Applied Computational Electromagnetics Society

Journal

June 2012 Vol. 27 No. 6

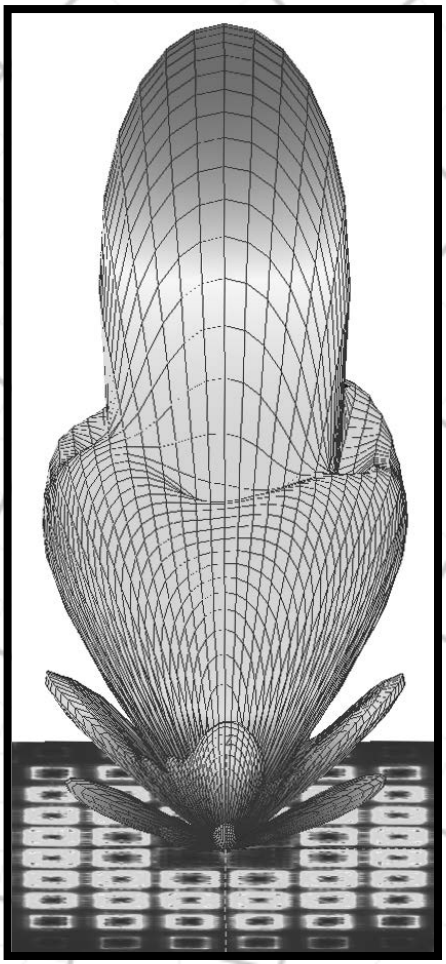

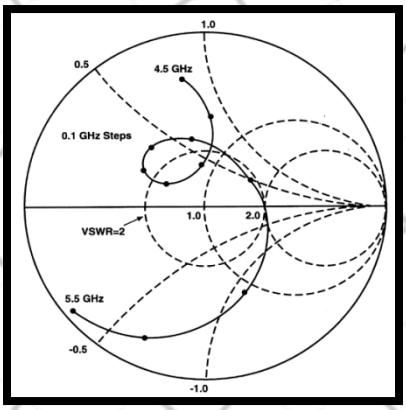

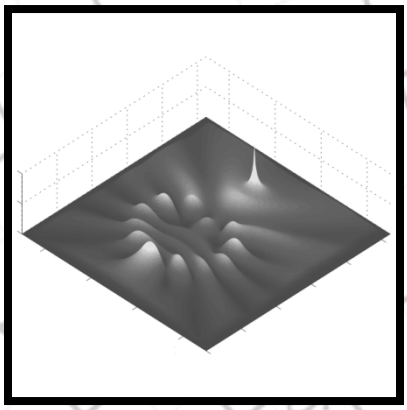

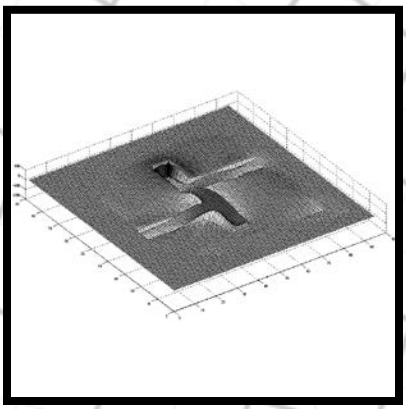

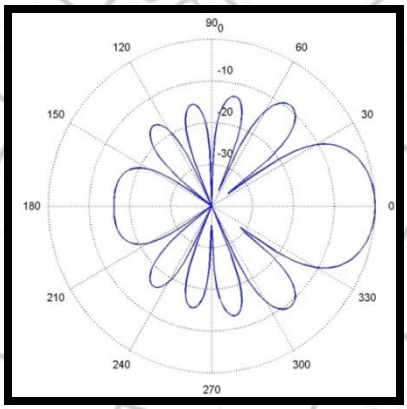

ISSN 1054-4887

GENERAL PURPOSE AND SCOPE: The Applied Computational Electromagnetics Society ***(ACES)*** Journal hereinafter known as the ***ACES Journal*** is devoted to the exchange of information in computational electromagnetics, to the advancement of the state-of-the art, and the promotion of related technical activities. The primary objective of the information exchange is to inform the scientific community on the developments of new computational electromagnetics tools and their use in electrical engineering, physics, or related areas. The technical activities promoted by this publication include code validation, performance analysis, and input/output standardization; code or technique optimization and error minimization; innovations in solution technique or in data input/output; identification of new applications for electromagnetics modeling codes and techniques; integration of computational electromagnetics techniques with new computer architectures; and correlation of computational parameters with physical mechanisms.

SUBMISSIONS: The ***ACES Journal*** welcomes original, previously unpublished papers, relating to applied computational electromagnetics. Typical papers will represent the computational electromagnetics aspects of research in electrical engineering, physics, or related disciplines. However, papers which represent research in applied computational electromagnetics itself are equally acceptable.

Manuscripts are to be submitted through the upload system of ***ACES*** web site http://aces.ee.olemiss.edu See "Information for Authors" on inside of back cover and at ***ACES*** web site. For additional information contact the Editor-in-Chief:

Dr. Atef Elsherbeni
Department of Electrical Engineering
The University of Mississippi
University, MS 386377 USA
Phone: 662-915-5382
Email: atef@olemiss.edu

SUBSCRIPTIONS: All members of the Applied Computational Electromagnetics Society are entitled to access and download the ***ACES Journal*** any published journal article available at http://aces.ee.olemiss.edu. Printed issues of the ***ACES Journal*** are delivered to institutional members. Each author of published papers receives a printed issue of the ***ACES Journal*** in which the paper is published.

Back issues, when available, are $50 each. Subscription to ***ACES*** is through the web site. Orders for back issues of the ***ACES Journal*** and change of address requests should be sent directly to ***ACES*** office at:

Department of Electrical Engineering
The University of Mississippi
University, MS 386377 USA
Phone: 662-915-7231
Email: aglisson@olemiss.edu

Allow four weeks advance notice for change of address. Claims for missing issues will not be honored because of insufficient notice, or address change, or loss in the mail unless the ***ACES*** office is notified within 60 days for USA and Canadian subscribers, or 90 days for subscribers in other countries, from the last day of the month of publication. For information regarding reprints of individual papers or other materials, see "Information for Authors".

LIABILITY. Neither ***ACES***, nor the ***ACES Journal*** editors, are responsible for any consequence of misinformation or claims, express or implied, in any published material in an ***ACES Journal*** issue. This also applies to advertising, for which only camera-ready copies are accepted. Authors are responsible for information contained in their papers. If any material submitted for publication includes material which has already been published elsewhere, it is the author's responsibility to obtain written permission to reproduce such material.

APPLIED COMPUTATIONAL ELECTROMAGNETICS SOCIETY JOURNAL

June 2012
Vol. 27 No. 6
ISSN 1054-4887

The ACES Journal is abstracted in INSPEC, in Engineering Index, DTIC, Science Citation Index Expanded, the Research Alert, and to Current Contents/Engineering, Computing & Technology.

The illustrations on the front cover have been obtained from the research groups at the Department of Electrical Engineering, The University of Mississippi.

JUNE 2012 REVIEWERS

Ahmed Abdelrahman
Guido Ala
Marco Arjona
Mohamed Bakr
Sami Barmada
Deb Chatterjee
Nihad Dib
Khaled ElMahgoub
Mario Fernandez
Christophe Fumeaux
Mohammed Hadi
Hai Jiang
Baek Jung
Yasushi Kanai
Shisong Li
Giampiero Lovat
Ricardo Matias
Manoj Meshram
Niladri Sarkar
Harvey Schuman
Yang Shao
Arda Ulku
Hui Wang
Theodoros Zygiridis

THE APPLIED COMPUTATIONAL ELECTROMAGNETICS SOCIETY

JOURNAL

Vol. 27 No. 6 June 2012

TABLE OF CONTENTS

"Dual-Band Loop-Loaded Printed Dipole Antenna with a Wideband Microstrip Balun Structure"
M. H. B. Ucar, A. Sondas, and Y. E. Erdemli……..…….458

"An Efficient Meshless Approach to Multi-scale Modeling in the Time-domain"
Y. Yu, F. Jolani, and Z. Chen…….…..…....…….466

"Efficient Marching-on-in-Degree Solver of Time Domain Integral Equation with Adaptive Cross Approximation Algorithm-Singular Value Decomposition"
H. H. Zhang, Q. Q. Wang, Y. F. Shi, and R. S. Chen.....475

"Optimization of Reception Antenna Composed with Unbalanced Fed Inverted L Element for Digital Terrestrial Television"
D. Yagyu and M. Taguchi……..……...483

"A Hybrid Finite Element-Boundary Integral-Characteristic Basis Function Method for Scattering by Multiple 3-D Cavities"
Z. Cui and Y. Han……..……....……..491

"Investigation of Frequency Effects on the Performance of Single-Sided Linear Induction Motor"
A. Shiri and A. Shoulaie……...……..497

"Simulation and Analysis of HEMP Coupling Effect on a Wire Inside an Apertured Cylindrical Shielding Cavity"
S. T. Song, H. Jiang, Y. L. Huang……505

"Planar Circular Monopole Antenna with Perforated Dielectric Resonator for Notched Ultra-Wide Band Applications"
S. H. Zainud-Deen, A. Shaker, and K. R. Mahmoud.....516

"Reducing the Numerical Calculation in the Wave Iterative Method by Image Processing Techniques"
H. Hrizi and N. Sboui……..…….524

"Characterization of Packet-Level Measurements for Vehicular Wireless Networks"
Y. Wang, X. Xing, and Y. Zhang……...…….532

Dual-Band Loop-Loaded Printed Dipole Antenna with a Wideband Microstrip Balun Structure

Mustafa H. B. Ucar, Adnan Sondas, and Yunus E. Erdemli

Electronics & Computer Education Department
Kocaeli University, Umuttepe Campus, 41380 Kocaeli, Turkey
mhbucar@kocaeli.edu.tr, asondas@kocaeli.edu.tr, yunusee@koceli.edu.tr

Abstract ─ A novel loop-loaded printed dipole (LLPD) with a wideband balun structure is presented for aiming a dual-band antenna operation at 3.0/5.5 GHz bands. The proposed balun structure alone demonstrates VSWR<1.5 performance over a 3:1 bandwidth. As the loop elements placed on the antenna aperture provides dual-band operation with at least 15% impedance bandwidths, the wideband balun/feed allows for matched and balanced excitation for the dipole over the bands of interest. An equivalent circuit modeling of the LLPD antenna is presented along with the corresponding simulations and measurements.

Index Terms ─ Balun/feed, dual-band operation, equivalent circuit model, loop elements, printed dipole.

I. INTRODUCTION

Compact multi-function antennas play a major role in today's communication systems where size, weight, power consumption and cost are the key issues in designing integrated transceiver circuitry. In this context, printed antennas were previously considered to achieve multi-band or wideband applications [1−16]. Printed dipole elements, in particular, are preferred in such applications due to their low-profile and easy fabrication. The dipoles, however, cannot perform in the way as predicted when they are excited directly by a coaxial feed. This is due to inherit unbalanced current excitation by the coax. To overcome this undesired phenomenon, a balun (balanced-to-unbalanced) structure is required in the coax-fed dipole applications in order to match the unbalanced coaxial transmission line to the balanced two-wire line, i.e. the dipole in this case.

In this study, a novel loop-loaded printed dipole (LLPD) with a wideband balun structure is introduced for a dual-band antenna operation at 3.0/5.5 GHz bands, which are designated for a specific radar application. Recently, parasitic or loading elements have been considered to obtain dual-band dipole operation [9, 10]. A dual-band printed dipole antenna with a multi-arm parasitic element is introduced in [9] for WiMAX applications covering the bands 2.5–3.8 GHz and 5.15–5.85 GHz. In [10], an antipodal printed dipole loaded with circular split-ring resonator (SRR) elements has been introduced for a dual-frequency operation. In that study, eight SRR elements consisting of two concentric split-rings each are placed along the length of the dipole to achieve a dual-band operation at 1.2 GHz and 2 GHz bands. Also in [11], the authors have recently introduced a twisted dipole antenna with switchable loadings to achieve tunable antenna operation for 3.0 GHz and 5.5 GHz bands.

In this research, we propose a novel printed dipole antenna loaded with two rectangular loop elements (without splits) asymmetrically placed along the dipole length to achieve the dual-band operation around the center frequencies of 3 GHz and 5.5 GHz. As compared to its counterparts [9, 10], the proposed LLPD configuration is rather simple in structure, thus offers more flexibility in designing for different operational frequencies while maintaining the desired antenna performance.

It is worth mentioning that the proposed antenna is low-cost, low-loss, low-profile, and is also arrayable [17]. We note that the full-wave

Submitted On: Jan. 26, 2012
Accepted On: April 25, 2012

analysis of the antenna design has been carried out using CST Microwave Studio, which utilizes the time-domain finite-integration method. In this article, we present the corresponding simulation and measurement results to demonstrate the performance of the proposed LLPD design. In addition, several parametric studies are presented to show the design flexibility of the proposed configuration. A simplistic equivalent circuit modeling of the LLPD is also presented.

II. ANTENNA AND BALUN/FEED DESIGN

The proposed LLPD/balun configuration is depicted in Fig. 1 along with the corresponding physical parameters. As shown, the antenna aperture consists of a printed dipole and a doublet of concentric loop elements asymmetrically located (at a distance of 0.3 mm) on each side of the dipole feed-gap, which is 0.89 mm. All these elements are supported by a thin substrate with t=0.79 mm and ε_r=2.2 (Arlon DiClad 880). While the dipole by itself resonates around 3 GHz, the inclusion of the loop elements allows for an additional operational frequency band around 5.5 GHz. The loop elements provide not only inherent inductive loading, but also capacitive loading to the dipole, thus achieving 50Ω matched dual-band operation. In particular, the capacitive effect occurs due to proximity of the loop elements to the dipole as well as interaction between the concentric loop elements. We remark that the critical parameters to achieve the desired dual-band performance are the loop dimensions, the effects of which on the antenna operation will be discussed in Section III.

When the dipole was excited directly by a coax-feed, the realized antenna could not perform in the way the simulations predicted [18]. This "expected" phenomenon is mainly due to the unbalanced behavior of the coax. Hence, a new balun structure having compatible conjunction with the dipole has been designed. As shown in Fig. 1, the LLPD is excited by a balun-feed structure placed vertically between the aperture and the ground plane (GP) where the aperture-GP distance is set to h=17 mm. This novel balun structure has a tapered microstripline with metallic extensions, and is supported by a similar substrate (t=0.79 mm, ε_r=2.2) placed on a triangular-shaped GP as depicted in detail in Fig. 2. The triangular shape [19] is chosen to accommodate the balun structure underneath the dipole gap appropriately. More importantly, the shape, position, and size of those extensions placed along the microstripline are determined to be the critical parameters of the balun design to achieve wideband VSWR performance. We note that for optimum performance the design parameters of the LLPD were re-optimized in integration with the balun-feed.

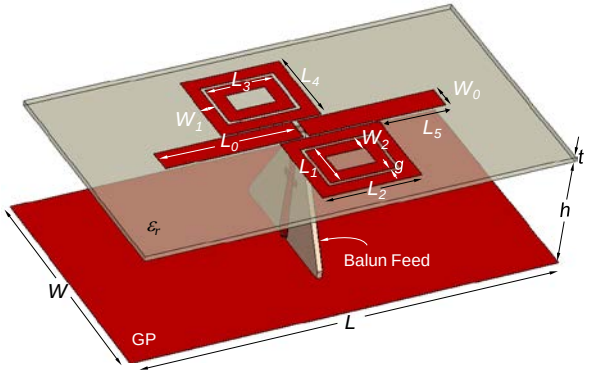

Fig. 1. The proposed LLPD/balun configuration: W=36, L=66, W_0=3.5, L_0=21.2, L_1=7.4, L_2=15.7, L_3=10.5, L_4=12.4, L_5=10.3, W_1=2.1, W_2=2, g= 0.5, t= 0.79, h= 17 (all in mm), ε_r=2.2.

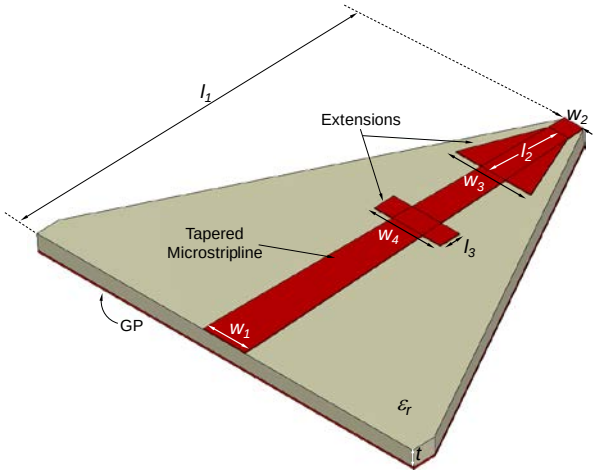

Fig. 2. The proposed balun configuration: l_1=18.275, l_2=3.4, l_3=1, w_1=2.2, w_2=1, w_3=4, w_4=3.5, t=0.79 (all in mm), ε_r=2.2.

III. RESULTS AND DISCUSSIONS

The simulated and measured VSWR characteristics of the back-to-back balun structure are displayed in Fig. 3. As shown, the realized

balun design with the extensions provides VSWR<1.5 over 2–6 GHz band, i.e. a 3:1 bandwidth. Also displayed in Fig. 3 are the results for the balun design without extensions, yielding relatively worse VSWR levels (around 1.5–2) for frequencies below 4.5 GHz. That is, the metallic extensions placed along the microstripline play a key role for better matching in lower frequencies. Also note that the measured data show ripple characteristics tracking the rather smooth simulated profile, mainly due to the standing-wave phenomenon observed in the measurements.

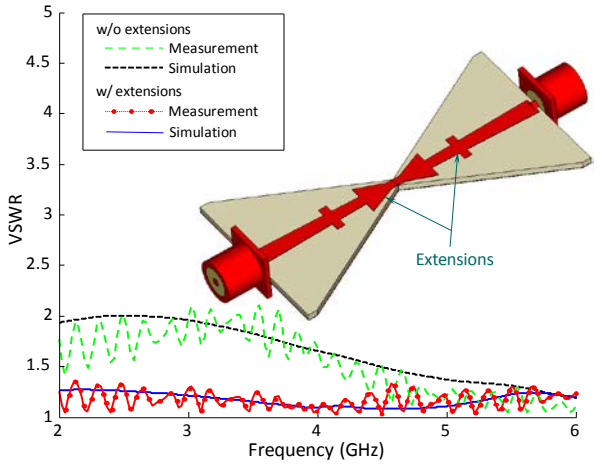

Fig. 3. The simulated and measured VSWR results for the balun designs.

Having discussed the balun design by itself, we now consider the performance of the LLPD antenna integrated with the balun-feed structure. The photograph of the fabricated LLPD/balun antenna is depicted in Fig. 4. In Fig. 5, we display the simulated and measured input reflection coefficient (S_{11}) characteristics of the LLPD design along with the corresponding bandwidth performances listed in Table 1. As seen, the agreement between the results is quite good except that a little amount of bandwidth reduction (~1.5%) is observed for the fabricated antenna. The discrepancies are probably due to material and fabrication tolerances. Of importance is that the realized antenna offers a dual-band operation with at least 15% S_{11} bandwidth at each band of interest, i.e. 3 GHz and 5.5 GHz where $|S_{11}|<-10$ dB criterion along with 50Ω system is considered. We note that the VSWR and return loss measurements were carried out using Rohde & Schwarz ZVB8 Vector Network Analyzer.

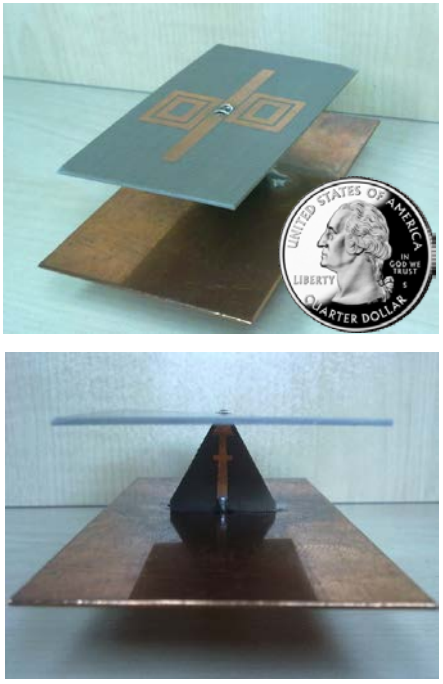

Fig. 4. The perspective views of the fabricated LLPD antenna.

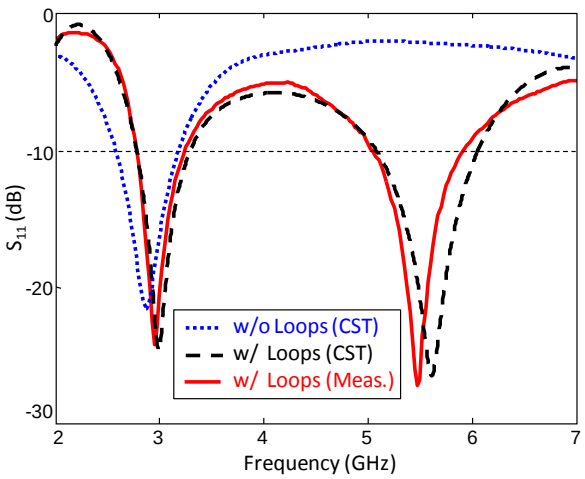

Fig. 5. The input reflection coefficient characteristics of the LLPD/balun design: the CST simulations for the cases with and without loop elements, and the measured results for the fabricated antenna with the loops are shown.

Also in Fig. 5, the simulated S_{11} performance of the dipole in absence of the loop elements is shown besides that of the LLPD design, where the loops play a key role in the occurrence of the upper frequency-band. In fact, the inclusion of the loops causes an additional resonance as well as an improvement in impedance matching in the upper

band as shown in Fig. 6, where the input impedance at the balun-coax end is displayed for the cases without and with the loops. As seen, for the former case, there are two resonances around 2.7 GHz and 4.8 GHz where the real part of impedance levels reaches 400 Ohms. On the other hand, for the latter case, an additional resonance occurs around 5.5 GHz, while the previous 4.8 GHz band shifts downwards to 4.2 GHz due to the loading effect of the loops. In addition, there is a slight upward shift observed in the lower band as can be seen from Figs. 5 and 6. More importantly, the impedances are dramatically reduced to 50 Ω levels owing to the inclusion of the loops, thus a desired matching is achieved around 5.5 GHz band.

Table 1: Bandwidth (BW) comparison of the simulated and fabricated antennas

Band	Simulation (CST)	Measurement
3.0 GHz	2.78–3.29 GHz BW~16.8%	2.78–3.24 GHz BW~15.3%
5.5 GHz	5.07–6.06 GHz BW~17.8%	5.03–5.92 GHz BW~16.3%

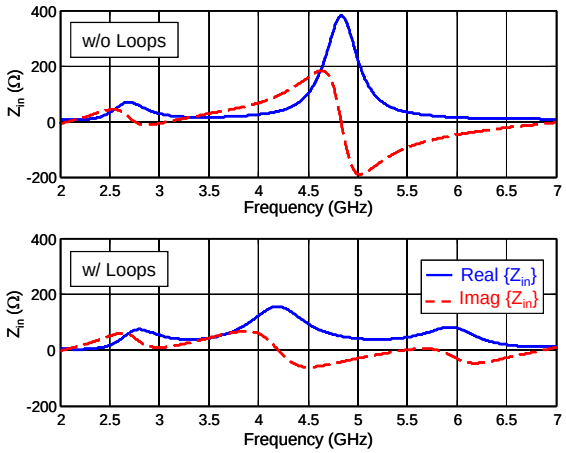

Fig. 6. The simulated input impedances (Z_{in}) for the cases without (top) and with (bottom) the loops.

In Fig. 7, we also display the computed surface current distributions over the antenna aperture for both frequency bands. As seen, the current distribution at 3 GHz is mainly concentrated along the dipole, while the distribution at 5.5 GHz is predominantly occurs around the loops as well as between the dipole and the loops. These results also confirm that the lower frequency band is mainly due to the dipole resonance, but the higher band occurs owing to presence of the loop elements.

In addition, we carried out radiation pattern measurements for the LLPD/balun configuration in an anechoic chamber using ETS-Lindgren 3117 DRG horn antenna (1–18 GHz). The computed and measured radiation patterns at 3 GHz and 5.5 GHz are displayed in Fig. 8 where a reasonably well agreement is observed. As shown, the antenna offers a broadside radiation pattern with a directive gain of about 7.5 dBi at the respective frequencies, where the front-to-back ratios are predicted as being higher than 13 dB. In addition, the computed radiation efficiency of the LLPD antenna is better than 95% at the related frequencies.

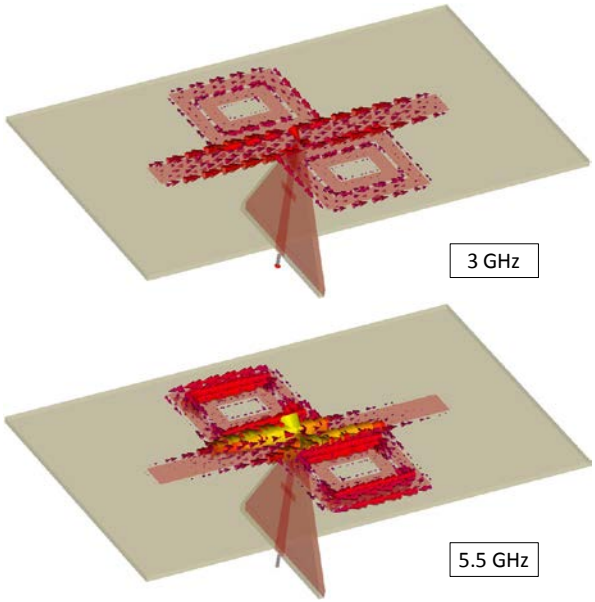

Fig. 7. The surface current distributions over the antenna aperture at 3 GHz (top) and 5.5 GHz (bottom).

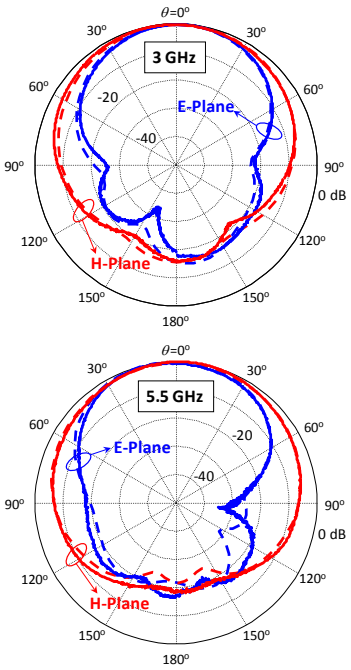

Fig. 8. The computed (dashed) and measured (solid) radiation patterns of the LLPD/balun design at 3 GHz (top) and 5.5 GHz (bottom).

Although the presented design is projected for a specific frequency operation, one can obtain a similar dual-band performance at different operational frequencies by varying some parameters of the antenna structure. In designing, we have carried out several parametric studies to achieve the optimum antenna performance. Here, we present those studies performed for the three critical design parameters, namely, the dipole length ($2L_0$) and the loop dimensions (L_2 and L_4). As can be seen from Fig. 9, the dipole length mainly determines the lower-band, while the loop dimensions play a major role in occurrence of the higher-band. Of importance is that when the dipole length is fixed, by varying the loop size one can shift the higher-band upwards or downwards with an insignificant effect on the lower-band (Fig. 9 (b) and (c)). Similarly, by varying the dipole length with the loop size fixed, one can shift the lower-band accordingly (Fig. 9 (a)). In brief, those studies demonstrate the flexibility of the proposed LLPD configuration; thus, provide some guidelines in designing for a different set of dual frequencies.

In addition, other loop parameters have also been examined during the design optimization process. The presence of inner loops is shown to have a critical effect on S_{11} levels, particularly in the upper band, while there is no significant effect observed when the gap between the outer and inner loops is varied in the range of 0.3–0.7 mm with noting that it is set to 0.5 mm in the final design.

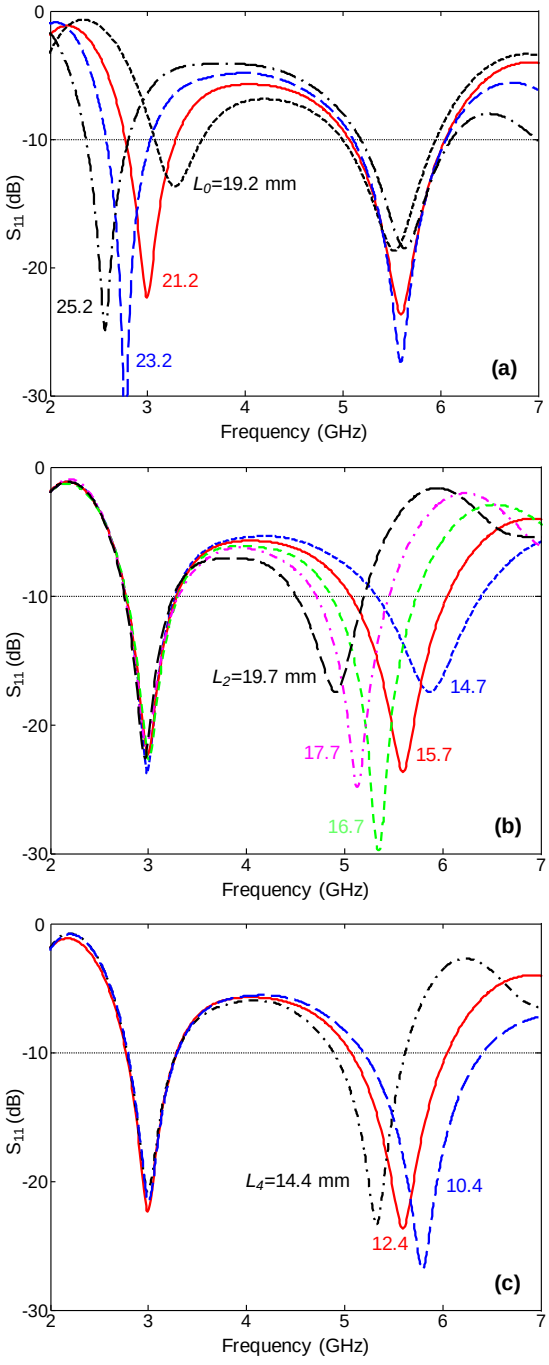

Fig. 9. The effects of (a) the dipole length ($2L_0$) and the loop dimensions (b) L_2 and (c) L_4 on the S_{11} performance.

When the dipole-loop gap is increased from the optimum value of 0.3 mm to 0.5 mm, there is a slight bandwidth reduction, and also about 0.2 GHz downward frequency shift observed. Moreover, the loop-widths have some slight effect on the performance. In particular, ±0.2 mm variation in the widths (W_1 & W_2) results in an upward or downward shift (at most 0.1 GHz) in the upper frequency-band. Similarly, the placement of the loops along the dipole-length (L_5) plays a role in fine-tuning of the upper center-frequency. Note that there has been no significant influence on the lower-band as the loop parameters are varied.

We also remark that there has been no degradation observed in the radiation properties of the antenna for the parametric studies considered. Furthermore, the proposed design tends to have a capability of broadband dipole performance (instead of dual-band). That is, with an appropriate parameter optimization, the gap between the lower and upper frequency bands may be closed, so the bands are joined together to provide a rather larger bandwidth performance. In Fig. 10, we display S_{11} characteristics of such a broadband design. As seen, this preliminary design offers 52.5% bandwidth (2.95–5.05 GHz) where $|S_{11}| < -6$ dB. We also note that the computed realized gain is 6–8 dB over the band of interest where radiation patterns are similar to those in Fig. 8.

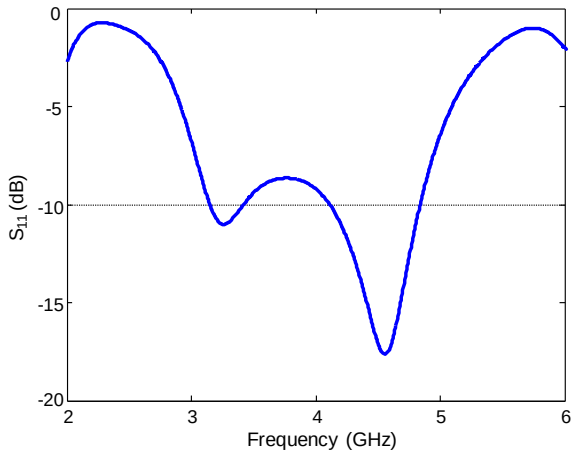

Fig. 10. The input reflection coefficient characteristics of the broadband LLPD/balun design where the parameters are same as those in Fig. 1 and Fig. 2 except W_0=2.9, L_0=19.1, L_2=18.75, L_3=13.55, L_5=7.3, l_3= 3 (all in mm).

Furthermore, an equivalent circuit modeling (ECM) for the LLPD design has been considered in this study. As seen in Fig. 11, the proposed simplistic model is based on the equivalent circuit models for the dipole antenna [20] and the loop elements [21]. By integrating those two models and including an additional capacitor (C_3) representing the coupling between the dipole and the loops, we obtained the ECM for the LLPD antenna. The corresponding capacitance, inductance, and resistance values (C_0=3.15 nF, L_0=0.2 nH, R_1=80 Ω, C_1=3 pF, L_1=0.7nH, R_2=2 Ω, C_2=1.4 pF, L_2=0.4 nH, R_3=11 Ω, C_3=0.9 pF) in the model were acquired by means of a curve-fitting algorithm considering only the related S_{11} magnitude for the design parameters given in Fig. 1. As shown in Fig. 12, the proposed ECM predicts the operational bands reasonably well with some differences in the out-of-bands. We note that in the ECM, R_1 mainly represents the radiation resistance of the dipole antenna, whereas the resistive elements R_2 and R_3 stand for possible physical losses. We note that those circuit element values will change if any dimension in the structure is altered. One can also develop empirical formulae relating the ECM values with the corresponding physical design parameters [1].

IV. CONCLUSION

In this paper, we have introduced a novel loop-loaded printed dipole antenna for a dual-band application operating at 3 GHz and 5.5 GHz bands. The proposed design has two new features: While the loop elements placed on the antenna aperture provides dual-band operation at the designated frequencies, the wideband balun/feed allows for matched and balanced excitation for the dipole. The practical realization of the proposed LLPD/balun design was carried out, resulting in reasonably good performance in accordance with the simulations. In particular, the design offers 15% impedance bandwidths at the corresponding bands with a fairly well radiation performance. We remark that the proposed low-profile antenna is simple in structure and can easily be adapted for different operational frequencies to be employed in various communications applications. Also, the proposed design can readily be extended to an array configuration. Finally, a simplistic equivalent circuit model for the LLPD antenna has

been proposed, predicting the antenna performance quite well.

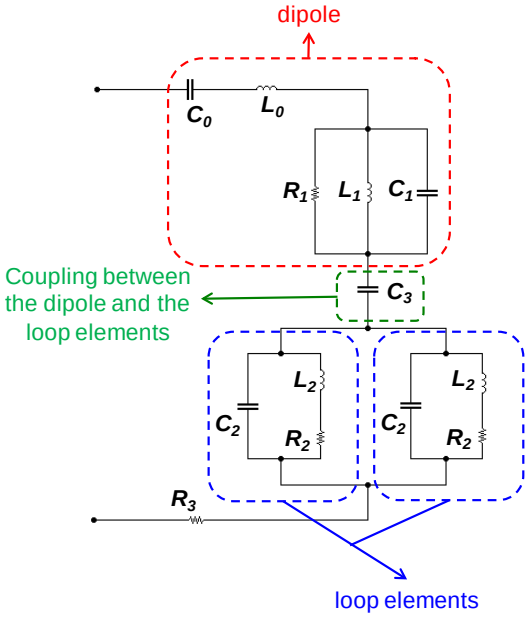

Fig. 11. The proposed equivalent circuit model for the LLPD antenna.

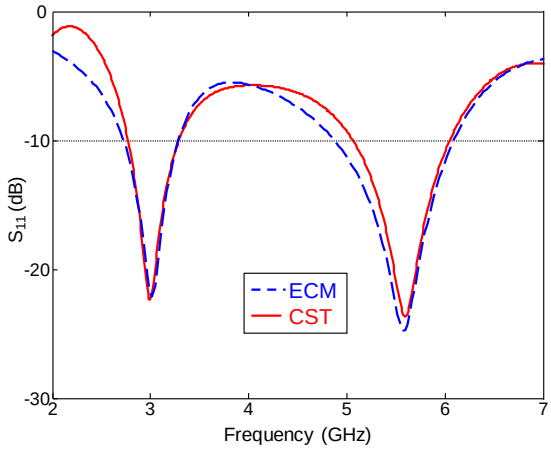

Fig. 12. The comparison of S_{11} characteristics for the simulated (CST) and the equivalent circuit model (ECM) of the LLPD antenna.

ACKNOWLEDGMENT

This work was supported by the Scientific & Technological Research Council of Turkey (TÜBİTAK–107E198) and partly funded by the Scientific Research Projects Unit of Kocaeli University (KOU–2010/35). We would like to thank all the reviewers for their invaluable comments.

REFERENCES

[1] Y. E. Erdemli, K. Sertel, R. A. Gilbert, D. E. Wright, and J. L. Volakis, "Frequency Selective Surfaces to Enhance Performance of Broadband Reconfigurable Arrays," *IEEE Trans. Antennas Propag.*, vol. 50, no. 12, pp. 1716-1724, 2002.

[2] A. Sondas, M. H. B. Ucar, and Y. E. Erdemli, "Tunable SRR-Based Substrate for a Microstrip Patch Antenna," *Turkish J. Elec. Eng. & Comp. Sci.*, vol. 20, no. 1, pp. 159-168, 2012.

[3] F. J. Herraiz-Martinez, L. E. Garcia-Munozle, D. Segovia-Vargas, D. Gonzalez-Overjero, and C. Craeye, "Arrays of Dual-Band Printed Dipoles Loaded with Metamaterial Particles," *3rd European Conf. Antennas and Propag. (EuCAP)*, pp. 3818-3822, Mar. 2009.

[4] J. -M. Floc'h and H. Rmili, "Design of Multiband Printed Dipole Antennas using Parasitic Elements," *Microwave Opt. Technol. Lett.*, vol. 48, no. 8, pp. 1639-1645, Aug. 2006.

[5] W. X. An, K. L. Lau, S. F. Li, and Q. Xue, "Wideband E-Shaped Dipole Antenna with Staircase-Shaped Feeding Strip," *Electronics Letters*, vol. 46, no. 24, pp. 1583-1584, 2010.

[6] H. Wong, K.-M. Mak, K.-M. Luk, "Wideband Shorted Bowtie Patch Antenna with Electric Dipole," *IEEE Trans. Antennas Propag.*, vol. 56, no. 7, pp. 2098-2101, 2008.

[7] Q. Wu, R. Jin, J. Geng, D. Su, "On the Performance of Printed Dipole Antenna with Novel Composite Corrugated-Reflectors for Low-Profile Ultrawideband Applications," *IEEE Trans. Antennas Propag.*, vol. 58, no. 12, pp. 3839-3846, 2010.

[8] X. N. Low, Z. N. Chen, W. K. Toh, "Ultrawideband Suspended Plate Antenna with Enhanced Impedance and Radiation Performance," *IEEE Trans. Antennas Propag.*, vol. 56, no. 8, pp. 2490-2495, 2008.

[9] W.-S. Chen and Y.-H. Yu, "Dual-Band Printed Dipole Antenna with Parasitic Element for WiMAX Applications," *Electronics Letters*, vol. 44, no. 23, pp. 1338-1339, 2008.

[10] V. Gonzalez-Posadas, J. L. Jimenez-Martin, F. J. Herraiz-Martinez, L. E. Garcia-Munoz, and D. Segovia-Vargas, "Design of Dual-Frequency SRR-Loaded Dipole with Equivalent Circuit Approach," *Electronics Letters*, vol. 45, no. 19, pp. 964-966, 2009.

[11] A. Sondas, M. H. B. Ucar, and Y. E. Erdemli, "Switchable Loop-Loaded Printed Dipole Antenna with a Balun/Feed Structure," *Microwave Optical Tech. Letts.*, vol. 54, no. 1, pp. 76-79, Jan. 2012.

[12] M. Naghshvarian-Jahromi and N. Komjani-Barchloui, "Analysis of the Behavior of Sierpinski Carpet Monopole Antenna," *Applied*

Computational Electromagnetics Society (*ACES*) *Journal*, vol. 24, no. 1, pp. 32-36, February 2009.

[13] J. C. Liu, W. Shao, and B. Z. Wang, "A Dual-Band Metamaterial Design using Double SRR Structures," *Applied Computational Electromagnetic Society (ACES) Journal*, vol. 26, no. 6, pp. 459-463, June 2011.

[14] R. Bakshi and S. K. Sharma, "A Wideband U-Slot Loaded Modified E-Shape Microstrip Patch Antenna and Frequency Agile Behavior by Employing Different Height Ground Plane and Ribbon Type Switches," *Applied Computational Electromagnetic Society (ACES) Journal*, vol. 26, no. 7, pp. 539-550, July 2011.

[15] Y. Zhao, L. Zhong, J. S. Hong, and G. M. Zhang, "A Monopole Antenna with SIR Ground for Harmonic Suppression and Bandwidth Enhancement," *Applied Computational Electromagnetic Society (ACES) Journal*, vol. 26, no. 8, pp. 705-708, August 2011.

[16] I. I. Papadopoulos-Kelidis, A. X. Lalas, N. V. Kantartzis, and T. D. Tsiboukis, "Combined Bowtie Peano Antennas for Wideband Performance," *Applied Computational Electromagnetic Society (ACES) Journal*, vol. 26, no. 9, pp. 760-767, Sep. 2011.

[17] A. Sondas, M. H. B. Ucar, and Y. E. Erdemli, "Dual-Band Loop-Loaded Printed Dipole Array," *Mediterranean Microwave Symposium (MMS)*, pp. 62-64, Guzelyurt, 25-27 Aug. 2010.

[18] A. Sondas, M. H. B. Ucar, and Y. E. Erdemli, "Tunable Loop-Loaded Printed Dipole Antenna Design," *IEEE Int. Symp. Antennas Propagat.*, Toronto, Canada, pp. 1-4, 11-17 July 2010.

[19] T. Xia, S. Yang, and Z. Nie, "Design of a Tapered Balun for Broadband Arrays with Closely Spaced Elements," *IEEE Antennas and Wireless Propagation Letters*, vol. 8, pp. 1291-1294, 2009.

[20] M. Hamid and R. Hamid, "Equivalent Circuit of Dipole Antenna of Arbitrary Length," *IEEE Trans. Antennas Propagat.*, vol. 45, no. 11, pp. 1695-1696, 1997.

[21] L. -H. Hsieh and K. Chang, "Equivalent Lumped Elements G, L, C, and Unloaded Q's of Closed- and Open-Loop Ring Resonators," *IEEE Trans. Microwave Theory Techniques*, vol. 50, no. 2, pp. 453-460, 2002.

Mustafa H. B. Ucar was born in Istanbul, Turkey, in 1982. He received the B.S. and M.S. degrees from the Kocaeli University, Kocaeli, Turkey both in Electronics & Computer Education Department in 2004 and 2007, respectively. He is currently a Ph.D. candidate and a research assistant in the same institution. His research interests include numerical analysis and design of reconfigurable antennas/arrays/EM filters and frequency selective surfaces.

Adnan Sondas was born in Tokat, Turkey, in 1978. He received the B.S. degree from the Sakarya University, Sakarya, in Electronics & Computer Education Department in 2001 and the M.S. and Ph.D. degrees from the Kocaeli University, Kocaeli, both in Electronics & Computer Education Department, in 2005 and 2011, respectively. He is currently a research assistant in Electronics and Computer Education at Kocaeli University. His research interests include numerical analysis and design of metamaterials, reconfigurable antennas/arrays/EM filters.

Yunus E. Erdemli was born in Tatvan, Turkey, in 1970. He received the B.S. degree in electrical engineering from Middle East Technical University, Ankara, Turkey, in 1992 and the M.S. and Ph.D. degrees from the University of Michigan, Ann Arbor, both in electrical engineering, in 1996 and 2002, respectively. During 1994–2002, he was a graduate Research Assistant at the University of Michigan Radiation Laboratory, Ann Arbor, where he also served as a Postdoctoral Research Associate. He has been a Professor in the Department of Electronics and Computer Education, Kocaeli University, Kocaeli, Turkey since 2002. His research interests include numerical analysis and design of conformal and reconfigurable arrays, frequency selective surfaces/volumes, and metamaterials for various communication applications.

An Efficient Meshless Approach to Multi-scale Modeling in the Time-domain

Yiqiang Yu[1,2], Farid Jolani[2], and Zhizhang (David) Chen[2]

[1] School of Information Engineering
East China Jiaotong University, Nanchang, China
yiqiang.yu@dal.ca

[2] Department of Electrical and Computer Engineering
Dalhousie University, Halifax, Canada
farid.jolani@dal.ca; z.chen@dal.ca

Abstract ─ An efficient multi-scale approach to meshless modeling of three-dimensional guided wave problems is realized by hybridization of the radial point interpolation method (RPIM) and the unconditionally stable leapfrog alternating-direction implicit (ADI-) RPIM scheme. In it, the solution domain is regionalized; the leapfrog ADI-RPIM is applied to regions with coarse nodal distributions while the original RPIM is applied to the rest of the dense nodal solution domain. With application of the leapfrog ADI scheme, a uniform time-step can now be applied to the entire solution domain without temporal and spatial interpolation between different computational regions. Furthermore, in the proposed scheme, implicit updating of field variables is confined only within the regions of densely-distributed nodes, yielding a significant saving in memory overhead and a further reduction in CPU time in comparison with leapfrog ADI-RPIM and original RPIM, respectively.

Index Terms ─ Alternating-direction implicit scheme, finite-difference time-domain, hybrid methods, meshless methods, radial point interpolation method.

I. INTRODUCTION

With recent advances in modern electronic and electrical technologies, electromagnetic problems are becoming exceedingly complex; as a result, modern computer-aided tools based on conventional computational electromagnetic methods often experience difficulties in providing accurate modeling solutions within a reasonable time. To tackle the problem, higher-order basis functions along with mesh reduction techniques have been applied to the conventional methods to reduce memory and time consumption while maintaining the same level of modeling accuracy [1, 2]; or alternatively, novel numerical methods have been sought that can free constraints on numerical accuracy from the connectivity laws of grid nodes and shape and dimension of elementary cells that long exist in the conventional methods. One of the promising new numerical techniques is the meshless method. It utilizes a set of scattered nodes to represent a problem domain and associated boundaries, rather than a predefined mesh/grid as used in the conventional numerical methods.

Among the meshless techniques that have been adapted for use in computational electromagnetics, the radial point interpolation method (RPIM) [3] gains significant attention due to its simplicity, accuracy, and consistency. Its applications have been seen in one dimensional wave propagation problems [4], two-dimensional H-plane bent waveguides [5, 6], and three-dimensional cavity problems [7]. Recently, the method has been extended to electromagnetic radiation and scattering problems in open-region [8] and with material interfaces [9]. Although the method has been repeatedly reported to be much more robust than the conventional finite-difference

Submitted On: Jan. 3, 2012
Accepted On: April 22, 2012

time-domain (FDTD) method, computational performance of the method is somehow limited by its stability constraint on time step; this is a drawback from the employment of explicit finite-difference scheme to approximate the time derivatives in Maxwell's equations. Efforts were thus made in our previous work [10, 11] to further improve the computational efficiency of the method, with the implementation of leapfrog alternating-direction-implicit (ADI) scheme [12-15] to remove the stability constraint; it leads to an unconditionally stable meshless ADI-RPIM method.

Computational efficiency of the unconditionally stable meshless ADI-RPIM method has then been assessed with a large number of numerical experiments. It is observed that the used implicit meshless scheme is very attractive for the problems where nodes are highly irregularly distributed over an entire solution domain.

However, when irregular nodal distributions are applied only in a small portion of the problem domain, the method appears to be less efficient. Further analysis of the computational expenditures leads to the explanation: since the method is based on the implicit updates of field variables, extra computational cost is required for matrix assembly of extra off-diagonal terms in coefficient matrix and the associated matrix computation during the time-marching; depending on the average number of nodes that are enclosed in the support domain for interpolation, this process can sometimes become time-consuming and compromise the overall computational efficiency of the unconditional meshless scheme.

Therefore, it is desirable to develop a smart hybrid approach that applies the unconditionally stable meshless method intelligently. To this end, in this paper, we propose the approach that applies the efficient leapfrog ADI-RPIM only to computational sub-regions with dense nodal distributions and the original RPIM to the rest of the problem domain. In such a way, the extra memory required to store the off-diagonal terms of the matrix equations and the additional CPU time for matrix computations can be minimized. Thanks to the multi-scale modeling capability of the meshless RPIM, such a hybridization can be realized easily without need of sub-gridding and additional spatial interpolation. Moreover, due to the alternating nature of the field variables in leapfrog ADI-RPIM, temporal interpolation is not needed either.

In the next section, we will first briefly describe the RPIM method in three dimensions and then present a set of RPIM equations with the convolutional perfectly matched layer (CPML) absorbing boundary conditions. In Section 3, we will present the unconditional stable RPIM method with the corresponding leap-frog ADI-RPIM equations and then combine it with the original explicit RPIM to formulate the hybrid approach; In Section 4, we will numerically validate the effectiveness of the proposed approach; the comparison between the proposed hybrid approach, the original RPIM method, the leapfrog ADI-RPIM, and the conventional FDTD in terms of computational cost is shown.

II. THE MESHLESS RPIM METHOD

The formulation of the meshless RPIM in computing electromagnetic fields comprises three key steps: representation of field variables with the point interpolation scheme, construction of shape functions, and discretization of Maxwell's time-dependent equations.

A. The Local Point Interpolation Scheme and Shape Function

The node-based RPIM method discretizes a solution domain using a set of spatial nodes. As seen in Fig.1, an arbitrary solution domain is filled with scattered nodes; whereas, the boundary of the domain is precisely represented with lying-on nodes. The underlying point interpolation scheme interpolates the field variable u at point q locally with and only with its values at surrounding nodes. A support domain S is defined for each q to enclose N points that are used for interpolation. The values of parameter N in the range of 4-12 are used throughout this work. Mathematically, such interpolation can be expressed as:

$$u(X) = \sum_{n=1}^{N} r_n(X) a_n + \sum_{m=1}^{M} p_m(X) b_m , \qquad (1)$$

where $X=(x_q, y_q, z_q)$ is the coordinate of point q, $r_n(X)$ is the radial basis function, $p_m(X)$ is the monomial basis function, and a_n and b_m are the associated interpolation coefficients.

The radial basis function in a Gaussian form is deployed in our work to weight the contributions

from surrounding nodes when interpolating the field value at point *q*. It is expressed as.

$$r_n(X) = e^{-c(r/d_s)^2}, \quad (2)$$

where $r = \sqrt{(x_q - x_n)^2 + (y_q - y_n)^2 + (z_q - z_n)^2}$, (x_n, y_n, z_n) are the coordinates of the *n*th node surrounding the point of interest *q*, d_s is the radius that defines the area of the support domain *S*, and shape parameter *c* controls the decay rate of the function over the space. *AD* is the average nodal spacing between two nodes in the domain.

A linear combination of four (M =4) monomial basis functions in the form of $[1, x, y, z]$ is used to construct the polynomial in eqn. (1).

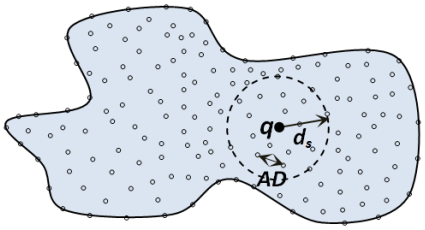

Fig. 1. Support domain of the point *q (dashed line)* and its surrounding nodes.

The interpolation coefficients a_n and b_m are solved locally with a matrix equation that relates true field values at nodes within the support domain at their relative spatial positions [3, 7]. Equation (1) can thus be rewritten as

$$u(X) = \left[\mathbf{R}^{\mathrm{T}}(\mathbf{X})\mathbf{S}_{\mathbf{a}} + \mathbf{P}^{\mathrm{T}}(\mathbf{X})\mathbf{S}_{\mathbf{b}}\right]\mathbf{U}_{\mathbf{s}} = \mathbf{\Phi}(\mathbf{X})\mathbf{U}_{\mathbf{s}}, \quad (3)$$

where $\mathbf{\Phi}(\mathbf{X}) = [\Phi_1(X), \Phi_2(X), \cdots, \Phi_N(X)]$ is a vector of shape functions associated with *N* nodes in the support domain of *q*. $\mathbf{U_s}$ is the vector holding the considered field component values at the *N* nodes, and the entries of constant matrices $\mathbf{S_a}$ and $\mathbf{S_b}$ can be found in [7].

B. RPIM Equations with CPML Absorbing Boundary Condition

By substituting the spatial derivatives of field variables in Maxwell's time-dependent equations with corresponding derivatives of (3) and applying the central difference scheme to approximate the time-derivatives, the leap-frog RPIM equations for time-marching of field variables can be formulated [7]. As this work addresses unbounded radiation and scattering problems, the CPML absorbing boundary conditions [16, 17] are deployed. Due to limited space, only the update equation for the *x*-directed electric field component and *z*-directed magnetic field component are presented below. The update equations for other field components can be produced by a cyclical exchange of *x*, *y*, and *z* indices. For detailed implementation of PML in meshless methods, please refer to [8, 11].

$$E_{x,i}^{n+\frac{1}{2}} = E_{x,i}^{n-\frac{1}{2}} + \frac{\Delta t}{\varepsilon}\left(\frac{1}{\kappa_{y,i}}\sum_j H_{z,j}^n \partial y \Phi_j - \frac{1}{\kappa_{z,i}}\sum_j H_{y,j}^n \partial z \Phi_j\right) + \frac{\Delta t}{\varepsilon}\left(\psi_{e_{xy,i}}^n - \psi_{e_{xz,i}}^n\right), \quad (4)$$

$$H_{z,i}^{n+1} = H_{z,i}^n + \frac{\Delta t}{\mu}\left(\frac{1}{\kappa_{y,i}}\sum_j E_{x,j}^{n+\frac{1}{2}} \partial y \Phi_j - \frac{1}{\kappa_{x,i}}\sum_j E_{y,j}^{n+\frac{1}{2}} \partial x \Phi_j\right) + \frac{\Delta t}{\mu}\left(\psi_{h_{zy,i}}^{n+\frac{1}{2}} - \psi_{h_{zx,i}}^{n+\frac{1}{2}}\right), \quad (5)$$

where $$\psi_{e_{xy,i}}^n = b_{y,i}\psi_{e_{xy,i}}^{n-1} + a_{y,i}\sum_j H_{z,j}^n \partial y \Phi_j, \quad (6)$$

$$\psi_{e_{xz,i}}^n = b_{z,i}\psi_{e_{xz,i}}^{n-1} + a_{z,i}\sum_j H_{y,j}^n \partial z \Phi_j, \quad (7)$$

$$\psi_{h_{zy,i}}^{n+\frac{1}{2}} = b_{y,i}\psi_{h_{zy,i}}^{n-\frac{1}{2}} + a_{y,i}\sum_j E_{x,j}^{n+\frac{1}{2}} \partial y \Phi_j, \quad (8)$$

$$\psi_{h_{zx,i}}^{n+\frac{1}{2}} = b_{x,i}\psi_{h_{zx,i}}^{n-\frac{1}{2}} + a_{x,i}\sum_j E_{y,j}^{n+\frac{1}{2}} \partial x \Phi_j, \quad (9)$$

and $$b_{\tau,i} = e^{-((\sigma_{\tau,i}/\kappa_{\tau,i})+\alpha_{\tau,i})(\Delta t/\varepsilon_o)}, \quad (10)$$

$$a_{\tau,i} = \frac{\sigma_{\tau,i}}{(\sigma_{\tau,i}\kappa_{\tau,i} + \kappa_{\tau,i}^2\sigma_{\tau,i})}(b_{\tau,i} - 1), \quad (11)$$

$$\sigma_{\tau,i} = \sigma_m^{\tau}\left(\frac{\rho_{\tau,i}}{\delta_\tau}\right)^n \quad (12), \quad \kappa_{\tau,i} = 1 + (\kappa_\tau^m - 1)\left(\frac{\rho_{\tau,i}}{\delta_\tau}\right)^n. \quad (12)$$

δ_τ and $\rho_{\tau,i}$ are the thickness of the PML and the depth of node *i* across the interior-PML interface along the *x*, *y* or *z* directions, respectively; power *n* is the order of scaling; $\kappa_{\tau,i}$ and $\sigma_{\tau,i}$ are the stretched coordinate metric and electric conductivities evaluated at each E-field node *i* in the CPML region; $\alpha_{\tau,i}$ is the shifting parameter, and κ_τ^m and σ_τ^m are the maximum values of $\kappa_{\tau,i}$ and $\sigma_{\tau,i}$.

III. THE UNCONDITIONALLY STABLE MESHLESS ADI-RPIM METHOD

In the original meshless RPIM method, there exists an upper limit for the time-step that can be applied to update field variables; when the time-step exceeds the limit, the time-marching scheme

will become unstable and give rise to divergent numerical results. The stability limit on the time-steps used in the original meshless RPIM method is extracted from [7] and listed here for completeness.

$$\Delta t \le \frac{2}{sqrt(\left|\lambda_{\max}(\mathbf{Q})\right|}, \tag{13}$$

where $\lambda_{\max}(\mathbf{Q})$ is the largest eigenvalue of matrix Q in terms of magnitude; and Q=CB+DA, where A, B, C, and D are the coefficient matrices associated with the right-hand-side of the meshless RPIM formulation.

The conditional stability expressed by (16) is due to employment of the explicit finite-difference approximation to the time derivatives in Maxwell's equations. In order to eliminate the stability constraint and consequently improve the computational efficiency with a larger step, a leapfrog version of the ADI scheme is incorporated into the RPIM method in [10], leading to an unconditionally stable *leapfrog* ADI-RPIM meshless method. The resultant scheme is implicit that requires solving a band matrix at each time iteration. The formulations for the implicit update of field components E_x and H_z are extracted from [10] and are listed below for simplicity and completeness.

$$E_{x,i}^{n+\frac{1}{2}} - \frac{\Delta t^2}{4\mu\varepsilon}\sum_j\sum_k E_{x,k}^{n+\frac{1}{2}}\partial y\Phi_k\partial y\Phi_j = E_{x,i}^{n-\frac{1}{2}} - \frac{\Delta t^2}{4\mu\varepsilon}\sum_j$$

$$\sum_k E_{x,k}^{n-\frac{1}{2}}\partial y\Phi_k\partial y\Phi_j + \frac{\Delta t}{\varepsilon}(\sum_j H_{z,j}^n\partial y\Phi_j - \sum_j H_{y,j}^n\partial z\Phi_j). \tag{14}$$

$$H_{z,i}^{n+1} - \frac{\Delta t^2}{4\mu\varepsilon}\sum_j\sum_k H_{z,k}^{n+1}\partial x\Phi_k\partial x\Phi_j = H_{z,i}^n - \frac{\Delta t^2}{4\mu\varepsilon}\sum_j$$

$$\sum_k H_{z,k}^n\partial x\Phi_k\partial x\Phi_j + \frac{\Delta t}{\mu}(\sum_j E_{x,j}^{n+\frac{1}{2}}\partial y\Phi_j - \sum_j E_{y,j}^{n+\frac{1}{2}}\partial x\Phi_j). \tag{15}$$

Here the range of values that correspond to indices *k* and *j* depends on the number of neighboring nodes enclosed in the local support domain of the node *i*. For instance, when *N*=4, the values of *k* and *j* are in the range of 1- 4, and the *i*th row of resultant band coefficient matrix will have 9 nonzero elements.

IV. THE PROPOSED HYBRID MESHLESS ADI-RPIM SCHEME

In the proposed hybrid scheme, a solution domain is divided into a number of sub-domains that are categorized into dense node regions and coarse node regions. A node *i* is considered to be in a dense node region when ratio of the average nodal spacing '*AD*' in the local support domain of node *i* to the average distance between two adjacent nodes over the entire solution domain falls below a pre-determined threshold; an optimized search routine is developed and applied to decide appropriate boundaries of those sub-regions.

The leapfrog ADI-RPIM is then applied to the dense node sub-regions; whereas, the original RPIM is applied to the remaining coarse node regions. For nodes lying at a region interface, field values are computed with the ADI-RPIM scheme. As can been seen from (15)-(16), E-field, and H-field in the leapfrog ADI-RPIM are staggered in time in the same manner as RPIM; synchronization of the time steps of dense regions and outer coarse regions can thus be realized without temporal interpolation. As for any node with a support domain intercepting with a region interface, update of field values needs to access the current field values at some of the nodes that fall into the another region; in this case, it is more convenient to recast the explicit RPIM update equations into a format of matrix equation and combine it with the matrix equation derived from the implicit leapfrog ADI-RPIM scheme. More specifically, combination of (4) with (15), and (5) with (16) yields two new matrix equations expressed as

$$\mathbf{AE}_x^{n+\frac{1}{2}} = \mathbf{AE}_x^{n-\frac{1}{2}} + \mathbf{BH}_z^n - \mathbf{CH}_y^n + \mathbf{\Psi}_E, \tag{16}$$

and $$\mathbf{MH}_z^{n+1} = \mathbf{MH}_z^n + \mathbf{DE}_x^{n+\frac{1}{2}} - \mathbf{GE}_y^{n+\frac{1}{2}} + \mathbf{\Psi}_H, \tag{17}$$

where entries of coefficient matrices A, B, C, M, D and G, and auxiliary vector ψ due to the CPML can be found from (4) to (16).

V. NUMERICAL EXPERIMENTS

A. 5-Pole H-Plane Iris Filter

The return loss of a bandpass waveguide iris filter was computed to illustrate the numerical efficiency of the hybrid meshless method presented here. The filter was based on a WR-28

rectangular waveguide for millimeter-wave applications. It consists of 5 cavities formed with 6 sets of thin perpendicular conductive walls. To evaluate performance of the filter under single-mode propagation, a plane source with TE_{10} field distribution was used to excite TE_{10} mode. The sensor nodes were placed at a short distance from the sources to record electric field component E_z. The geometry and solution domain setup of the problem are shown in Fig. 2, whereas the dimension of the filter is given in Table 1.

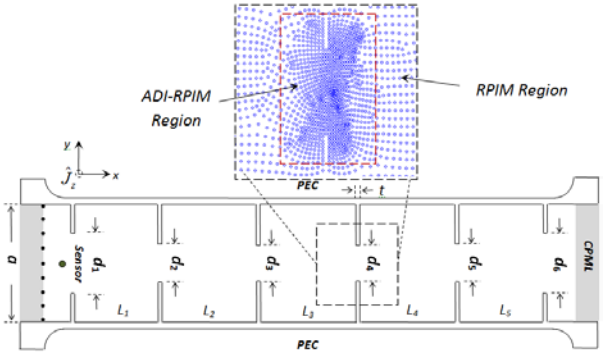

Fig. 2. A 5-pole H-plane iris filter (WR-28 waveguide).

Table 1: Dimension of the iris filter (inches)

a	t	L_1	L_2	L_3	L_4	L_5
0.28	0.008	0.169	0.187	0.192	0.187	0.169
d_1	d_2	d_3	d_4	d_5	d_6	
0.127	0.082	0.077	0.077	0.082	0.127	

Here a is the width of the WR-28 rectangular waveguide, t is the thickness of the irises, L_i specifies the space between two adjacent irises, and d_i defines the gap between a set of irises.

Due to the small dimension of the thin iris, a very fine uniform grid will be needed to discretize the entire problem when the conventional FDTD is used; this yields a significant number of unknowns to be solved with large computational effort. However, with the multi-scale modeling capability of the meshless RPIM, a set of densely distributed nodes can now be placed in the regions around thin walls for refined solutions; the rest of the problem domain remains represented with uniformly distributed coarse nodes, as shown in Fig. 2.

Then, a computational sub-domain is defined to enclose those densely distributed nodes where the field values are updated with unconditionally stable ADI-RPIM scheme. The rest of the domain is still solved with the original RPIM method.

To accurately assess the S11 values of the iris filter shown in Fig. 2, a reference problem with the same nodal discretization but with the irises removed and top/bottom PECs replaced by CPML layers is also simulated. The total electric field recorded at the sensor point due to the iris walls is Fourier transformed to the frequency domain and compared with the incident field computed from the reference problem to determine the reflected field and thus the numerical reflection at *port1*.

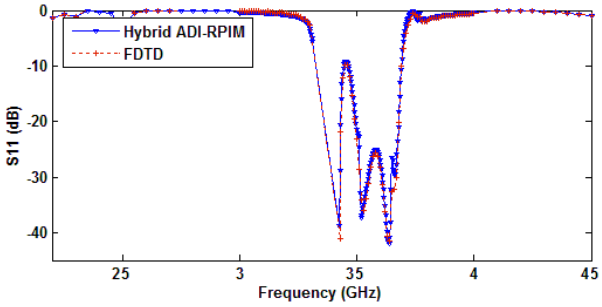

Fig. 3. Computed S11 parameters of 5-pole H-plane iris filter.

Figure 3 shows the computed S11 values for the frequency sweep from 22 GHz to 45 GHz. As can be seen, the results solved with the proposed hybrid meshless scheme agree well with the reference solution from the conventional FDTD with a fine grid; both indicate a good performance of the filter design with the center frequency of 35.2GHz and the bandwidth of 3.2GHz; the reflection in the pass band is lower than -10dB.

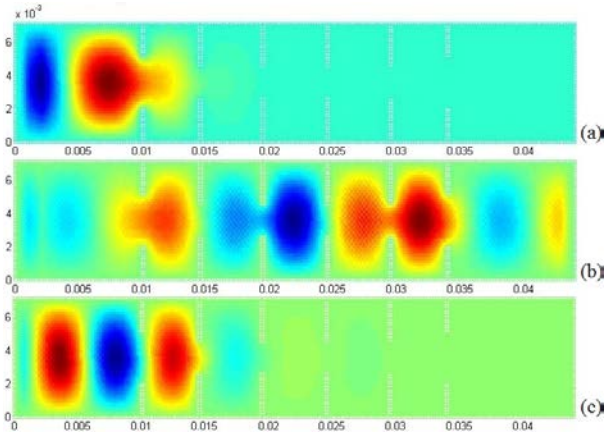

Fig. 4. E-field distributions at different frequencies (after 20000 time-steps), (a) at 30 GHz (below the low end of the pass band); (b) 35.5 GHz (inside the pass band); (c) 40 GHz (beyond the pass band).

Figure 4 presents the graphical displays of E-field distribution along the waveguide filter after 20000 time iterations at different frequencies. As clearly seen, within the pass-band, the steady-state TE_{10} mode propagation is established with little reflection, whereas outside the pass-band, the E-field attenuates and eventually vanishes as it propagates away from the sources.

B. Substrate Integrated Waveguide (SIW)

The second example was the simulation of the steady-state transmission mode of a single-layer substrate integrated waveguide (SIW). Figure 5 shows the geometrical design and fundamental parameters of the SIW under study. For illustration purposes, a standard substrate for high speed digital applications, N-4000-13, with ε_r = 3.6 and height h = 16 mil, was used.

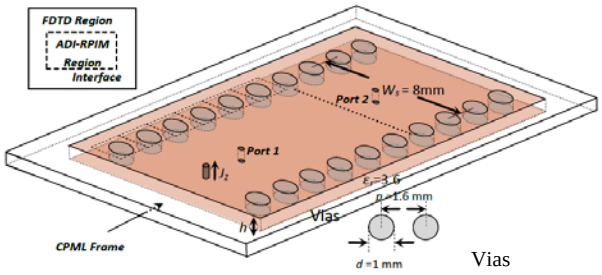

Fig. 5. A 2D substrate integrated waveguide.

In principle, the substrate integrated waveguide emulates a dielectric-filled waveguide with lateral walls formed by rows of vias that are sufficiently close to each other. If properly designed, the behavior of a SIW is similar to that of a conventional rectangular waveguide. The theoretical cutoff frequency of the SIW shown in Fig. 5 was found to be around 10GHz with the following formulae from [18]:

$$f_c = \frac{c}{2W_d\sqrt{\varepsilon_r}}, \text{ and } W_d = W_s - \frac{d^2}{0.95p} + 0.1\frac{d^2}{W_s} \quad (18)$$

where c is the speed of light, ε_r is the dielectric constant, W_s is the width of the waveguide, W_d is the effective width of the guide, d the diameter of the via, and p is distance between the vias.

Since the SIW can only support TE_{m0} modes due to dielectric gaps created by the via separations, a vertically oriented probe was used to excite the waveguide. The uniform current density along the probe was expressed with a ramped sinusoidal function (20). The duration of the ramp function was set to be six cycles of the sinusoidal pulse to eliminate the switch-on noise. The long-time response of the waveguide to such an excitation was approximately monochromatic.

$$J_z(t) = R(t-2T_0)\cdot\sin(2\pi f_0(t-2T_0))\hat{z}. \quad (19)$$

The ratio of voltages at port 1 and port 2 indicates the transmission behavior of the SIW under study and it was firstly examined. The time-domain profiles of electric field along the two ports were recorded up to 30000 time iterations and Fourier-transformed to obtain the corresponding frequency responses; and then line-integrations were performed along the ports to obtain the voltage values at the two ports. As can be seen from Fig. 6, the results computed with the hybrid approach are in good agreement with the reference solution from the FDTD, both indicating a cut-off frequency of 10GHz for the dominant mode (TE_{10}) of the SIW.

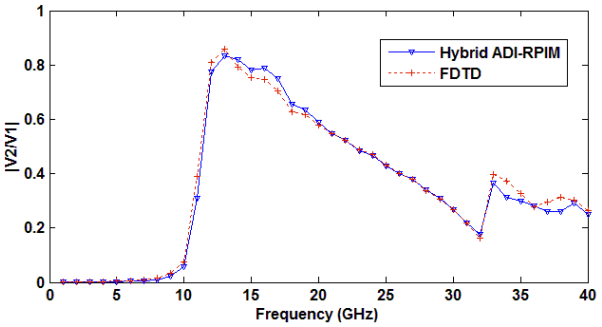

Fig. 6. Ratio of voltages across two ports (1-40 GHz).

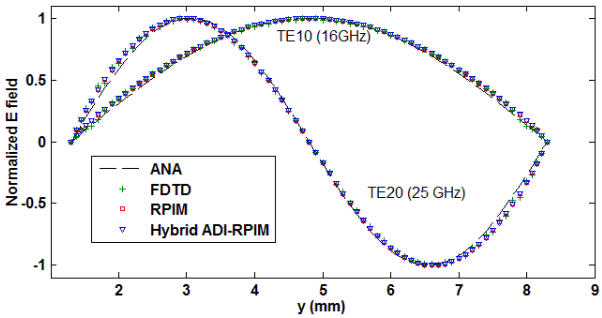

Fig. 7. Normalized electric field along the line of observation points.

The steady-state field distribution over the SIW for higher TE modes was also examined. To launch a TE_{20} propagating mode along the SIW, the waveguide was excited with two probes, which were positioned at 1/4 and 3/4 of the width of the waveguide, in an anti-phase manner. Figure 7

shows the normalized electric field along the line of observation points depicted in Fig. 6 for different TE modes. The computed results are compared with the ones from the FDTD of a fine uniform grid, the original RPIM and the analytical values from an equivalent dielectric filled rectangular waveguide. Good agreements are observed.

Figure 8 presents snapshots of steady-state E field distribution over the SIW for other TE modes, computed with proposed hybrid ADI-RPIM approach after 500,000 time steps. As can been seen, the results do not suffer from late-time instability and there are no noticeable reflections from the dense/coarse region interface that often exist in a conventional sub-gridding scheme with additional interpolation at the region interface.

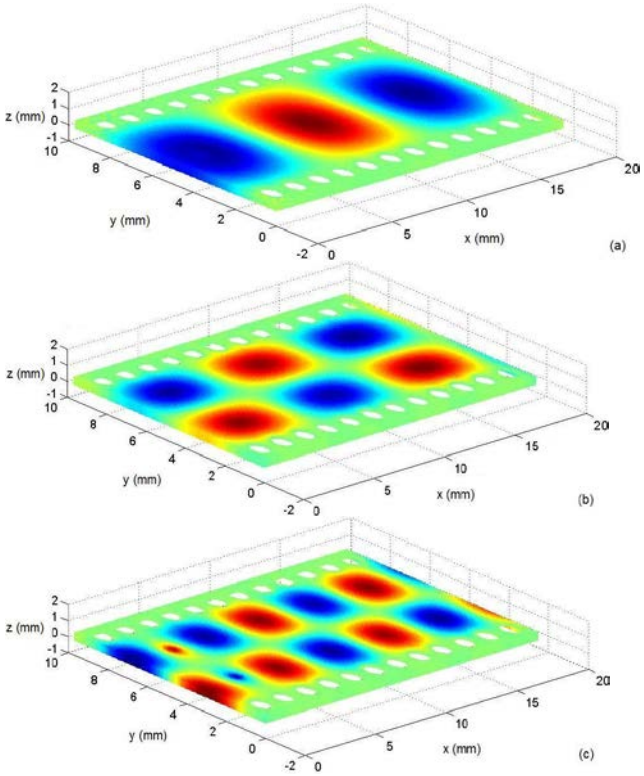

Fig. 8. Steady-state TE mode propagation over the substrate integrated waveguide, (a) TE_{10} mode at 16 GHz; (b) TE_{20} mode at 25 GHz; (c) TE_{20} mode at 30 GHz.

VI. COMPUTATIONAL EXPENDITURE

To quantify the numerical performance of the proposed hybrid ADI-RPIM meshless approach, computational expenditure of the first numerical example is monitored and tabulated in Table 2. The original RPIM, the ADI-RPIM, along with the orthogonal FDTD are included for comparison. As clearly seen, all three meshless methods outperform the conventional FDTD in CPU time as expected; with the FDTD method, a very fine uniform grid is needed to discretize the entire solution domain due to the small dimension of the thin iris; this yields a very large number of total number of unknowns to be solved.

Among the three meshless methods, it is interesting to observe that the pure non-hybrid leapfrog ADI-RPIM does not significantly reduce the CPU run-time and the efficiency gained from its unconditionally stability is compromised by the additional computational cost required for matrix assembly of extra off-diagonal terms and matrix computation during the time-marching. However, the proposed hybrid approach not only saves more than 50% of the memory required by a pure non-hybrid unconditionally stable ADI-RPIM but also runs 100% faster.

Table 2: Computational expenditure of example A

	FDTD	RPIM	ADI-	Hybrid
Unknowns	176562	34581	34581	34581
CPU time (sec.)	512	125	121	56
Memory (Mbs)	364	111	319	152
CPU gain	1	3.0	3.2	8.1

VII. CONCLUSION

The presented hybrid ADI-RPIM approach further improves the computational efficiency of the meshless RPIM technique for solving problems with fine geometric features. With the unconditionally stable ADI-RPIM method only applied to the computational regions that require fine discretization (to describe abrupt changes in field values or geometrical details), CPU, and memory overhead due to implicit updates of field variables are minimized, which in turn renders a CPU gain over the original RPIM meshless method. In addition, time-steps at different computational regions can be synchronized without temporal interpolation; as well, the underlying point interpolating nature of the RPIM method obviates the need of additional spatial interpolation at region interfaces. The numerical experiments show the proposed hybrid meshless approach remains numerically stable after half a million time iterations.

ACKNOWLEDGMENT

The work was supported in part by the National Natural Science Foundation of China (NSFC) fund under contract 61061003 and Natural Science and Engineering Research Council of Canada under contract 155230-07.

REFERENCES

[1] R. K. Gordon and W. E. Hutchcraft, "The Use of Multiquadric Radial Basis Functions in Open Region Problems," *Applied Computational Electromagnetics Society (ACES) Journal*, vol. 21, no. 2, pp. 127 – 134, July 2006.

[2] A. B. Ali, E. A. Hajlaoui, and A. Gharsallah, "Efficient Analysis Technique for Modeling Periodic Structures Based on Finite Element Method using High-Order Multiscalets Functions," *Applied Computational Electromagnetics Society (ACES) Journal*, vol. 25, no. 9, pp. 755 - 763, September 2010.

[3] J. G. Wang and G. R. Liu, "A Point Interpolation Meshless Method Based on Radial Basis Functions*," Int. J. Numer. Methods Eng*., 2001.

[4] S. J. Lai, B. Z. Wang, and Y. Duan, "Meshless Radial Basis Function Method for Transient Electromagnetic Computations," *IEEE Trans. Magnetics*, vol. 44, no. 10, pp. 2288-2295, 2008.

[5] T. Kaufmann, C. Fumeaux, and R. Vahldieck, "The Meshless Radial Point Interpolation Method for Time-Domain Electromagnetic," *IEEE MTT-S Int. Microwave Symp. Dig.*, Atlanta GA, pp. 61-64, June 15-20, 2008.

[6] S. J. Lai, B. Z. Wang, and Y. Duan, "Solving Helmholtz Equation by Meshless Radial Basis Functions Method," *Progress In Electromagnetics Research B*, vol. 24, pp. 351-367, 2010.

[7] Y. Yu and Z. Chen, "A Three-Dimensional Radial Point Interpolation Method for Meshless Time-Domain Modeling," *IEEE Trans. Microwave Theory & Techniques*, vol. 57, no. 8, pp. 2015-2020, 2009.

[8] Y. Yu and Z. Chen, "Meshless RPIM Modeling of Open-Structures using PMLs," *IEEE MTT-S Int. Microwave Symp. Dig.*, Anaheim, May 23-28, 2010.

[9] Y. Yu and Z. Chen, "Implementation of Material Interface Conditions in the Radial Point Interpolation Meshless Method," *IEEE Trans. Antennas and Propagation*, vol. 59, no. 8, pp. 2916-2923, 2011.

[10] Y. Yu and Z. Chen, "Towards the Development of Unconditionally Stable Time-Domain Meshless Numerical Methods," *IEEE Trans. Microwave Theory and Techniques*, vol. 58, no. 3, pp. 578-586, 2010.

[11] T. Kaufmann, Y. Yu, C. Engström, Z. Chen, and C. Fumeaux "Recent Developments of the Meshless Radial Point Interpolation Method for Time-Domain Electromagnetics," *International Journal of Numerical Modelling: Electronic Networks, Devices and Fields*, Article first published online :, DOI: 10.1002/jnm.1830, Feb. 15, 2012.

[12] S. J. Cooke, M. Botton, T. M. Antonsen, and B. Levush, "A Leapfrog Formulation of the 3D ADI-FDTD Algorithm," *Intl. Workshop on Computational Electromagnetics in Time-Domain*, , pp. 1-4, Oct. 15-17, 2007

[13] F. Zhen, Z. Chen, and J. Zhang, "Toward the Development of a Three-Dimensional Unconditionally Stable Finite Difference Time-Domain Method," *IEEE Trans. Microwave Theory & Techniques*, vol. 48, no. 9, pp. 1550-1558, Sept. 2000.

[14] T. Namiki, "3-D ADI-FDTD Method--Unconditionally Stable Time-Domain Algorithm for Solving Full Vector Maxwell's Equations," *IEEE Trans. Microwave Theory & Techniques*, vol. 48, no. 10, pp. 1743-1748, Oct. 2000.

[15] J. Chen and J. Wang, "An Unconditionally Stable Subcell Model for Thin Wires in the ADI-FDTD Method," *Applied Computational Electromagnetics Society (ACES) Journal*, vol. 25, no. 8, pp. 659 - 664, August 2010.

[16] J. A. Roden and S. D. Gedney, "Convolutional PML (CPML): An Efficient FDTD Implementation of the CFS-PML for Arbitrary Media," *Microwave Opt. Technol. Lett.*, vol. 27, pp. 334-339, Dec. 5, 2000.

[17] S. D. Gedney, G. Liu, J. Alan Rodden, and A. Zhu, "Perfectly Matched Layer Media with CFS for an Unconditionally Stable ADI-FDTD Method," *IEEE Trans. Antennas & Propagation*, vol. 49, no. 11, pp. 1554-1559, 2001.

[18] F. Xu and K. Wu, "Guided-Wave and Leakage Characteristics of Substrate Integrated Waveguide," *IEEE Trans. Microwave theory & techniques*, vol. 53, no. 3, pp. 66-73, 2005.

Yiqiang Yu (M'09) received the M.Sc. degree (with distinction) in communication systems in 2003 and Ph.D. in microwave engineering in 2007 from Swansea University, U.K.

He is presently a full Professor with East China Jiaotong University. He is also a Research Fellow with the Department of Electrical and Computer Engineering, Dalhousie University, Halifax, Canada.

His primary interest is in applications of computational electromagnetics, in particular use of finite-difference methods, method of moments, and fast multipole methods in both the time and frequency domains. His interests also include RF/microwave components design, antennas design and measurement, EMI/EMC analysis and testing, and iterative solvers and preconditioning techniques for large-scale matrix computation.

Dr. Yu was a recipient of the Overseas Research Scholarship from the United Kingdom Overseas Research Award Program during 2004–2007.

Zhizhang (David) Chen (S'92-M'92–SM'96–F'10) received the Ph.D. degree from the University of Ottawa, ON, Canada.

He was a NSERC Postdoctoral Fellow with the ECE Department of McGill University, Montreal, Canada. He joined Dalhousie University, Halifax, Canada, in 1993, where he is presently a Professor. He has authored and coauthored over 200 journal and conference papers in computational electromagnetics and RF/microwave electronics. He was one of the originators in developing new numerical algorithms (including ADI-FDTD method) and in designing new classes of compact RF front-end circuits for wireless communications. His current research interests include numerical modeling and simulation, RF/microwave electronics, smart antennas, and wireless transceiving technology and applications.

Dr. Chen received the 2005 Nova Scotia Engineering Award, a 2006 Dalhousie graduate teaching award, 2006 ECE Professor of the Year award and the 2007 Faculty of Engineering Research Award from Dalhousie University.

Efficient Marching-on-in-Degree Solver of Time Domain Integral Equation with Adaptive Cross Approximation Algorithm-Singular Value Decomposition

Huan-huan Zhang, Quan-quan Wang, Yi-fei Shi, and Ru-shan Chen

Department of Communication Engineering
Nanjing University of Science and Technology, Nanjing 210094, Jiangsu, China
zhanghuanajkd@hotmail.com, eechenrs@mail.njust.edu.cn

Abstract ─ Adaptive cross approximation algorithm with singular value decomposition postcompression (ACA-SVD) is introduced into the marching-on-in-degree solver of time domain integral equation for the analysis of transient electromagnetic scattering from perfect electric conductor (PEC). The computational domain is divided into multilevel groups based on octree. ACA-SVD algorithm is utilized to compute the impedance matrices associated with the well-separated groups at each level. Whereas, the impedance matrices formed by self and neighboring groups are calculated entirely in the traditional manner. Numerical results demonstrate that the proposed method can greatly reduce the memory requirement and matrix-vector product (MVP) time per iteration.

Index Terms ─ Time domain integral equation, marching-on-in-degree, transient scattering, adaptive cross approximation algorithm, singular value decomposition.

I. INTRODUCTION

In recent years, the direct time domain methods has attracted extensive attention in calculating transient electromagnetic problems, which is due to the increasing interest in target identification, short pulse radar design, or other related applications. Several common time domain methods are finite-difference time domain (FDTD) method, time domain finite-element (TDFE) method, finite-volume time domain (FVTD) method and time domain integral equation (TDIE) method, among which the TDIE method is more suitable for analysis of electromagnetic scattering and radiation problems in homogeneous medium because it only needs surface meshing and does not need absorbing boundary condition. There are two popular approaches to solve TDIE. One is the marching-on-in-time (MOT) method [1], [2], and the other is the marching-on-in-degree (MOD) method [3]-[6]. The proposed method in this paper is based on the MOD solver of TDIE.

The MOD method uses causal weighted Laguerre polynomials as temporal basis and testing functions. Due to the property of weighted Laguerre polynomials [7], [8], this method does not involve late-time instability. However, the conventional MOD method requires much more memory and CPU time than that of MOT method [9], which precludes its application in large scale problems. Moreover, the plane wave time domain (PWTD) algorithm, developed at Michelssen's group at Urbana-Champaign, can reduce the CPU time and memory requirements of MOT to $O(N_tN_s log^2 N_s)$ and $O(N_tN_s)$ respectively [10]. In order to improve the capability of MOD method, several accelerating techniques have been applied, such as fast Fourier transform (FFT) [11], UV method [12], and so on. The FFT-based MOD utilizes the spatial translational invariance nature of the Green's function and reduces the computational cost and the storage requirements respectively to $O(N_t^2 N_s log N_s)$ and $O(N_tN_s)$, where N_s and N_t denote the number of spatial and temporal basis functions. But the FFT method applied in [11] requires uniform mesh of the object. The UV method is utilized in [12] to reduce both the memory requirement and CPU time per interaction to $O(N_s^{4/3} log N_s)$.

Submitted On: Nov. 16, 2011
Accepted On: May 3, 2012

The adaptive cross approximation (ACA) algorithm was developed by Bebendorf [13] and is widely used to solve electromagnetic wave problems with moderate electric size [14-16]. It is a purely algebraic and therefore, kernel independent algorithm. In this paper, ACA algorithm with singular value decomposition (SVD) postcompression [17] is applied to the MOD solver of TDIE. Numerical results show that the proposed method can greatly reduce the memory requirement and matrix-vector product (MVP) time per iteration.

The remainder of this paper is organized as follows. Section II describes the marching-on-in-degree solver of time domain combined field integral equation (TD-CFIE). Section III gives the details about the acceleration of MOD with ACA-SVD algorithm. Section IV presents validations and numerical experiments. Section V gives some conclusions.

II. MARCHING-ON-IN-DEGREE SOLVER OF TD-CFIE

A. TD-CFIE

Considering that a PEC scatterer is illuminated by a transient electromagnetic field. The induced current on the conducting surface is denoted as $\mathbf{J}(\mathbf{r},t)$, which satisfies the time domain electric field integral equation (TD-EFIE) and magnetic field integral equation (TD-MFIE):

$$\begin{aligned}\hat{n}\times\hat{n}\times\mathbf{E}^i(\mathbf{r},t) &= \hat{n}\times\hat{n}\times\frac{\mu_0}{4\pi}\frac{\partial}{\partial t}\int_s\frac{\mathbf{J}(\mathbf{r}',\tau)}{R}dS' \\ &\quad -\hat{n}\times\hat{n}\times\frac{\nabla}{4\pi\varepsilon_0}\int_s\int_{-\infty}^{\tau}\frac{\nabla'\bullet\mathbf{J}(\mathbf{r}',t)}{R}dtdS',\end{aligned} \tag{1}$$

$$\hat{n}\times\mathbf{H}^i(\mathbf{r},t)=\frac{\mathbf{J}(\mathbf{r},t)}{2}-\hat{n}\times\nabla\times\int_{s_0}\frac{\mathbf{J}(\mathbf{r}',\tau)}{4\pi R}dS', \tag{2}$$

where $\tau=t-R/c$ is the retarded time, $R=|\mathbf{r}-\mathbf{r}'|$, $\mathbf{r}$ and $\mathbf{r}'$ refer to the position vectors of observation and source point respectively, S_0 denotes the surface without the singularity point at $\mathbf{r}$=$\mathbf{r}'$, $\hat{n}$ is the unit normal vector outward to the conducting surface S.

Using a combination factor α ranging from 0 to 1, we can get the TD-CFIE:

$$\alpha(\textit{TD-EFIE})+(1-\alpha)\eta(\textit{TD-MFIE}), \tag{3}$$

where η is the wave impedance of free space.

B. Spatial and temporal discretization of TD-CFIE

For the expanding of TD-CFIE, we choose RWG basis functions [18] and weighted Laguerre polynomials as spatial and temporal basis functions, respectively. Thus, the surface current density can be discretized as

$$\mathbf{J}(\mathbf{r},t)=\sum_{n=1}^{N_s}\sum_{j=0}^{N_t}\mathrm{J}_{n,j}\mathbf{S}_n(\mathbf{r})\varphi_j(\bar{t}), \tag{4}$$

where $\mathbf{S}_n(\mathbf{r})$ represents the n*th* RWG basis function, $\varphi_j(\bar{t})$ is the j*th* degree weighted Laguerre polynomial

$$\varphi_j(\bar{t})=e^{-\bar{t}/2}L_j(\bar{t}), \tag{5}$$

$\bar{t}=st$, s is the temporal scaling factor and L_j is the j*th* degree Laguerre polynomial

$$L_j(t)=\frac{e^t}{j!}\frac{d^j}{dt^j}\left(t^je^{-t}\right),\ 0\le t<\infty, \tag{6}$$

N_s is the number of spatial basis functions, N_t is the number of temporal basis functions and it is related to time duration T and frequency bandwidth B of the incident wave [3]

$$N_t>2BT+1. \tag{7}$$

Taking (4) into (3) and making the spatial and temporal testing with Galerkin's method, we can obtain

$$\begin{aligned}\sum_{n=1}^{N_s}\sum_{j=0}^{i}\left[sJ_{n,j}^{D}A_{mn}+\frac{2}{s}J_{n,j}^{I}B_{mn}-J_{n,j}D_{mn}\right]\varphi_{i,j}(sR/c) \\ +\sum_{n=1}^{N_s}J_{n,i}C_{mn}=\int_0^{\infty}\varphi_i(\bar{t})R_m d\bar{t},\end{aligned} \tag{8}$$

where

$$\begin{aligned}A_{mn}&=\frac{\alpha\mu_0}{4\pi}\int_s\int_{s'}\frac{S_m(\mathbf{r})\cdot S_n(\mathbf{r}')}{R}dS'dS \\ &\quad -\frac{(1-\alpha)\eta}{4\pi c}\int_s S_m(\mathbf{r})\cdot\hat{n}\times\int_{S_0}S_n(\mathbf{r}')\times\frac{\hat{\mathbf{R}}}{R}dS'dS,\end{aligned} \tag{9}$$

$$B_{mn}=\frac{\alpha}{4\pi\varepsilon_0}\int_s\int_{s'}\frac{\nabla\cdot S_m(\mathbf{r})\nabla'\cdot S_n(\mathbf{r}')}{R}dS'dS, \tag{10}$$

$$C_{mn}=\frac{(1-\alpha)\eta}{2}\int_s S_m(\mathbf{r})\cdot S_n(\mathbf{r}')dS, \tag{11}$$

$$D_{mn}=\frac{(1-\alpha)\eta}{4\pi}\int_s S_m(\mathbf{r})\cdot\hat{n}\times\int_{S_0}S_n(\mathbf{r}')\times\frac{\hat{\mathbf{R}}}{R^2}dS'dS, \tag{12}$$

$$\begin{aligned}R_m&=\alpha\int_s S_m(\mathbf{r})\cdot\mathbf{E}^i(\mathbf{r},t)dS \\ &\quad +(1-\alpha)\eta\int_s S_m(\mathbf{r})\cdot\hat{n}\times\mathbf{H}^i(\mathbf{r},t)dS,\end{aligned} \tag{13}$$

$$\varphi_{i,j}(sR/c)=\varphi_{i-j}(sR/c)-\varphi_{i-j-1}(sR/c), \tag{14}$$

$$J_{n,j}^{D} = 0.5J_{n,j} + \sum_{k=0}^{j-1} J_{n,k}, \tag{15}$$

$$J_{n,j}^{I} = J_{n,j} + 2\sum_{k=0}^{j-1} J_{n,k}\left(-1\right)^{j+k}. \tag{16}$$

Making the $i=j$ terms at left and the $i<j$ terms at right, we can rewrite (8) in matrix form

$$\left[\mathbf{Z}_{mn}\right]\left\{J_{n,i}\right\} = \left\{\mathbf{V}_{m,i}\right\} + \left\{\mathbf{P}_{m,i}\right\}, \tag{17}$$

where

$$\mathbf{Z}_{mn} = \left[0.5sA_{mn} + \frac{2}{s}B_{mn} - D_{mn}\right]e^{\frac{-sR}{2c}} + C_{mn}, \tag{18}$$

$$\mathbf{V}_{m,i} = \int_0^{\infty} \varphi_i\left(\bar{t}\right) R_m d\bar{t}, \tag{19}$$

$$\begin{aligned}\mathbf{P}_{m,i} = -\sum_{j=0}^{i-1}\Bigg[& sJ_{n,j}^{D}A_{mn} + \frac{2}{s}J_{n,j}^{I}B_{mn} - J_{n,j}D_{mn}\Bigg]\varphi_{i,j}\left(sR/c\right) \\ & -\Bigg[s\sum_{k=0}^{i-1} J_{n,k}A_{mn} + \frac{2}{s}\left(2\sum_{k=0}^{i-1} J_{n,k}\left(-1\right)^{j+k}\right)B_{mn}\Bigg]e^{\frac{-sR}{2c}}.\end{aligned} \tag{20}$$

Equation (17) is a recursion equation and can be solved degree by degree to obtain the current coefficients $\left\{J_{n,i}\right\}$.

III. ACCELERATION OF MOD WITH ACA-SVD ALGORITHM

Based on the knowledge of Section II, it can be discovered that four kinds of matrices $\mathbf{M}_1$, $\mathbf{M}_2$, $\mathbf{M}_3$, $\mathbf{M}_4$ need to be constructed and stored for the implementation of MOD-TDCFIE, where

$$\mathbf{M}_{1,mn} = \mathbf{Z}_{mn} = \left[0.5sA_{mn} + \frac{2}{s}B_{mn} - D_{mn}\right]e^{\frac{-sR}{2c}} + C_{mn}, \tag{21}$$

$$\mathbf{M}_{2,mn,k} = sA_{mn}\phi_{k,k-1}\left(sR/c\right), \quad k = 0,1,2,\cdots,N_t \tag{22}$$

$$\mathbf{M}_{3,mn,k} = \frac{2}{s}B_{mn}\phi_{k,k-1}\left(sR/c\right), \quad k = 0,1,2,\cdots,N_t \tag{23}$$

$$\mathbf{M}_{4,mn,k} = D_{mn}\phi_{k,k-1}\left(sR/c\right), \quad k = 0,1,2,\cdots,N_t \tag{24}$$

$$\phi_{k,k-1}\left(sR/c\right) = \begin{cases} e^{\frac{-sR}{2c}} & k = 0 \\ \varphi_k\left(sR/c\right) - \varphi_{k-1}\left(sR/c\right) & k \in \left[1, N_t\right]. \end{cases} \tag{25}$$

$\mathbf{M}_1$ refers to the impedance matrix at present degree. $\mathbf{M}_2$, $\mathbf{M}_3$, $\mathbf{M}_4$ represent the differential, integral and normal term of each degree, respectively. There are totally $N_s \times N_s \times \left[1+3\times\left(1+N_t\right)\right]$ matrices to be stored. Because each of these matrices is handled in the same manner, we only take $\mathbf{M}_{1,mn}$ as an example in the rest of this section to introduce the combination of ACA-SVD with MOD method.

The ACA-SVD algorithm needs a multilevel grouping of the computational domain. The grouping pattern based on octree, which is popularly used in the multilevel fast multipole algorithm [19-21] is adopted in this paper. The coupling of self and neighboring groups at some level are computed directly and the whole submatrices with elements (21) are stored. Whereas, the submatrices associated with two well-separated groups are evaluated and stored with ACA-SVD algorithm. Considering two well-separated groups, the interaction between them will lead to a rank-deficient submatrix $\mathbf{M}_1^{p\times q}$, where p and q are the number of basis functions in the two groups, the superscript $p\times q$ represents the size of the submatrix, the digit 1 of the subscript refers to the kind of matrix $\mathbf{M}_1$. We firstly use ACA algorithm to approximate submatrix $\mathbf{M}_1^{p\times q}$ with $\left[\mathbf{U}_1^{p\times r_1}\right]\left[\mathbf{W}_1^{q\times r_1}\right]^T$, where r_1 is the rank of matrix $\mathbf{M}_1^{p\times q}$, [ ] notation is used to represent a column matrix. With moderately grouping in the application, the rank r_1 is always smaller than p and q [14]. Because the columns of the matrices $\left[\mathbf{U}_1^{p\times r_1}\right]$ and $\left[\mathbf{W}_1^{q\times r_1}\right]$ generated by ACA are usually not orthogonal, we can use SVD algorithm to further remove the redundancies contained in them. Assume that the QR decompositions of them are

$$\left[\mathbf{U}_1^{p\times r_1}\right] = \left[\mathbf{Q}_u^{p\times r_1}\right]\left[\mathbf{R}_u^{r_1\times r_1}\right], \tag{26}$$

$$\left[\mathbf{W}_1^{q\times r_1}\right] = \left[\mathbf{Q}_w^{q\times r_1}\right]\left[\mathbf{R}_w^{r_1\times r_1}\right]. \tag{27}$$

The product of matrices $\left[\mathbf{R}_u^{r_1\times r_1}\right]$ and $\left[\mathbf{R}_w^{r_1\times r_1}\right]^T$ is then decomposed by SVD algorithm:

$$\left[\mathbf{R}_u^{r_1\times r_1}\right]\left[\mathbf{R}_w^{r_1\times r_1}\right]^T = \left[\tilde{\mathbf{U}}^{r_1\times r_1}\right]\left[\tilde{\Sigma}^{r_1\times r_1}\right]\left[\tilde{\mathbf{V}}^{r_1\times r_1}\right]^T \tag{28}$$

Discarding the columns of $\left[\tilde{\mathbf{U}}^{r_1\times r_1}\right]$ and $\left[\tilde{\mathbf{V}}^{r_1\times r_1}\right]^T$ corresponding to negligible singular values, we can obtain

$$\left[\mathbf{R}_u^{r_1\times r_1}\right]\left[\mathbf{R}_w^{r_1\times r_1}\right]^T = \left[\bar{\mathbf{U}}^{r_1\times \bar{r}_1}\right]\left[\bar{\Sigma}^{\bar{r}_1\times \bar{r}_1}\right]\left[\bar{\mathbf{V}}^{r_1\times \bar{r}_1}\right]^T, \tag{29}$$

where the upper horizontal bar denotes an approximate version of the corresponding matrix.

Finally, the decomposition of matrix $\left[\mathbf{M}_1^{p\times q}\right]$ can be rewritten as

$$\begin{aligned}\left[\mathbf{M}_1^{p\times q}\right]&=\left[\mathbf{U}_1^{p\times r_1}\right]\left[\mathbf{W}_1^{q\times r_1}\right]^T\\&=\left[\mathbf{Q}_u^{p\times r_1}\right]\left[\bar{\mathbf{U}}^{r_1\times \bar{r}_1}\right]\left[\bar{\sum}^{\bar{r}_1\times \bar{r}_1}\right]\left[\bar{\mathbf{V}}^{r_1\times \bar{r}_1}\right]^T\left[\mathbf{Q}_{\mathrm{w}}^{q\times r_1}\right]^T\\&=\left[\mathbf{X}_1^{p\times \bar{r}_1}\right]\left[\mathbf{Y}_1^{\bar{r}_1\times q}\right],\end{aligned}\quad(30)$$

where

$$\left[\mathbf{X}_1^{p\times \bar{r}_1}\right]=\left[\mathbf{Q}_u^{p\times r_1}\right]\left[\bar{\mathbf{U}}^{r_1\times \bar{r}_1}\right]\left[\bar{\sum}^{\bar{r}_1\times \bar{r}_1}\right],\quad(31)$$

$$\left[\mathbf{Y}_1^{\bar{r}_1\times q}\right]=\left[\bar{\mathbf{V}}^{r_1\times \bar{r}_1}\right]^T\left[\mathbf{Q}_{\mathrm{w}}^{q\times r_1}\right]^T.\quad(32)$$

Because $\bar{r}_1 < r_1$, the storage requirement of $\left[\mathbf{X}_1^{p\times \bar{r}_1}\right]$ and $\left[\mathbf{Y}_1^{\bar{r}_1\times q}\right]$ is smaller than $\left[\mathbf{U}_1^{p\times r_1}\right]$ and $\left[\mathbf{W}_1^{q\times r_1}\right]^T$.

It is obvious that if we compute the submatrices $\mathbf{M}_1$, $\mathbf{M}_2$, $\mathbf{M}_3$, $\mathbf{M}_4$ of two well-separated groups directly at each degree, we will need to store $\mathrm{p}\times\mathrm{q}\times\left[1+3\times\left(1+N_t\right)\right]$ elements. However, if we evaluate the submatrix degree by degree with ACA-SVD algorithm, we only need to store $(p+q)\bar{r}_1+\sum_{m=2}^{4}\sum_{k=0}^{N_t}(p+q)\bar{r}_{\mathrm{m},k}$ elements. $\bar{r}_{\mathrm{m},k}$ is usually smaller than *p* and *q*, so the application of ACA-SVD to MOD can greatly reduce the memory requirement.

IV. NUMERICAL RESULTS

Several numerical experiments are carried out to validate the accuracy and efficiency of the proposed method. The combination factor α of TD-CFIE is set to be 0.5 for closed bodies. ACA terminating tolerance is set to be 10^{-3} unless noted otherwise. The temporal scaling factor of the weighted Laguerre polynomials is 1.2×10^9. All experiments are performed on 2.67GHz CPU and 48 GB RAM.

The incident pulse used in all the following examples is a modulated Gaussian pulse which is defined as

$$\mathbf{E}^i(\mathbf{r},t)=\hat{e}_x\cos\left(2\pi f_0\tau\right)\exp\left[-\left(\tau-t_p\right)^2/2\sigma^2\right],\quad(33)$$

where f_0 is the central frequency, $\tau=t-\hat{k}\bullet\mathbf{r}/c$, $\hat{k}$ refers to the propagation direction of incident wave and is along *z* direction in our examples, $\hat{e}_x$ is the unit vector along *x* axis and represents the polarization of the incident wave, $t_p=3.5\sigma$, $\sigma=6/\left(2\pi f_{bw}\right)$, f_{bw} denotes the bandwidth of the incident pulse.

A. Accuracy

Three examples are given to show the accuracy of the proposed method. As the first example, we consider a PEC plate with 1.4m side length, which lies in the *xoy* plane and is centered at the origin. The problem is discretized into 1044 edges. 50 temporal basis functions and single level ACA-SVD are used. The modulated Gaussian pulse parameter is chosen as f_0 = 150MHz and f_{bw} = 300MHz. Based on the proposed method, equation (17) is solved to obtain the current coefficients $\left\{J_{n,i}\right\}$. Then, the current at the n*th* edge in time domain can be calculated as

$$\mathrm{J}_n(t)=\sum_{j=0}^{N_t}\mathrm{J}_{n,j}\varphi_j(\bar{t}).\quad(34)$$

Finally, current at a randomly chosen inner edge is compared with the results obtained by inverse discrete Fourier transform (IDFT) of the frequency domain data as shown in Fig. 1. The frequency domain data is computed by method of moments (MoM). The two endpoints of the inner edge are (0.1499, -0.0037, 0) and (0.1531, -0.0856, 0).

A PEC cylinder with radius of 0.5m and height of 3m is analyzed as the second example. The problem is discretized into 5856 edges. 90 temporal basis functions and two levels ACA-SVD are adopted. The modulated Gaussian pulse parameter is the same as that of the first example. After the current coefficients are obtained, the time domain far-field data is computed and transformed into frequency domain. Then it is normalized by the incident wave. Finally, the wideband bistatic RCS can be obtained. Results at several frequencies are given and compared with that of MoM. It can be observed in Fig. 2 that RCS data obtained from MOD-ACA-SVD agrees well with that of MoM. In order to present the influence of terminating tolerance to the accuracy of proposed method, the relative error of wideband bistatic RCS with the terminating tolerance of 10^{-1}, 10^{-2}, 10^{-3} is shown in Fig. 3. The relative error of RCS at certain observation angle is defined as

$$\text{Relative error}=\left|\frac{RCS^{MOD-ACA-SVD}-RCS^{\mathrm{Ref}}}{RCS^{\mathrm{Ref}}}\right|\times100\%,$$

where $RCS^{MOD-ACA-SVD}$ is the RCS obtained by the proposed method and RCS^{Ref} is the reference results obtained by traditional MOD method. It is acceptable to set the terminating tolerance to be

10^{-3} where the maximum relative error is below 5%.

The third example is a PEC ogive modeled with 8463 edges. The maximum size in the x, y and z directions are 3.81m, 0.76m and 0.76m. Please refer to [22] for detail information about this model. 125 temporal basis functions and three levels ACA-SVD are employed. The modulated Gaussian pulse parameter is chosen as f_0 = 225MHz and f_{bw} = 450MHz in this example. Results at several frequencies are given and compared with that of MoM. Good agreement can be achieved as shown in Fig. 4.

The memory requirement of the proposed method is given in Table 1 and compared with that of the traditional MOD method, which is computed directly by using the formula $N_s \times N_s \times \left[1+3\times(1+N_t)\right]\times 4/1024^3$. The total solution time of the proposed method and MOD method are shown in Table 2. For the example of PEC ogive, the memory requirement of MOD exceeds the available memory and the total solution time can not be obtained. But it can still be computed by the proposed method. So it can be concluded that the traditional MOD method is less useful for large problems though it spends less time than proposed method for small problems.

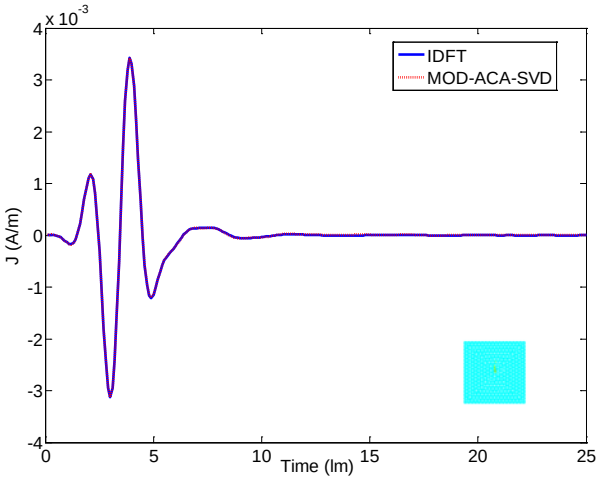

Fig. 1. The current at a randomly chosen inner edge compared with the results obtained by IDFT of the frequency domain data. The unit lm represents light meter and 1 (lm) = 1/light speed in free space (s).

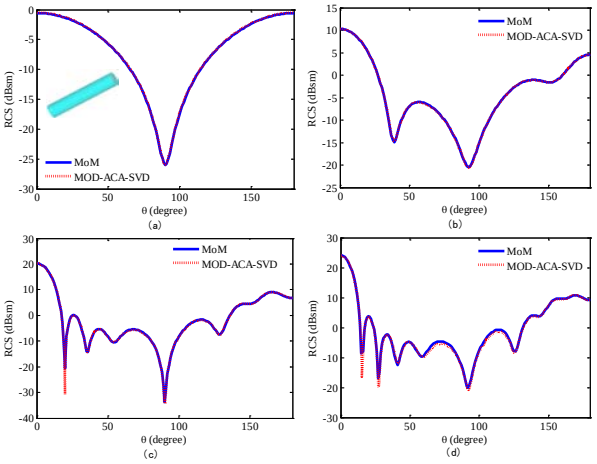

Fig. 2. Bistatic RCS results of a PEC cylinder when Φ = 0: (a) f = 40MHz, (b) f = 110MHz, (c) f = 180MHz, (d) f = 260MHz.

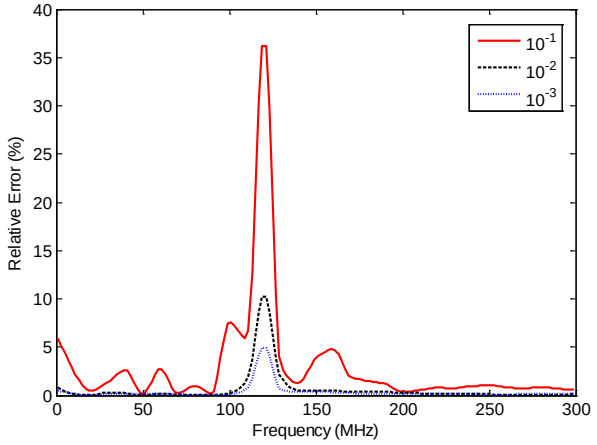

Fig. 3. Relative error of Bistatic RCS with three sets of terminating tolerance when Φ = 0, θ = 0.

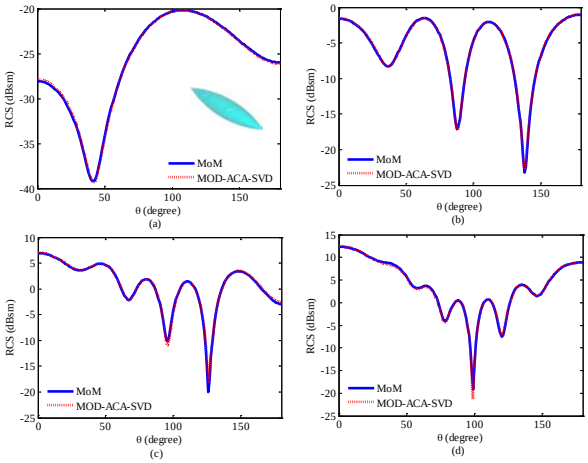

Fig. 4. Bistatic RCS results of a PEC ogive when Φ = 0: (a) f = 45MHz, (b) f = 150MHz, (c) f = 300MHz, (d) f = 390MHz.

Table 1: Memory requirement of three examples

Examples	Memory Requirement (GB)	
	MOD-ACA-SVD	MOD
Plate	0.288	0.428
Cylinder	14.85	35.84
Ogive	32.66	103.55

Table 2: Total solution time of three examples

Examples	Total Solution Time (s)	
	MOD-ACA-SVD	MOD
Plate	410	39
Cylinder	46,040	5,242
Ogive	148,737	–

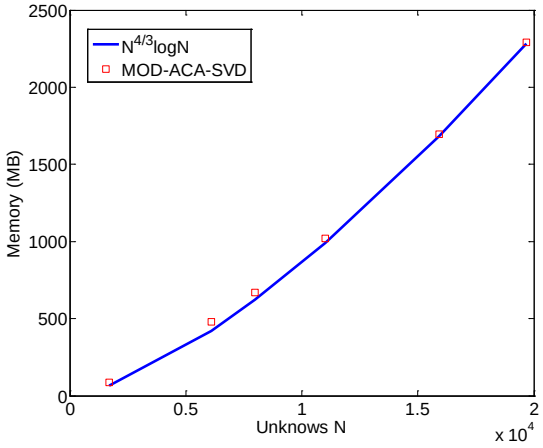

(a)

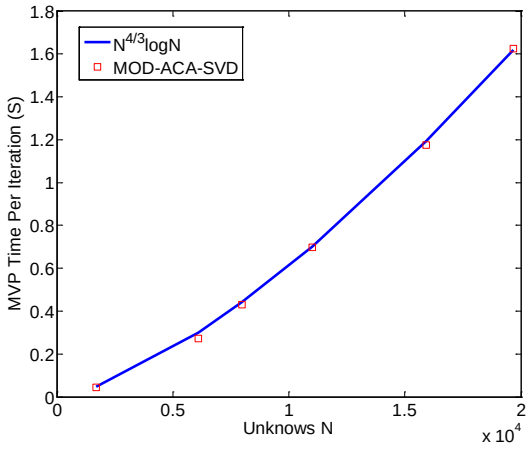

(b)

Fig. 5. Complexity of MOD-ACA-SVD algorithm for a PEC sphere example: (a) memory, (b) MVP time per iteration.

B. Efficiency

In this section, the numerical complexity of the proposed method is explored. A metallic sphere of radius 1 meter centered at the origin and is meshed with different number of edges according to different frequency band of the modulated Gaussian pulse. The highest frequency of the frequency band is increased from 200MHz to 667MHz. The degree of temporal basis functions is chosen to be 0*th* to 3*th* for the sake of available memory. Both the memory requirement and MVP time per iteration with 1692, 6102, 7989, 10998, 15918, and 19674 unknowns are shown in Fig. 5. It can be observed that the complexity of proposed method scales as $N_s^{4/3}\log N_s$ for moderate sized problems.

V. CONCLUSION

The combination of marching-on-in-degree solver of time domain integral equation and adaptive cross approximation algorithm with singular value decomposition postcompression is achieved in this paper. The impedance matrices of each degree related to well-separated groups are compressed by ACA-SVD algorithm. Numerical results show that the method proposed in this paper is very stable and accurate. Moreover, it can greatly reduce the memory requirement and matrix-vector product (MVP) time per iteration of MOD method.

ACKNOWLEDGMENT

The authors would like to thank the support of National Natural Science Foundation of China under Grant No. 60871013 and 60901007. The authors would also like to thank the earnest work of the editors and anonymous reviewers.

REFERENCES

[1] S. M. Rao, D. R. Wilton, "Transient Scattering by Conducting Surfaces of Arbitrary Shape," *IEEE Trans. Antennas Propagat.*, vol. 39, no. 1, pp. 56-61, 1991.

[2] B. Shanker, A. A. Ergin, K. Ayügn, and E. Michielssen, "Analysis of Transient Electromagnetic Scattering from Closed Surfaces using a Combined Field Integral Equation," *IEEE Trans. Antennas Propagat.*, vol. 48, no. 7, pp. 1064-1074, 2000.

[3] Y. S. Chung, Y. J. Lee, J. H. So, J. Y. Kim, C. Y. Cheon, B. J. Lee, and T. K. Sarkar, "A Stable

Solution of Time Domain Electric Field Integral Equation using Weighted Laguerre Polynomials," *Microw. Opt. Technol. Lett.*, vol. 49, no. 11, pp. 2789-2793, 2007.

[4] B. H. Jung, Y. S. Chung, and T. K. Sarkar, "Time-Domain EFIE, MFIE, and CFIE Formulations using Laguerre Polynomials as Temporal Basis Functions for the Analysis of Transient Scattering from Arbitrary Shaped Conducting Structures," *Prog. Electromagn. Res.*, vol. 39, pp. 1-45, 2003.

[5] B. H. Jung, Y. Chung, M. Yuan, and T. K. Sarkar, "Analysis of Transient Scattering from Conductors using Laguerre Polynomials as Temporal Basis Functions," *Appl. Comput. Electromagn. Soc. J.*, vol. 19, no. 2, pp. 84-92, 2004.

[6] Q. Q. Wang, C. Yan, Y. F. Shi, D. Z. Ding, and R. S. Chen, "Transient analysis of electromagnetic scattering using marching-on-in-order time-domain integral equation method with curvilinear RWG basis functions," *Appl. Comput. Electromagn. Soc. J.*, vol. 26, no. 5, pp. 429-436, 2011.

[7] Y. S. Chung, T. K. Sarkar, B. H. Jung, M. Salazar-Palma, Z. Ji, S. M. Jang, and K. J. Kim, "Solution of Time Domain Electric Field Integral Equation using the Laguerre Polynomials," *IEEE Trans. Antennas Propag.*, vol. 52, no. 9, pp. 2319-2328, 2004.

[8] B. H. Jung, T. K. Sarkar, Y. S. Chung, M. Salazar-Palma, Z. Ji, S. M. Jang, and K. J. Kim, "Transient Electromagnetic Scattering from Dielectric Objects using the Electric Field Integral Equation with Laguerre Polynomials as Temporal Basis Functions," *IEEE Trans. Antennas Propag.*, vol. 52, no. 9, pp. 2329-2340, 2004.

[9] Z. Ji, T. K. Sarkar, B. H. Jung, M. Salazar-Palma, and M. T. Yuan, "A Comparison of Marching-on-in-Time Method with Marching-on-in-Degree for the TD-EFIE Solver," in *Proc. IEEE/ACES Int. Conf. Wireless Communications and Applied Computational Electromagnetics*, Hawaii, 2005, pp. 297-300.

[10] B. Shanker, A. A. Ergin, M. Y. Lu, and E. Michielssen, "Fast Analysis of Transient Electromagnetic Scattering Phenomena using the Multilevel Plane Wave Time Domain Algorithm," *IEEE Trans. Antennas Propag.*, vol. 51, no. 3, pp. 628- 641, 2003.

[11] A. Geranmayeh, W. Ackermann, and T. Weiland, "Space-FFT-Accelerated Marching-on-in-Degree Methods for Finite Periodic Structures," *Int. J. Microw. Wirel. Technol.*, vol. 1, no.4, pp. 331-337, 2009.

[12] Q. Q. Wang, Y. F. Shi, M. M. Li, Z. H. Fan, R. S. Chen, and M. Y. Xia, "Analysis of Transient Electromagnetic Scattering using UV Method Enhanced Time-Domain Integral Equations with Laguerre Polynomials," *Microw. Opt. Technol. Lett.*, vol. 53, no. 1, pp. 158–163, 2011.

[13] M. Bebendorf, "Approximation of Boundary Element Matrices," *Numer. Math.*, vol. 86, no. 4, pp. 565–589, 2000.

[14] K. Z. Zhao, M. N. Vouvakis, and J. F. Lee, "The Adaptive Cross Approximation Algorithm for Accelerated Method of Moments," *IEEE Trans. Electromagn. Compat.*, vol. 47, no. 4, pp. 763-773, 2005.

[15] J. Shaeffer and F. Canning, "Adaptive Cross Approximation for MOM Matrix Fill for PC Problem Sizes to 157000 Unknowns," in Proc. IEEE/ACES *Int. Conf. Wireless Communications and Applied Computational Electromagnetics*, 2005, pp. 748-753.

[16] Z. N. Jiang, R. S. Chen, Z. H. Fan, Y. Y. An, M. M. Zhu, and K. W. Leung, "Modified Adaptive Cross Approximation Algorithm for Analysis of Electromagnetic Problems," *Appl. Comput. Electromagn. Soc. J.*, vol. 26, no. 2, pp. 160-169, 2011.

[17] M. Bebendorf and S. Kunis, "Recompression Techniques for Adaptive Cross Approximation," *J. Integral Equations Appl.*, vol. 21, no. 3, pp. 331-357, 2009.

[18] S. M. Rao, D. R. Wilton, and A. W. Glisson, "Electromagnetic Scattering by Surfaces of Arbitrary Shape," *IEEE Trans. Antennas Propag.*, vol. 30, no. 5, pp. 409-418, 1982.

[19] X. Q. Sheng, J. M. Jin, J. Song, W. C. Chew, and C. C. Lu, "Solution of Combined-Field Integral Equation using Multilevel Fast Multipole Algorithm for Scattering by Homogeneous Bodies," *IEEE Trans. Antennas Propag.*, vol. 46, no.11, pp. 1718-1726, 1998.

[20] M. Chen, R. S. Chen, and X. Q. Hu, "Augmented MLFMM for Analysis of Scattering from PEC Object with Fine Structures," *Appl. Comput. Electromagn. Soc. J.*, vol. 26, no. 5, pp. 418-428, 2011.

[21] Z. N. Jiang, Z. H. Fan, D. Z. Ding, R. S. Chen, and K. W. Leung, "Preconditioned MDA-SVD-MLFMA for Analysis of Multi-Scale Problems," *Appl. Comput. Electromagn. Soc. J.*, vol. 25, no. 11, pp. 914-925, 2010.

[22] A. C. Woo, H. T. G. Wang, M. J. Schuh, and M. L. Sanders, "Benchmark Radar Targets for the Validation of Computational Electromagnetics Programs," *IEEE Antennas Propag. Mag.*, vol. 35, no. 1, pp. 84-89, 1993.

Huan-huan Zhang received the B.S. degree in electronic information engineering from Henan Polytechnic University, Henan, China, in 2009.

He is currently working towards the Ph.D. degree in electromagnetic fields and microwave technology at Nanjing University of Science and Technology. His research interests include transient electromagnetic scattering, time-domain integral equation (TDIE) method and radar target recognition.

Quan-quan Wang received the B.S. degree in communication engineering from Nanjing University of Science and Technology (NUST), China, in 2006.

He is currently working towards the Ph.D. degree in electromagnetic fields and microwave technology at NUST. His research interests include transient EM scattering and TDIE method.

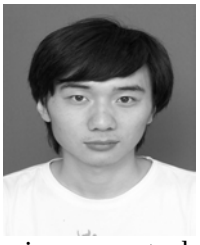

Yi-fei Shi received the B.S. degree in electrical engineering from Nanjing University of Technology, China, in 2004.

He is currently working towards the Ph.D. degree in electromagnetic fields and microwave technology at Nanjing University of Science and Technology, China. His research interests include TDIE and its fast methods.

Ru-shan Chen received the B.S. and M.S. degrees in electronic from Southeast University, China, in 1987 and 1990, respectively, and the Ph.D. degree from the Department of Electronic Engineering, City University of Hong Kong (CUHK), Hong Kong SAR, China, in 2001. In 1990, he joined the Department of Electronic Engineering, Nanjing University of Science and Technology (NUST), China. Since 1996, he has been a Visiting Scholar with the Department of Electronic Engineering, CUHK. In 1999, he was promoted Full Professor of NUST, and in 2007, he was appointed Head of the Department of Communication Engineering.

Optimization of Reception Antenna Composed with Unbalanced Fed Inverted L Element for Digital Terrestrial Television

Daisuke Yagyu [1] and Mitsuo Taguchi [2]

[1] Information Media Center
Nagasaki University, Nagasaki, 852-8521, Japan
d-yagyu@nagasaki-u.ac.jp

[2] Division of Electrical Eng. & Computer Science, Graduate School of Engineering
Nagasaki University, Nagasaki, 852-8521, Japan
mtaguchi@nagasaki-u.ac.jp

Abstract ─ The structure of the array antenna for the reception antenna of the digital terrestrial television broadcasting in Japan is optimized by PSO algorithm. The unbalanced fed ultra low profile inverted L antenna is used as the driven element and two wires are located at the forward and backward directions of the driven element. In the case of antenna size of 170 mm by 325 mm by 29 mm, the return loss bandwidth less than -10 dB is satisfied at the whole broadcasting frequency band (240 MHz) and the directivity of 5.44 dBi to 7.19 dBi is obtained. In the numerical analysis, the electromagnetic simulator WIPL-D based on the method of moment is used.

Index Terms ─ Inverted L antenna, PSO, reception antenna, WIPL-D.

I. INTRODUCTION

The digital terrestrial television broadcasting in Japan started on December 2003, and the analog broadcasting ended on July 2011 except the devastated area by the Great East Japan Earthquake [1]. For the reception of the conventional analog terrestrial broadcasting, directional antennas with high gain, and high front-to-back ratio, such as the Yagi-Uda antenna, are used in order to suppress the ghost image due to the echo. On the other hand, a small antenna with low front-to-back ratio is sufficient for the reception of the digital terrestrial broadcasting. By now, many antennas such as a square loop antenna, a planar antenna, and a W-loop antenna mounted on a car window are proposed for the reception antenna of the terrestrial television broadcasting [2 - 4]. The authors have proposed the planar sleeve antenna composed of a coplanar waveguide for the reception antenna of the digital terrestrial television [5]. Although the good return loss characteristics are obtained at the whole broadcasting frequency band, the directivity becomes low (2.32 dBi to 3 dBi). The high gain antenna is desired for the reception at the far area from the broadcasting station.

The authors have proposed two element phased array dipole antenna [6]. Two half-wave dipoles with 90 degree phase difference feed are located with a distance of less than a quarter wavelength. By controlling the mutual coupling between two dipoles, a front-to-back ratio of 15.3 dB is obtained. Then the authors have proposed an ultra low profile inverted L antenna located on parallel wire conductors [7]. This antenna consists of a coaxial line. The inner conductor of the coaxial line is extended from the end of the outer conductor, that is, this antenna is excited at the end of the outer conductor. The antenna height is around $\lambda/30$ (λ: wavelength). The length of the horizontal element of this antenna is almost a quarter wavelength. In the case of the length of parallel wires is 0.49 λ and three wires are located with the width of 0.124 λ, the maximum gain becomes 3.99 dBi and the return loss bandwidth less than -10 dB is 6.13 %. The authors used an

Submitted On: Aug. 22, 2011
Accepted On: March 2, 2012

ultra low profile inverted L antenna located on parallel conducting wires for the driven element of three element array antenna for the reception antenna of the terrestrial television [8]. In order to widen the return loss bandwidth, the antenna height *h* becomes larger and the distance between horizontal wires *pxp* = *pxm* are shorter compared with those in [7]. Although the directivity of 6.0 dBi to 7.77 dBi is obtained, the return loss bandwidth is satisfied only for 170 MHz of the television frequencies from 470 MHz to 710 MHz.

In this paper, the particle swarm optimization (PSO) algorithm [9, 10] is used for the optimization of the geometry parameters of the antenna proposed in the reference [8] to satisfy the return loss less than -10 dB from 470 MHz to 710 MHz. The genetic algorithm is also used for the optimization of the antenna structure [11-13]. Since there are ten parameters should be optimized and the handling of the real number is easy in the PSO, the PSO algorithm is used for the optimization in this paper. In the numerical analysis, the electromagnetic simulator WIPL-D based on the method of moment is used [14].

II. ANALYTICAL MODEL

Figure 1 shows the structure of the analytical model. The driven element No. 1 is an ultra low profiled inverted L antenna located on three parallel wires. The inverted L antenna is composed of a coaxial radiator. This antenna consists of a horizontal arm in the *y*-direction and a small leg in the *z*-direction. The inner conductor of the coaxial line is extended from the end of an outer conductor, that is, this antenna is excited at the end of an outer conductor. The parallel wires are connected to each other by a single perpendicular wire at the base of the inverted L antenna. The length of horizontal element *L* determines the resonant frequency. The length *L*1 is adjusted for the impedance matching. The radii of outer and inner conductors of the coaxial line are 1.095 mm and 0.255 mm, respectively. The radius of parallel wire *a* is 1.5 mm. The height of the horizontal element is *h*. The wire elements No. 2 and No. 3 are located in the forward and backward directions of antenna. In this paper, the Smith chart and the return loss are normalized by the characteristic impedance 75 Ω of feeder of television receiver.

III. ALGORITHM OF OPTIMIZATION

The PSO algorithm is a population-based stochastic approach for solving continuous and discrete optimization problems [9, 10]. The PSO algorithm and its conditions used, in this paper, are described as follows.

A. Solution space

Solution Space: 10-dimension

Dz: 40 to 120[80],
Dy: 130 to 290[208],
Rz: -120 to -40[-65],
Ry: 300 to 460[320]
h: 15 to 35[24.5],
L: 90 to 170[130],
*L*1: 25 to 65[41]
pxp=*pxm*: 10 to 70[40],
pym: 14 to 74[44],
pyp: 150 to 270[210]

A unit of all parameters is mm. The value in [ ] shows a value shown in the reference [8].

A minimum and maximum value for each dimension in the 10-dimensional optimization is referred to as $Xmin_n$ and $Xmax_n$, respectively, where *n* ranges from 1 to 10.

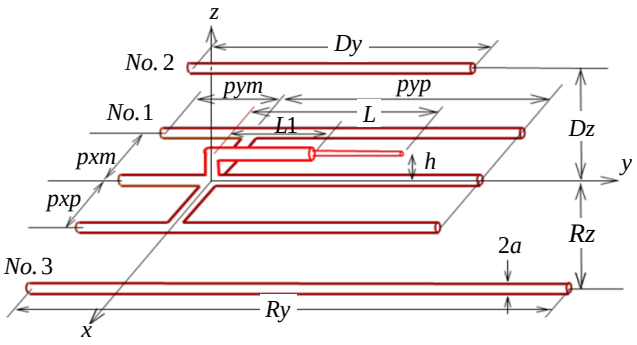

(a) Bird's-eye view

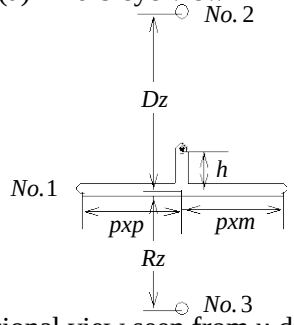

(b) Cross sectional view seen from *y*-direction

Fig. 1. Analytical model of antenna.

B. Fitness function

In this paper, the fitness value is calculated by a bandwidth. The bandwidth is defined as the frequency range where the return loss is less than -10 dB at 75 Ω system. The fitness value is defined by the following equation:

$$fitness\ value = \min\left(F_L, F_H\right) + 0.1\left|F_H - F_L\right|, \quad (1)$$

$$F_L = f_c - f_{lowest}, \quad F_H = f_{highest} - f_c$$

where f_{lowest} and $f_{highest}$ is the lowest and highest frequency of calculated frequency band, respectively. f_c is defined as the center frequency 590 MHz of the frequency band of the digital terrestrial television broadcasting in Japan. If F_L or F_H becomes less than zero, then it is set to be zero. If the calculated frequency band differs from the broadcasting frequency band, F_L differs from F_H. Then, the first term of equation (1) takes smaller value of F_L and F_H. The fitness value is increased in the updating step. Therefore, lower value of F_L and F_H becomes large. This means that the center frequency of the calculation frequency band approaches to f_c in the optimization process. The second term of equation (1) accelerates the extending the return loss bandwidth. In this paper, the coefficient of the second term is fixed as 0.1 based on our experience.

C. Initialization

Each particle begins at its own random location with a velocity that is random both in its direction and magnitude. Initial position in each dimension is given in the following equation:

$$x_n = \mathrm{rand}(\ ) * \left(Xmax_n - Xmin_n\right) + Xmin_n, \quad (2)$$

where x_n is the particle's coordinate in the n-th dimension. The random number function rand( ) returns a number between 0.0 and 1.0.

In this paper, the absolute value of velocities of each particle is limited to 10% of the analytical range in each dimension. $Vmax_n$ shows maximum limit of the absolute value of velocities. $Vmax_n$ is defined as

$$Vmax_n = 0.1 * \left(Xmax_n - Xmin_n\right). \quad (3)$$

The initial velocity defined as

$$v_n = \left\{2 * \mathrm{rand}(\ ) - 1\right\} * Vmax_n, \quad (4)$$

where v_n is the velocity of the particle in the n-th dimension. v_n takes an arbitrary value from $-Vmax_n$ to $Vmax_n$.

D. Iterations

The following procedures are iterated.

1) Evaluate the Particle's Fitness:

The fitness value is computed by the coordinate of each particle. In the numerical analysis of antenna characteristics, the electromagnetic simulator WIPL-D based on the method of moment is used. The coordinate and the velocity of each particle are calculated by the program written in FORTRAN. This program generates an input file of WIPL-D and executes the solver of WIPL-D. In addition, this program demands the return loss from the input impedance value that WIPL-D output. The antenna characteristics and the return loss are calculated at every 5 MHz from 450 MHz to 1 GHz. The larger frequency increment is preferable from the standpoint of the computation time. However, the input impedance characteristics rapidly vary as shown in Figure 4. Therefore, the frequency increment of 5 MHz is chosen.

2) Compare to *pbest*, *gbest*:

pbest is the location in parameter space of the best fitness returned for a specific particle. *gbest* is the location in parameter space of the best fitness returned for the entire swarm. If the fitness value resulting from a change in coordinate of a particle is larger than the fitness value at *pbest* of each particle, *pbest* is changed by that coordinate. In the first iteration, each *pbest* is defined as the initial state of each particle.

If the fitness value resulting from a change in coordinate of each particle is larger than the fitness value at *gbest*, *gbest* is changed by that coordinate. In the first iteration, *gbest* is defined as the coordinate of the particle with best fitness.

3) Update the particle's velocity:

For the next iteration, the velocity of the particle is changed according to the relative locations of *pbest* and *gbest*. It is accelerated in the directions of these locations of greatest fitness according to the following equation:

$$\begin{aligned} v_n = {} & w * v_n + c_1 * \mathrm{rand}(\ ) \times \left(pbest_n - x_n\right) \\ & + c_2 * \mathrm{rand}(\ ) \times \left(gbest_n - x_n\right). \end{aligned} \quad (5)$$

The new velocity is simply the old velocity scaled by *w* and increased in the direction of *gbest* and *pbest* for that particular dimension. c_1 and c_2 are scaling factors. In this paper, w=0.729, c_1=c_2=1.494 [10]. If the absolute value of v_n is greater than $Vmax_n$, v_n is assumed to be $Vmax_n$ or -$Vmax_n$.

4) Move the particle:

For the next iteration, new coordinate x_n is calculated for each dimension according the following equation:

$$x_n = x_n + v_n * \Delta t. \quad (6)$$

In this paper, Δt is assumed to be 1.

5) Boundary conditions:

In this paper, as for the boundary condition to limit the coordinate of each particle in solution space, the absorbing wall is adopted. That is, if new calculated coordinate x_n is less than $Xmin_n$, x_n is replaced as $Xmin_n$. If x_n is greater than $Xmax_n$, x_n is replaced as $Xmax_n$. In either case, v_n is set to zero.

IV. RESULTS AND DISCUSSION

Table 1 shows the comparison of the fitness value for the different number of population. The number of trial is 10. gFIT indicates the best fitness at the number of iteration IX. If the return loss bandwidth is satisfied at the whole broadcasting frequency band (240 MHz), IX indicates the number of iteration when the return loss bandwidth of 240 MHz is obtained at the first time. As the number of population is increased, the good results satisfying the return loss bandwidth are slightly increased. Therefore, from the standpoint of computation time, the number of population is fixed to 50 in the optimization in the subsequent sections.

Based on the above-mentioned algorithm, the antenna parameters with the bandwidth of 240 MHz and more are obtained. The number of unknowns on WIPL-D is 25. The average computation time for the population of 50 and the iteration of 50 is about 6 hours 40 minutes by using PC with AMD Turion™ 64 processor driven at 2 GHz.

Figure 2 shows the example of the convergence of fitness value in the case of population of 50 and the number of maximum iteration is 50. In this trial, the fitness value which satisfies the return loss bandwidth of 240 MHz is obtained at the number of iteration of 25.

Table 1. Fitness value for different number of population

	50		60		70		80	
	IX	gFIT	IX	gFIT	IX	gFIT	IX	gFIT
1	37	115.0	29	116.5	29	111.0	20	120.0
2	38	120.0	37	120.5	47	120.0	30	120.0
3	33	120.0	45	120.0	26	116.0	21	121.0
4	49	105.0	46	116.5	32	120.0	40	115.0
5	23	120.0	44	120.5	49	121.5	22	115.0
6	36	110.0	47	86.0	49	120.5	44	115.0
7	42	110.5	34	105.0	36	116.0	18	120.0
8	45	120.0	29	120.5	42	95.5	11	120.0
9	33	105.5	38	115.0	18	120.0	47	115.5
10	37	66.0	47	115.5	35	116.5	46	116.0

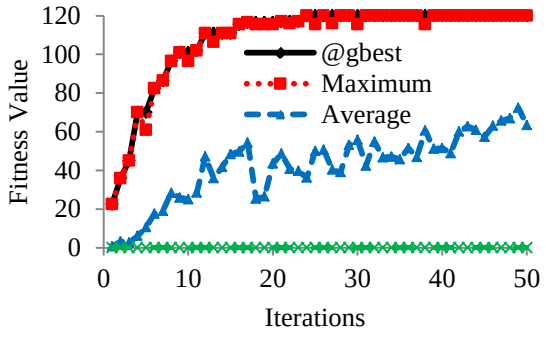

Fig. 2. Convergence of fitness value.

Figure 3 shows the distribution of *Dy* as the function of *Dz*, and *Ry* as the function of *Rz* from the obtained antenna parameters. The distribution of *Ry* can be divided to the following five groups:

Group A: *Rz*<-85, *Ry*<347.5,
Group B: -84<*Rz*<-80, 365<*Ry*<385,
Group C: *Rz*>-79.2, *Ry*<382.5,
Group D: *Rz*<-91.5, *Ry*>385,
Group E: *Rz*>-77.6, *Ry*>400.

In each group, the typical antenna parameters are choosing from the solution in the dense portion in the figure of *Rz* – *Ry*. Figures 4 and 5 show the input impedance and the reflection coefficient characteristics of the antenna of each group, respectively. Figure 6 shows the directivities of antennas of all groups. The

directivity of the antenna in Group A becomes higher at the lower frequencies. The parameters of antenna in Group A are as follows; *Dz* = 74.0 mm, *Dy* = 185.9 mm, *Rz* = -92.7 mm, *Ry* = 325.0 mm, *h* = 30.6 mm, *L* = 121.4 mm, *L1* = 25.9 mm, *pxp* = *pxm* = 12.9 mm, *pym* = 31.6 mm, *pyp* = 214.8 mm. The element No. 3 is located for extending the return loss bandwidth at lower frequencies. The average value of the length of the element No. 3 is 325.5 mm in the Group A, as shown in Figure 3. This length is almost a half wave length at the lowest frequency. Therefore, the directivity of the Group A is improved at lower frequencies.

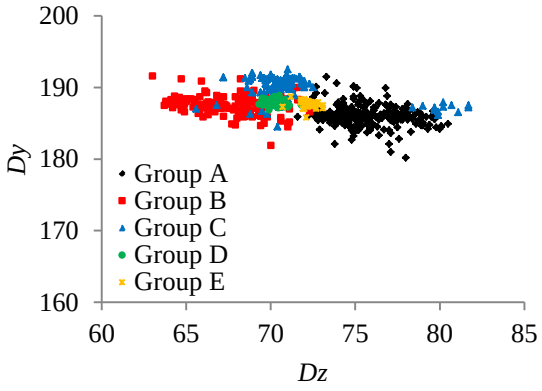

(a) *Dz-Dy*

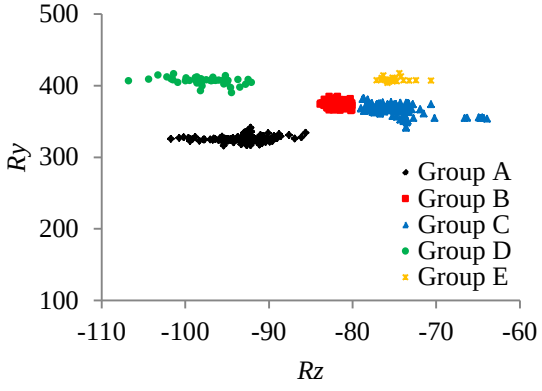

(b) *Rz-Ry*

Fig. 3. Distribution of optimized results.

Figure 7 shows the distribution of *Dy* as the function of *Dz*, and *Ry* as the function of *Rz* in Group A. Four sample data are shown in these figures. Figures 8 and 9 show the input impedance and reflection coefficient characteristics of four sample antennas, respectively. Figure 9 shows the directivity of these antennas. The directivity of these antennas are almost the same.

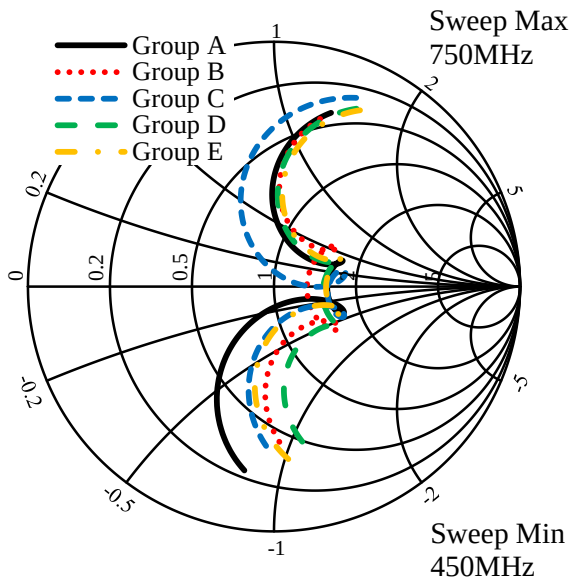

Fig. 4. Input impedance characteristics.

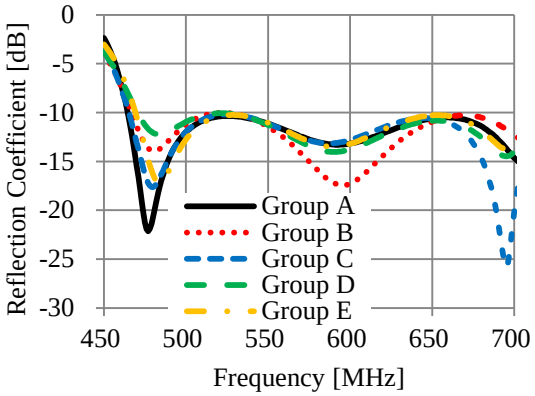

Fig. 5. Reflection Coefficient characteristics.

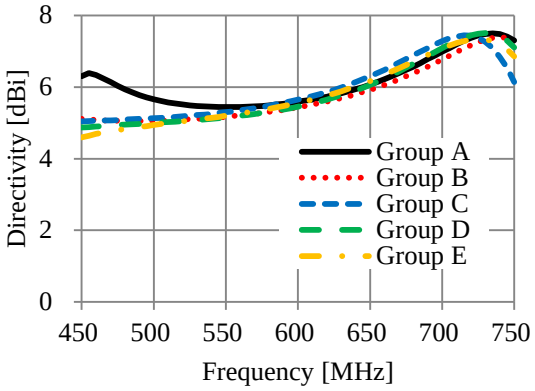

Fig. 6. Directivity characteristics.

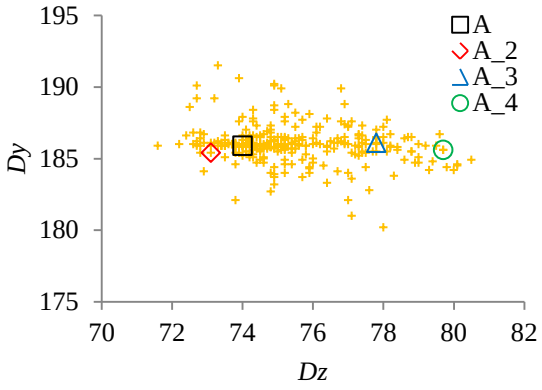

(a) *Dz-Dy*

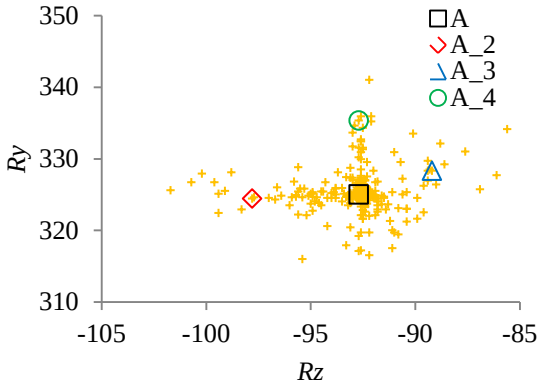

(b) *Rz-Ry*

Fig. 7. Distribution of optimized results.

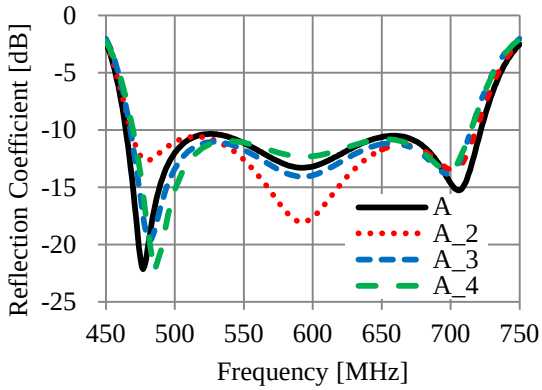

Fig. 8. Reflection Coefficient characteristics.

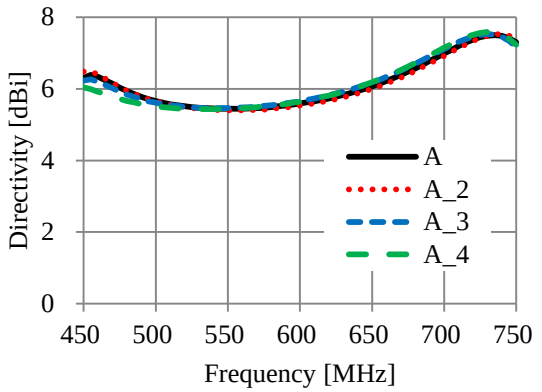

Fig. 9. Directivity characteristics.

Figures 10 and 11 show the electric field radiation patterns of the antenna of Group A in *xz*-plane and *yz*-plane, respectively. Figure 12 shows the comparison of the return loss and the directivity characteristics for the initial design [8] and the optimized solution (Group A).

Figure 13 shows the photograph of fabricated antenna. The inverted L element is fabricated by the semi rigid coaxial cable with the characteristic impedance of 50 Ω. The coaxial cable is extended from the base point of antenna to the backward of parallel wires. The antenna is fixed by the expanded polystyrene. In order to measure the input impedance at the feed point not the return loss, the length of coaxial cable has to be compensated. Since this compensation is not so easy, the return loss is measured by the vector network analyzer with the characteristic impedance of 50 Ω. Figure 14 shows the comparison of measured and calculated reflection coefficient characteristics normalized by 50 Ω.

Since the width of parallel wires (*pxm* + *pxp*) is narrower than the wavelength, the leakage current may flow on the surface of semi rigid cable. This may cause the discrepancy between calculated and measured data at the lower frequencies.

V. CONCLUSION

As the reception antenna of the terrestrial digital television, three element array antenna has been proposed and its structure has been optimized by applying PSO algorithm. The unbalanced fed ultra low profile inverted L antenna on three parallel wires is used as the driven element of proposed antenna. In the case of antenna size of 170 mm by 325 mm by 29 mm, the return loss bandwidth of 240 MHz and the directivity of 5.44 dBi to 7.19 dBi are obtained.

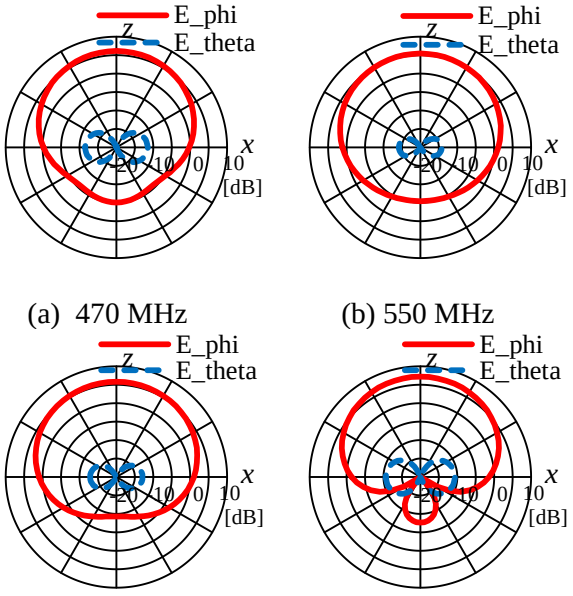

(a) 470 MHz (b) 550 MHz

(c) 630 MHz (d) 710 MHz

Fig. 10. Electric field radiation patterns in *xz*-plane. *Dz* = 74.0 mm, *Dy* = 185.9 mm, *Rz* = -92.7 mm, *Ry* = 325.0 mm, *h* = 30.6 mm, *L* = 121.4 mm, *L1* = 25.9 mm, *pxp* = *pxm* = 12.9 mm, *pym* = 31.6 mm, *pyp* = 214.8 mm.

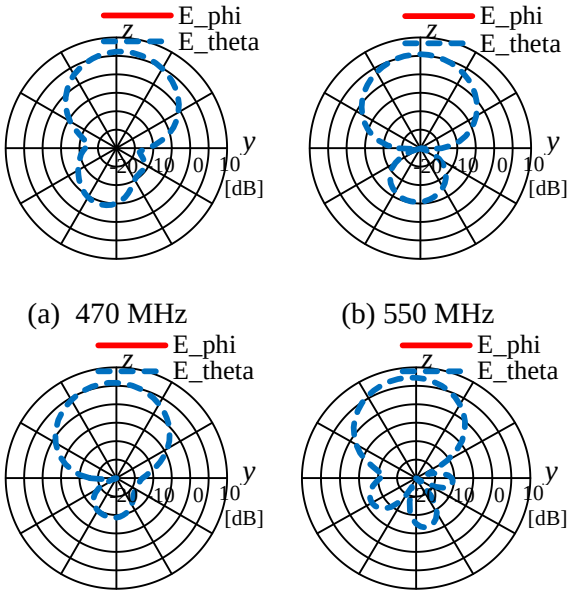

(a) 470 MHz (b) 550 MHz

(c) 630 MHz (d) 710 MHz

Fig. 11. Electric field radiation patterns in *yz*-plane. *Dz* = 74.0 mm, *Dy* = 185.9 mm, *Rz* = -92.7 mm, *Ry* = 325.0 mm, *h* = 30.6 mm, *L* = 121.4 mm, *L1* = 25.9 mm, *pxp* = *pxm* = 12.9 mm, *pym* = 31.6 mm, *pyp* = 214.8 mm.

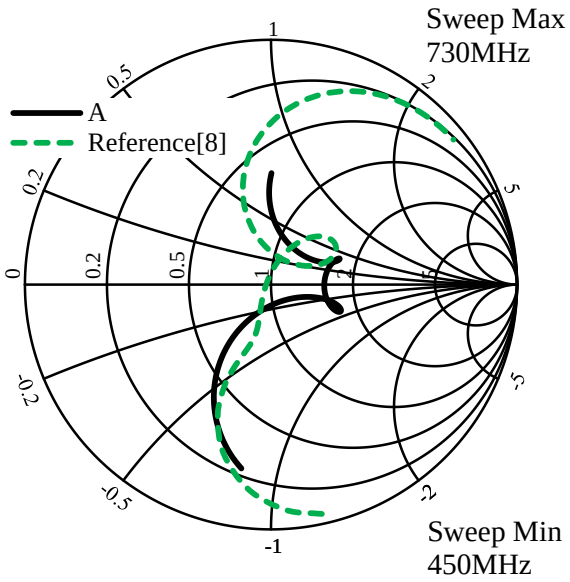

Fig. 12. Comparison of input impedance characteristics for initial design and optimized solution. *Dz* = 74.0 mm, *Dy* = 185.9 mm, *Rz* = -92.7 mm, *Ry* = 325.0 mm, *h* = 30.6 mm, *L* = 121.4 mm, *L1* = 25.9 mm, *pxp* = *pxm* = 12.9 mm, *pym* = 31.6 mm, *pyp* = 214.8 mm.

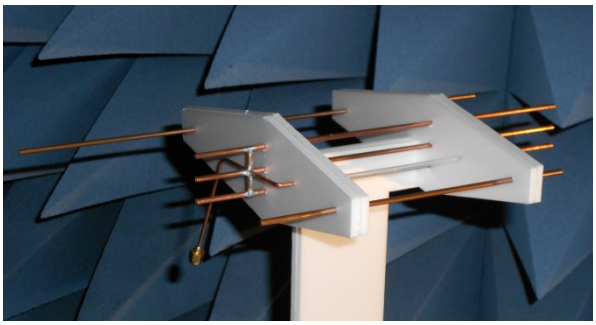

Fig. 13. Photograph of fabricated antenna.

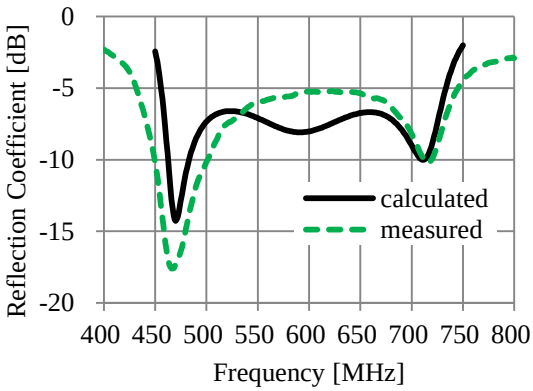

Fig. 14. Reflection Coefficient characteristics normalized by 50 Ω.

REFERENCES

[1] M. Taguchi, "Portable TV Antennas," in *Antenna Engineering Handbook, Fourth Edition*, Chap. 30, New York: McGraw-Hill, 2007.

[2] Y. Okano, "Development of Tabular Broad Band Antenna for UHF-TV," *Trans. ICICE*, vol. J85-B, no. 8, pp. 1426-1433, Aug. 2002. (*in Japanese*)

[3] Y. Okano and K. Sakauchi, "Development of Convenient Planar Broadband Antenna for Terrestrial Digital Broadcasting," *Trans. IEICE*, vol. J90-B, no. 7, pp. 679-688, July 2007. (*in Japanese*)

[4] T. Sato, N. Michishita, Y. Yamada, and K. Ogino, "Measurement of Electrical Characteristics of W-Loop Antenna Mounted on Car for Digital Terrestrial Broadcasting," *Trans. IEICE*, vol. J91-B, no. 9, pp. 1069-1071, Spt. 2008. (*in Japanese*)

[5] Y. Seto and M. Taguchi, "Planar Sleeve Antenna for Reception of Digital Terrestrial Television," *IEICE Technical Report*, no. AP2009-21, May 2009. (*in Japanese*)

[6] M. Taguchi, K. Era, K. Tanaka, "Two Element Phased Array Dipole Antenna," *Applied Computational Electromagnetic Society (ACES) Journal*, vol. 22, no. 1, pp. 112 – 116, March 2007.

[7] M. Taguchi and T. Araki, "Ultra Low Profile Inverted L Antenna on Parallel Wires," *Proc. on 26th Annual Review of Progress in Applied Computational Electromagnetics*, pp. 652-655, April 2010.

[8] M. Taguchi and S. Yang, "Reception Antenna Composed with Unbalanced Fed Inverted L Element for Digital Terrestrial Television in Japan," *Proc. on 2010 Int. Conference on Communications, Circuits and Systems*, #07_M1_03, July 2010.

[9] J. Kennedy and R. C. Eberhart, "Particle Swarm Optimization," *Proc. IEEE Int. Conf. Neural Networks*, vol. IV, pp. 1942-1948, Piscataway, NJ, 1995.

[10] J. Robinson and Y. Rahmat-Samii, "Particle Swarm Optimization in Electromagnetics," *IEEE Trans. Antennas Propag.*, vol. 52, no. 2, pp. 397-407, Feb. 2003.

[11] B. J. Barbisch, D. H. Werner, P. L. Werner, "A Genetic Algorithm Optimization Procedure for the Design of Uniformly Excited and Nonuniformly Spaced Broadband Low Sidelobe Arrays," *Applied Computational Electromagnetic Society (ACES) Journal*, vol. 15, no. 2, pp. 34-42, July 2000.

[12] D. S. Linden, R. MacMillan, "Increasing Genetic Algorithm Efficiency for Wire Antenna Design Using Clustering," *Applied Computational Electromagnetic Society (ACES) Journal*, vol. 15, no. 2, pp. 75-86, July 2000.

[13] C. M. de J. van Coevorden, A. R. Bretones, M. F. Pantoja, S. G. Garcia, A. Monorchio, "A New Implementation of the Hybrid Taguchi GA: Application to the design of a Miniaturized Log-Periodic Thin-Wire Antenna," *Applied Computational Electromagnetic Society (ACES) Journal*, vol. 24, no. 1, pp. 21-31, February 2009.

[14] WIPL-D d.o.o.: http://www.wipl-d.com/, WIPL-D Pro v7.0, 2008.

Daisuke Yagyu Prof. Daisuke Yagyu received his B. E. and M. E. degrees from Nagasaki University, Japan in 1994 and 1996, respectively. From 2000 to 2006, he was a Research Associate at Nagasaki University.

Since 2007, he has been an Assistant Professor at Nagasaki University. His research interests are the antennas for wide band communications and the computer networks. He is a member of the Institute of Electronics, Information and Communication Engineers of Japan.

Mitsuo Taguchi Prof. Mitsuo Taguchi received his B. E. and M. E. degrees from Saga University, Japan in 1975 and 1977, respectively, and a Dr. Eng. Degree from Kyushu University Japan in 1986. From 1977 to 1987, he was a Research Associate at Saga University. From 1987 to 2007, he was an Associate Professor at Nagasaki University.

Since 2007, he has been a Professor at Nagasaki University. In 1996 he was a visiting researcher at the Department of Electrical Engineering at the University of California, Los Angeles. His research interests are the small antenna for mobile communication and UWB antennas. He is a member of ACES, IEEE, the Institute of Electronics, Information and Communication Engineers of Japan and the Institute of Image Information and Television Engineers of Japan.

A Hybrid Finite Element-Boundary Integral-Characteristic Basis Function Method for Scattering by Multiple 3-D Cavities

Zhiwei Cui and Yiping Han

School of Science
Xidian University, Xi'an, 710071, China
zwcui@mail.xidian.edu.cn, yphan@xidian. edu.cn

Abstract ─ An efficient hybrid finite element-boundary integral-characteristic basis function method (FE-BI-CBFM) is proposed to solve the problem of electromagnetic scattering by multiple three-dimensional (3-D) cavities embedded in a conducting plane. Specifically, the finite element method is used to obtain the solution of the vector wave equation inside each cavity and the boundary integral equation is applied on the apertures of all the cavities as a global boundary condition. The resultant coupling system of equations is solved by using an excitation independent characteristic basis function method. Some numerical results are included to illustrate the validity and capability of the proposed method.

Index Terms ─ Boundary integral equation, characteristic basis function method, finite element method, multiple cavities.

I. INTRODUCTION

Electromagnetic scattering from various cavity structures has been intensively investigated by many researchers during the past few decades. Among the many methods applied to this class of problems, the hybrid finite element-boundary integral (FE-BI) method [1–7] has been widely proved to be a general, robust, and accurate numerical method to analyze the EM scattering from open cavities. It employs the finite element method (FEM) to handle the fields in the cavity volume, while the boundary integral equation (BIE) to handle the fields on the aperture of the cavity. This method has been first applied to 2-D scattering problems [1, 2] and later extended to more challenging 3-D scattering problems [3–5]. Recently, Alavikia and Ramahi further extended it to the solution of EM scattering problems involving multiple 2-D cavities [6].

More recently, we presented a domain decomposition of the FE-BI method for solving the problem of EM scattering by multiple 3-D cavities [7]. In the implementation of the method, the vector FEM was applied inside each cavity to derive a linear system of equations associated with unknown fields. The BIE was then applied on the apertures of all the cavities to truncate the computational domain and to connect the matrix subsystem generated from each cavity. By virtue of an iterative domain decomposition method, the coupling system of equations was reduced to a small one which only includes the unknowns on the apertures. The solution to the reduced system was obtained by an iterative solver, where the multilevel fast multipole algorithm (MLFMA) was employed to speed up the matrix-vector multiplication. However, the iterative solver is inefficient when one is interested in solving the reduced system for multiple excitation vectors, as the iterations need to be started anew for each right hand side. In practice, one is often interested in analyzing the monostatic scattering characteristics of the cavities and, in such a case, the resultant FE-BI matrix equation involves a number of excitation vectors. For the purpose of efficient analysis of monostatic scattering characteristics of multiple cavities in a conducting plane, we utilize the characteristic basis function method (CBFM) [8–12] to solve the resultant FE-BI matrix equation. The use of CBFM has the advantages that it only utilizes direct solvers rather than iterative methods; hence it does not suffer from convergence problems and can solve multiple excitation problems efficiently.

Submitted On: Dec. 13, 2011
Accepted On: March 4, 2012

In the following, Section 2 presents the formulation of the hybrid FE-BI-CBFM. Section 3 illustrates some numerical examples and Section 4 is the conclusion.

II. FORMULATION

As illustrated in Fig. 1, let us consider the problem of EM scattering by multiple 3-D cavities embedded in a perfectly conducting plane. For the sake of convenient description, the free space region above the cavities and conducting plane is denoted as Ω_0, the region occupied by the ith cavity is denoted as $\Omega_i \left(i = 1, 2, \cdots, m\right)$, with m being the total number of the cavities, and the corresponding volume and area of the aperture are denoted as V_i and S_i, respectively.

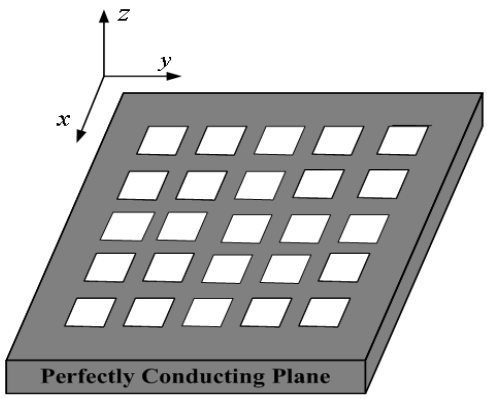

Fig. 1. Geometry of multiple 3-D cavities embedded in a perfectly conducting plane.

The field in region $\Omega_i \left(i = 1, 2, \cdots, m\right)$ can be formulated into an equivalent variational problem with the functional given by [13]

$$F\left(\mathbf{E}_i\right) = \frac{1}{2}\iiint_{V_i}\left[\frac{1}{\mu_{ri}}\left(\nabla\times\mathbf{E}_i\right)\cdot\left(\nabla\times\mathbf{E}_i\right) - k_0^2\varepsilon_{ri}\mathbf{E}_i\cdot\mathbf{E}_i\right]dV + jk_0Z_0\iint_{S_i}\left(\mathbf{E}_i^S\times\mathbf{H}_i^S\right)\cdot\hat{n}_i dS \tag{1}$$

where $\mathbf{E}_i^S$ and $\mathbf{H}_i^S$ denote the electric and magnetic fields on S_i, respectively, and $\hat{n}_i$ denotes the outward unit vector normal to S_i. Using FEM with edge elements, the functional can be converted into a sparse matrix equation

$$\begin{bmatrix} K_i^{II} & K_i^{IS} & 0 \\ K_i^{SI} & K_i^{SS} & B_i \end{bmatrix}\begin{Bmatrix} E_i^I \\ E_i^S \\ H_i^S \end{Bmatrix} = \begin{Bmatrix} 0 \\ 0 \end{Bmatrix} \tag{2}$$

where $\left\{E_i^I\right\}$ is a vector containing the discrete electric fields inside V_i, $\left\{E_i^S\right\}$ and $\left\{H_i^S\right\}$ are the vectors containing the discrete electric and magnetic fields on S_i, respectively. Also, $\left[K_i^{II}\right]$, $\left[K_i^{IS}\right]$, $\left[K_i^{SI}\right]$ and $\left[K_i^{SS}\right]$ are contributed by the volume integral in (1), whereas $\left[B_i\right]$ is contributed by the surface integral.

Since Eq. (2) is independent of the excitation, we can eliminate the interior unknowns to derive a matrix equation that only includes the unknowns on S_i, as follows

$$\left[S_i\right]\left\{E_i^S\right\} + \left[B_i\right]\left\{H_i^S\right\} = \left\{0\right\} \tag{3}$$

where

$$\left[S_i\right] = \left[K_i^{SS}\right] - \left[K_i^{SI}\right]\left[K_i^{II}\right]^{-1}\left[K_i^{IS}\right] \tag{4}$$

Before further proceeding, it should be noted that the above computation in each cavity is independent. Moreover, when the cavities are uniform, this computation can be significantly reduced. Since for this case, the coefficient matrices are the same for each cavity, only one cavity needs to be dealt with.

For all the cavities, we can write the global linear system as follows

$$\begin{bmatrix} S_1 & & & \\ & S_2 & & \\ & & \ddots & \\ & & & S_m \end{bmatrix}\begin{Bmatrix} E_1^S \\ E_2^S \\ \vdots \\ E_m^S \end{Bmatrix} + \begin{bmatrix} B_1 & & & \\ & B_2 & & \\ & & \ddots & \\ & & & B_m \end{bmatrix}\begin{Bmatrix} H_1^S \\ H_2^S \\ \vdots \\ H_m^S \end{Bmatrix} = \begin{Bmatrix} 0 \\ 0 \\ \vdots \\ 0 \end{Bmatrix} \tag{5}$$

By invoking Huygens's principle and image theory, the magnetic field in region Ω_0 can be represented as

$$\mathbf{H_0} = \mathbf{H}^{inc} + \mathbf{H}^{ref} + \sum_{i=1}^{m}\mathbf{H}_i^{sca} \tag{6}$$

where $\mathbf{H}^{inc}$ is the incident field, $\mathbf{H}^{ref}$ is the reflected field from the conducting plane and $\mathbf{H}_i^{sca}$ is the scattered field caused by the equivalent magnetic current $\mathbf{M}_i = \mathbf{E}_i^S \times \hat{n}_i$ on S_i. Also, $\mathbf{H}_i^{sca}$ is defined by [3]

$$\mathbf{H}_i^{sca}(\mathbf{r}) = -2jk_0 \frac{1}{Z_0} \iint_{S_a} \mathbf{M}_i(\mathbf{r}') \cdot \overline{\overline{G}}_0(\mathbf{r}, \mathbf{r}') dS' \quad (7)$$

Since the tangential magnetic field must be continuous across the apertures of all the cavities, we may enforce the boundary condition on S_i to obtain the following BIE

$$\hat{n}_i \times \mathbf{H}_i^S = 2\hat{n}_i \times \mathbf{H}^{inc} + \sum_{i=1}^{m} \left(\hat{n}_i \times \mathbf{H}_i^{sca} \right) \quad (8)$$

Multiplying Eq. (8) by $jk_0 Z_0$ and discretizing the resulting BIE via Galerkin's method yields

$$\begin{bmatrix} P_{11} & P_{12} & \cdots & P_{1m} \\ P_{21} & P_{22} & \cdots & P_{2m} \\ \vdots & \vdots & \ddots & \vdots \\ P_{m1} & P_{m2} & \cdots & P_{mm} \end{bmatrix} \begin{Bmatrix} E_1^S \\ E_2^S \\ \vdots \\ E_m^S \end{Bmatrix} - \begin{bmatrix} B_1 & & & \\ & B_2 & & \\ & & \ddots & \\ & & & B_m \end{bmatrix} \begin{Bmatrix} H_1^S \\ H_2^S \\ \vdots \\ H_m^S \end{Bmatrix} = \begin{Bmatrix} b_1 \\ b_2 \\ \vdots \\ b_m \end{Bmatrix} \quad (9)$$

where $\left[P_{ij}\right], \left[B_i\right]$ and $\left\{b_i\right\} (i, j = 1, 2, \cdots, m)$ are the resultant impedance matrices and excitation vectors due to the discretization of BIE. Combining (5) and (9), we obtain

$$\begin{bmatrix} P_{11}+S_1 & P_{12} & \cdots & P_{1m} \\ P_{21} & P_{22}+S_2 & \cdots & P_{2m} \\ \vdots & \vdots & \ddots & \vdots \\ P_{m1} & P_{m2} & \cdots & P_{mm}+S_m \end{bmatrix} \begin{Bmatrix} E_1^S \\ E_2^S \\ \vdots \\ E_m^S \end{Bmatrix} = \begin{Bmatrix} b_1 \\ b_2 \\ \vdots \\ b_m \end{Bmatrix} \quad (10)$$

For the sake of convenient description, (10) is written in a more compact form as

$$\begin{bmatrix} \mathbf{Z}_{11} & \mathbf{Z}_{12} & \cdots & \mathbf{Z}_{1m} \\ \mathbf{Z}_{21} & \mathbf{Z}_{22} & \cdots & \mathbf{Z}_{2m} \\ \vdots & \vdots & \ddots & \vdots \\ \mathbf{Z}_{m1} & \mathbf{Z}_{m2} & \cdots & \mathbf{Z}_{mm} \end{bmatrix} \begin{bmatrix} \mathbf{J}_1 \\ \mathbf{J}_2 \\ \vdots \\ \mathbf{J}_m \end{bmatrix} = \begin{bmatrix} \mathbf{V}_1 \\ \mathbf{V}_2 \\ \vdots \\ \mathbf{V}_m \end{bmatrix} \quad (11)$$

The resultant FE-BI matrix equation can be efficiently solved by using an excitation independent CBFM presented in [10]. In accordance with the CBFM, we first characterize each aperture by using the so called primary characteristic basis functions (CBFs) that constructed by illuminating the aperture with plane waves incident from N_{PWS} angles. To be more specific, we construct the CBFs by solving the following matrix equation

$$\mathbf{Z}_{ii} \cdot \mathbf{J}_i^{\text{CBFs}} = \mathbf{V}_i^{\text{PWS}} \quad (12)$$

where $\mathbf{V}_i^{\text{PWS}}$ denotes the N_{PWS} plane wave excitation. Since the dimension of each block-diagonal matrix $\mathbf{Z}_{ii}$ is relatively small, the above equation can be solved by using LU decomposition. This type of factorization is highly desirable because we have to solve Eq. (12) N_{PWS} times, one for each incident plane wave, to compute the complete set of primary basis functions.

Next, we use the singular value decomposition (SVD) to express the set of solutions $\mathbf{J}_i^{\text{CBFs}}$ as

$$\mathbf{J}_i^{\text{CBFs}} = \mathbf{U}\mathbf{D}\mathbf{V}^{\text{T}} \quad (13)$$

and we retain the columns from the left singular value matrix $\mathbf{U}$ whose singular values are above a threshold. For simplicity, we assume that all of the apertures contain the same number K of CBFs after SVD, where K is always smaller than N_{PWS}. For the ith aperture the solution can be written as

$$\mathbf{J}_i = \boldsymbol{\alpha}_i \tilde{\mathbf{J}}_i \quad (14)$$

where $\boldsymbol{\alpha}_i = \left(\alpha_i^1, \alpha_i^2, \cdots, \alpha_i^K\right)^{\text{T}}$ are the unknown expansion coefficients to be determined by solving the reduced matrix equation, and $\tilde{\mathbf{J}}_i$ are the new CBFs after SVD. The elements of the reduced matrix take the form

$$\mathbf{A}_{ij} = \tilde{\mathbf{J}}_i^{\text{T}} \mathbf{Z}_{ij} \tilde{\mathbf{J}}_j \quad (15)$$

Thus, the reduced matrix equation can be represented as

$$\begin{bmatrix} \mathbf{A}_{11} & \mathbf{A}_{12} & \cdots & \mathbf{A}_{1m} \\ \mathbf{A}_{21} & \mathbf{A}_{22} & \cdots & \mathbf{A}_{2m} \\ \vdots & \vdots & \ddots & \vdots \\ \mathbf{A}_{m1} & \mathbf{A}_{m2} & \cdots & \mathbf{A}_{mm} \end{bmatrix} \begin{bmatrix} \boldsymbol{\alpha}_1 \\ \boldsymbol{\alpha}_2 \\ \vdots \\ \boldsymbol{\alpha}_m \end{bmatrix} = \begin{bmatrix} \tilde{\mathbf{J}}_1^{\text{T}} \mathbf{V}_1 \\ \tilde{\mathbf{J}}_2^{\text{T}} \mathbf{V}_2 \\ \vdots \\ \tilde{\mathbf{J}}_m^{\text{T}} \mathbf{V}_m \end{bmatrix} \quad (16)$$

Obviously, the dimension of the reduced matrix is much smaller than that of the original impedance matrix and hence equation (16) can be solved directly.

III. NUMERICAL RESULTS

Based on the formulation described above, we have written a computer program to demonstrate the validity and capability of the proposed method. In this program, tetrahedral elements are used to discretize the solution domain and the density of meshes is 12 parts per wavelength. In what follows, all the computations are performed on a personal computer with 3.0 GHz CPU and 2 GB memory.

To illustrate the validity of the proposed method, we first consider a 2×2 array of cavities embedded in a conducting plane. Each cavity of the array has a square $1.0\lambda\times1.0\lambda$ aperture and is 0.6λ deep, with λ being the operating wavelength. The periodicity of the array is 2.0λ in the x- and y-dimensions. For numerical solution, each cavity is subdivided into 4182 tetrahedral elements. As a result, a total of 17808 FEM unknowns and 1252 BIE unknowns are generated. Figure 2 shows the computed radar cross sections (RCS) as a function of the angle of incidence. For comparison, the result obtained using the method of moments (MOM) is given in the same figure. Good agreements are observed between them.

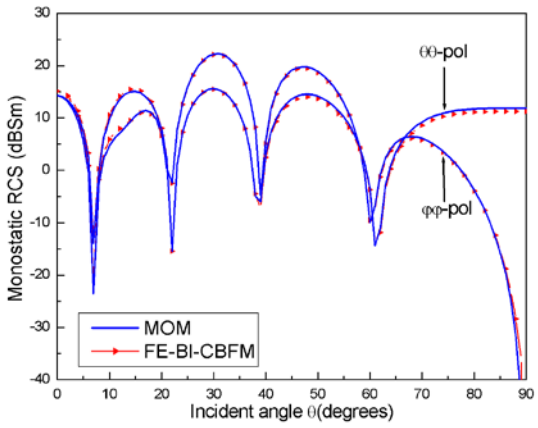

Fig. 2. Comparison of the monostatic RCS for a 2×2 array of cavities from the FE-BI-CBFM and the MOM.

Next, we examine the efficiency of the proposed method. For the problem described above, although the number of FEM unknowns is very large, only one fourth of those need to be dealt with since the cavities are uniform. Utilizing the frontal method to solve the FEM matrix equation, the memory requirement and the computational time are 5 Mb and 15 s, respectively. Furthermore, we only need to analyze a single cavity to construct the CBFs for the entire array. Using the CBFM to solve the resultant FE-BI matrix equation, the memory required is about 6 Mb and the computational time is 25 s. But when we use the iterative method in combination with MLFMA to solve the FE-BI equation, the memory requirement and the computational time are 8 Mb and 310 s, respectively. Thus the proposed FE-BI-DDM is well suitable for the analysis of monostatic scattering characteristics of multiple cavities embedded in a conducting plane.

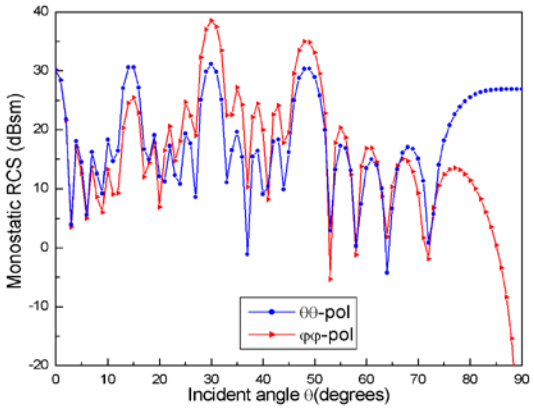

(a)

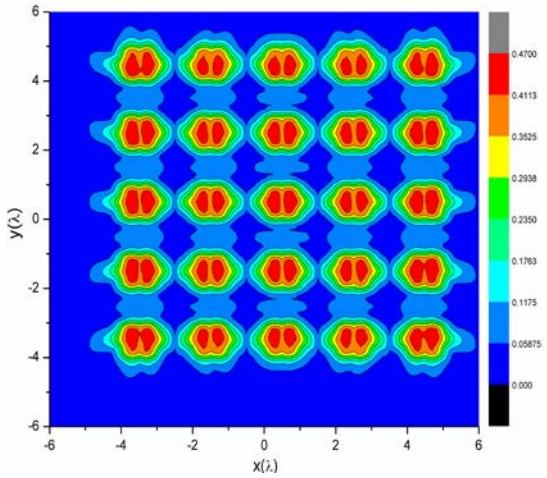

(b)

Fig. 3. RCS and magnitude of electric field calculated for 5×5 array of cavities: (a) monostatic RCS; (b) magnitude of electric field.

Now, we consider the scattering of a plane wave from a 5×5 array of cavities embedded in a conducting plane, as depicted in Fig. 1. The size of each cavity and the periodicity are the same as those of the first example. Figure 3(a) shows the monostatic RCS of the array, while Figure 3(b) shows the magnitude of electric field calculated at a plane located at a distance of $z=0.2\lambda$ above the apertures for the case of normal incidence.

Finally, to demonstrate the capability of the FE-BI-CBFM to handle large scale problems, we consider a 10×10 array of cavities depicted in Fig. 4 (a). The size of each cavity and the periodicity are also taken as $1.0\lambda\times1.0\lambda\times0.6\lambda$ and 2.0λ, respectively. For this example, although the number of the cavities is far more than that of the first example, the memory requirement basically remains the same. The computational time is 2200 s, which can be significantly reduced by adopting the parallel computation because the CBFM is highly parallelizable. The computed RCS is given in Fig. 4 (b) as a function of the angle of incidence.

IV. CONCLUSION

In this paper, the hybrid FE-BI method in combination with the CBFM is proposed to analyze the EM scattering from multiple 3-D cavities in a conducting plane. In the proposed method, each cavity is efficiently modeled by the edge-based FEM. The holes are coupled to each other through the BIE based on the Green's function. To reduce the computational burden, an excitation independent CBFM is used to solve the resultant FE-BI matrix equation. Since the CBFM only utilizes direct solvers rather than iterative methods, it does not suffer from convergence problems and can solve multiple excitation problems efficiently. Numerical results obtained show that the proposed method is suitable for this class of problems.

ACKNOWLEDGMENT

This work was supported by the National Natural Science Foundation of China (Grant No. 60771039).

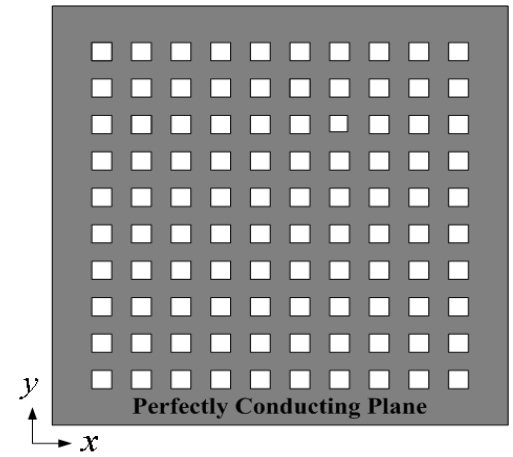

(a)

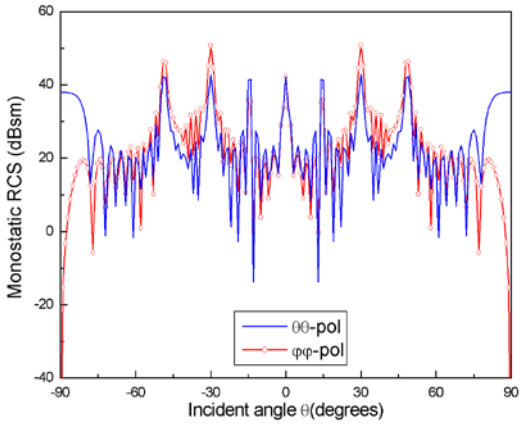

(b)

Fig. 4. A 10×10 array of rectangular cavities: (a) geometrical configuration; (b) monostatic scattering cross section.

REFERENCES

[1] J. M. Jin and J. L. Volakis, "TM Scattering by an Inhomogeneously Filled Aperture in a Thick Conducting Plane," *IEEE Proc. Part H*, vol. 137, no. 3, pp. 153-159, Jun. 1990.

[2] J. M. Jin and J. L. Volakis, "TE Scattering by an Inhomogeneously Filled Aperture in a Thick Conducting Plane," *IEEE Trans. Antennas Propagat.*, vol. 38, no. 8, pp. 1280-1286, Aug. 1990.

[3] J. M. Jin and J. L. Volakis, "A Finite Element-Boundary Integral Formulation for Scattering by Three-Dimensional Cavity-Backed Apertures," *IEEE Trans. Antennas Propagat.*, vol. 39, no. 1, pp. 97-104, Jan. 1991.

[4] J. Liu and J. M. Jin, "A Special Higher Order Finite-Element Method for Scattering by Deep Cavities," *IEEE Trans. Antennas Propagat.*, vol. 48, no. 5, pp. 694-703, May 2000.

[5] J. Meese, L. C. Kempel, and S. W. Schneider, "Mixed Element Formulation for the Finite Element-Boundary Integral Method," *Applied Computational Electromagnetics Society (ACES) Journal*, vol. 21, pp. 51-62, 2006.

[6] B. Alavikia and O. M. Ramahi, "Finite-Element Solution of the Problem of Scattering from Cavities in Metallic Screens using the Surface Integral Equation as a Boundary Constraint," *J. Opt. Soc. Am. A*, vol. 26, no. 9, pp. 1915-1925, Sept. 2009.

[7] Z. W. Cui, Y. P. Han, C. Y. Li and W. J. Zhao, "Efficient Analysis of Scattering from Multiple 3-D Cavities by Means of a FE-BI-DDM Method," *Prog. Electromagn. Res.*, vol. 116, pp. 425-439, 2011.

[8] V. V. S. Prakash and R. Mittra "Characteristic Basis Function Method: A New Technique for Efficient Solution of Method of Moments Matrix Equation," *Microw. Opt. Technol. Lett.*, vol. 36, no. 2, pp. 95-100, Jan. 2003.

[9] G. D. Han and C. Q. Gu, "A Hybrid QR Factorization with Dual-MGS and Adaptively Modified Characteristic Basis Function Method for Electromagnetic Scattering Analysis," *Microw. Opt. Technol. Lett.*, vol. 49, no. 11, pp. 2879-2883, Nov. 2007.

[10] E. Lucente, A. Monorchio, and R. Mittra, "An Iteration-Free MoM Approach Based on Excitation Independent Characteristic Basis Functions for Solving Large Multiscale Electromagnetic Scattering Problems," *IEEE Trans. Antennas Propagat.*, vol. 56, no. 4, pp. 999-1007, Apr. 2008.

[11] C. Delgado, E. Garcia, F. Catedra, and R. Mittra, "Application of the Characteristic Basis Function Method for the Electromagnetic Analysis of Electrically Large and Complex Bodies," *Applied Computational Electromagnetics Society (ACES) Journal*, vol. 24, no. 2, pp. 189-203, Apr. 2009.

[12] R. Mittra, "Characteristic Basis Function Method (CBFM) an Iteration-Free Domain Decomposition Approach in Computational Electromagnetics," *Applied Computational Electromagnetics Society (ACES) Journal*, vol. 24, no. 2, pp. 204-223, Apr. 2009.

[13] J. M. Jin, *The Finite Element Method in Electromagnetics*, Wiley, New York, 2002.

Zhi-Wei Cui was born in Shanxi, China, in 1982. He received the M.Sc. degrees from Xidian University, Xi'an, China, in 2008. He is currently working toward the Ph.D. degree at Xidian University. His research interests include radar cross section analysis, Electromagnetic scattering and propagation in complex media, parallel computation.

Yi-Ping Han was born in Zhejiang, China, in 1964. She received the B.Sc. degree in Department of Physics, Northwest University, in 1984, M. Sc. and Ph.D. degrees in Electrical Engineering Xidian University in 1989, and 2000, respectively. She worked in CNRS (France) for one year, Supporting by the K.C.WONG education foundation in 2001. Since 1989, she has been worked in Department of Physics at Xidian University, China, as lecturer, assistant professor and professor. She is currently director of Physics Department.

Dr. Han is a recipient of the excellent young people awards of MOE，P. R. C. (2003), New Century Excellent Talents awards of MOE，P. R. C. (2004), First-class award for Scientific Technology Award of University in Shanxi (2005), and award of the Excellent PhD Thesis of Shannxi Province (2002) respectively.

She has been in charge of several projects, including National Natural Science Foundation, the Scientific Research Foundation for ROCS, State Key Laboratory Foundation et al. Her main interests are electromagnetic scattering, wave propagation and scattering in atmosphere, electromagnetic compatibility, computational electromagnetics, optical tweezers, laser measuring techniques for particles, optical microcavities.

Investigation of Frequency Effects on the Performance of Single-Sided Linear Induction Motor

Abbas Shiri and Abbas Shoulaie

Department of Electrical Engineering
Iran University of Science and Technology, Tehran, Iran
abbas_shiri@iust.ac.ir, Shoulaie@iust.ac.ir

Abstract ─ Single-sided linear induction motors (SLIMs) have been widely used in industry, especially in high-speed transportation systems. The performance of the SLIMs is considerably affected by the characteristics of its secondary back-iron. The conductivity of the iron used as well as its magnetic permeability influence the performance of the machine, while the magnetic permeability itself is affected by the input frequency of the SLIM. In this paper, using Dancan equivalent circuit model and considering all phenomena involved in the single-sided linear induction motor, the outputs of the motor such as efficiency, power factor, normal force and output thrust are analytically derived. Then, the effects of the input frequency on depth of the field penetration and saturation level of the secondary back-iron as well as the SLIM outputs are analyzed. To confirm the analytical results, 2D time-stepping finite element method is employed. The results are in good agreement with each other confirming the analytical analysis.

Index Terms ─ Back-iron saturation, efficiency, input frequency, normal force, output thrust, power factor.

I. INTRODUCTION

Single-sided linear induction motor (SLIM) is one of the many kinds of linear motors that became popular in industry in recent decades. Their simple structure and comparatively low construction cost make them a reliable candidate for high-speed transportation systems [1, 2]. Because of the importance of the SLIM, it has gained interests of the researchers in industry. Many investigations have been done concerning the design of the SLIMs. In design, the primary weight [3], the thrust and power to weight ratio [4], the power factor and efficiency [5-7], and thrust in constant current [8] have been considered. To study the performance of the SLIMs, several equivalent circuit models have been proposed which facilitate their analysis [9-11]. There are special phenomena in linear motors that make them different from their rotary counterparts. Lee et al. have investigated the effect of the construction of the secondary on edge effect [12]. There are some researches which investigate the end effect in linear induction motors. Bazghaleh et al. have designed the SLIM considering end effect phenomenon [13-15]. In [16], the existence of the end effect has been confirmed by using analytical equations and defining end effect factor. Also, the effects of design parameters on the end effect have been investigated in [17-19].

In double-layer secondary SLIM, the performance of the latter is mainly influenced by saturation level of the back-iron. The secondary back-iron plays important role in operation of the SLIM. Besides providing a mechanical support, it is used as magnetic flux pass produced by the primary. Changing the input frequency changes the saturation level of the back-iron and so, impresses the performance of the motor. In this paper, to study the performance of the SLIM, analytical equations for the efficiency, power factor, normal force and output thrust are derived. All phenomena involved in the single-sided linear induction motor such as longitudinal end effect, back-iron saturation, transverse edge effect, and skin effect are considered in equations. Then, using the derived equations, the frequency effects

Submitted On: Jan. 12, 2012
Accepted On: April 25, 2012

on the saturation level of the back-iron and the motor performance are investigated. To confirm the validity of the analytical analysis, as well as the obtained outputs, finite element method is employed and the results are compared.

II. EQUIVALENT CIRCUIT MODEL OF THE SLIM

Similar to rotary induction motors, the performance of SLIM can be investigated by equivalent circuit model [9-11]. For investigation of the performance of the SLIM, the equivalent circuit model proposed by Duncan is employed [9]. The per-phase equivalent circuit model is shown in Fig. 1. In this figure, R_1 is the per-phase resistance of the primary which is calculated as follows:

$$R_1 = \frac{2(W_s + l_{ec})N}{\sigma_w A_w}, \quad (1)$$

In the above equation, σ_w is the conductivity of the conductor used in the primary winding, l_{ec} is the end connection length, W_s primary width, N the per-phase number of turns of the primary winding and A_w is the cross-sectional area of the conductor.

The primary leakage reactance is given by [20, 21]:

$$X_1 = 2\mu_0\omega_1[(\lambda_s(1+\frac{3}{2p})+\lambda_d)\frac{W_s}{q}+\lambda_e l_{ec}]N^2/p, \quad (2)$$

where μ_0 is the permeability of the vacuum, p the number of pole pairs, q the number of the slots per pole per phase, ω_1 the primary angular frequency and λ_s, λ_e and λ_d are the permeances of slot, the end connection and the differential, respectively.

The per-phase magnetizing reactance of the motor is given by [20]:

$$X_m = \frac{6\mu_0\omega_1 W_{se} {k_w}^2 N^2 \tau}{\pi^2 p g_e}, \quad (3)$$

where k_w is the winding factor, τ the pole pitch and W_{se} and g_e are the equivalent primary width and the effective air-gap length, respectively, which are calculated by the following equations:

$$W_{se} = W_s + g_m, \quad (4)$$

$$g_e = (k_c k_l / k_{tm})(1+k_s)g_m, \quad (5)$$

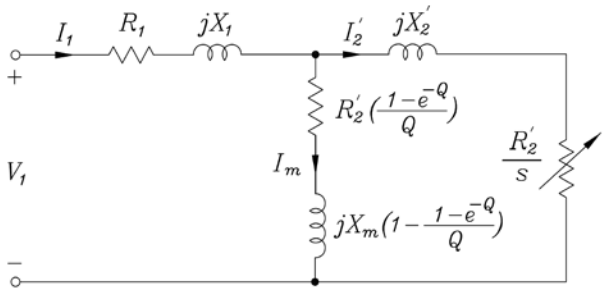

Fig. 1. Equivalent circuit of SLIM.

In the aforementioned equations, the following denotations and equations are hold:

g_m is the magnetic air-gap, k_l the air-gap leakage factor, k_c the Carter's coefficient, k_{tm} the magnetizing reactance factor due to edge effect, and k_s is the secondary iron saturation factor. The mentioned coefficients are given as follows:

$$g_m = g + d, \quad (6)$$

$$k_l = \frac{\sinh(\pi g_m/\tau)}{\pi g_m/\tau}, \quad (7)$$

$$k_c = \frac{\tau_s}{\tau_s - \gamma g_m}, \quad (8)$$

$$\gamma = (w_s/g_m)^2/[5+(w_s/g_m)], \quad (9)$$

$$k_{tm} = (k_R/k_x)k_{tr}, \quad (10)$$

$$k_{tr} = \frac{{k_x}^2}{k_R}\frac{1+(sGk_R/k_x)^2}{1+(sG)^2}, \quad (11)$$

$$k_R = 1 - \mathrm{Re}[(1-jsG)\frac{2\lambda}{\alpha W_{se}}\tanh(\frac{\alpha W_{se}}{2})], \quad (12)$$

$$k_x = 1 + \mathrm{Re}[(sG+j)\frac{2sG\lambda}{\alpha W_{se}}\tanh(\frac{\alpha W_{se}}{2})], \quad (13)$$

$$\lambda = \frac{1}{1+\sqrt{1+jsG}\tanh(\frac{\alpha W_{se}}{2})\tanh[\pi(c-\frac{W_{se}}{2})/\tau]}, \quad (14)$$

$$\alpha = (\pi/\tau)\sqrt{1+jsG}, \quad (15)$$

$$G = \frac{2\mu_0 f_1 \tau^2 \sigma_e d}{\pi g_m k_l k_c (1+k_s)}, \quad (16)$$

$$k_s = \mu_0(\tau/\pi)^2(\mu_i\delta_i g_m k_c)^{-1}, \quad (17)$$

$$\delta_i = \mathrm{Re}[\frac{1}{\sqrt{(\pi/\tau)^2 + j2\pi f_1 \mu_i s\sigma_i/k_{tri}}}], \quad (18)$$

$$k_{tri} = [1-(\frac{2\tau}{\pi W_{se}})\tanh(\frac{\pi W_{se}}{2\tau})]^{-1}, \quad (19)$$

In the above equations, g is the physical air-gap, d is the secondary aluminum sheet thickness, s the motor slip, G goodness factor of the motor, δ_i the depth of the field penetration in the secondary back-iron, and μ_i is the secondary back-iron permeability which should be calculated using iterative algorithm [22].

For the calculation of the secondary resistance, the conductivity of the secondary sheet should be modified. The effective conductivity of the secondary sheet, σ_e is given by [20]:

$$\sigma_e = \sigma / k_{sk}, \tag{20}$$

in which

$$k_{sk} = \frac{2d}{\delta_s}[\frac{\sinh(2d/\delta_s)+\sin(2d/\delta_s)}{\cosh(2d/\delta_s)-\cos(2d/\delta_s)}], \tag{21}$$

where δ_s is the depth of the field penetration in the secondary sheet which can be calculated by:

$$\delta_s = [\frac{1}{2}(\frac{\pi}{\tau})^2 + \mu_0 \pi f_1 s \sigma]^{-1/2}, \tag{22}$$

In the above equation, f_1 is the primary supply frequency, τ the motor pole pitch, σ is the conductivity of the secondary sheet which is reduced by the factor k_{sk} because of the skin effect. Besides the skin effect, the edge effect reduces the secondary conductivity by the factor k_{tr}. If the latter factor and contribution of the secondary back-iron in conduction of the secondary current are taken into account, the effective conductivity is modified to:

$$\sigma_{ei} = \frac{\sigma}{k_{sk} k_{tr}} + \frac{\sigma_i \delta_i}{k_{tri} d}. \tag{23}$$

The primary referred secondary resistance is defined as [23]:

$$R_2' = X_m / G_e, \tag{24}$$

where G_e is the modified goodness factor of the motor which is given by [20]:

$$G_e = 2\mu_0 f_1 \tau^2 \sigma_{ei} d / (\pi g_e). \tag{25}$$

In secondary sheet linear induction motors, the secondary reactance can be neglected [24]; so, $X_2' \approx 0$. Also, due to low value of the flux density in the air-gap, the core loss is negligible; so, $R_c \approx 0$. In Fig. 1, Q is normalized motor length. The value of Q is obtained by the following equation [9]:

$$Q = L_s R_2' / [(L_m + L_2')V_r], \tag{26}$$

In which, L_s is the primary length, V_r the motor speed, L_m the magnetizing inductance, and L_2' is the secondary leakage inductance which is zero for secondary sheet motors.

Air-gap flux density is given by [20]:

$$B_g = \mu_0 J_m \tau / [\pi g_e \sqrt{1+(sG_e)^2}], \tag{27}$$

where, J_m is the amplitude of the equivalent current sheet which is calculated as follows [20], [25]:

$$J_m = 3\sqrt{2} k_w N I_1 / (\pi \tau). \tag{28}$$

Using (27), the tooth flux density is obtained as:

$$B_t = B_g \tau_s / w_t. \tag{29}$$

Referring to Fig. 1 and doing some mathematical calculations, the following equations for efficiency, power factor, output thrust and normal force are derived:

$$\eta = \frac{F_x 2\tau f_1 (1-s) + 3(s-1) R_m {I_m}^2}{F_x 2\tau f_1 + 3{I_1}^2 R_1}, \tag{30}$$

$$\cos\varphi = [F_x 2\tau f_1 + 3{I_1}^2 R_1] / (3 I_1 V_1), \tag{31}$$

$$F_{xo} = \frac{3{I_1}^2 R_2'}{s 2\tau f_1}[\frac{{R_m}^2 + {X_{m1}}^2}{(R_2'/s + R_m)^2 + {X_{m1}}^2}], \tag{32}$$

$$F_y = \frac{\mu_0 L_s W_s}{4} \frac{1-(\sigma_{ei} d \mu_0 s V_s)^2}{\sinh^2(\pi g_{ei}/\tau) + (\sigma_{ei} d \mu_0 s V_s)^2 \cosh^2(\pi g_{ei}/\tau)} {J_m}^2, \tag{33}$$

In the above equations, R_m is the magnetizing branch resistance in Duncan model which represents the power loss due to end effect and X_{m1} is the modified magnetizing reactance considering end effect which are calculated by the following equations:

$$R_m = R_2'[1-e^{-Q}]/Q, \tag{34}$$

$$X_{m1} = X_m(1-[1-e^{-Q}]/Q), \tag{35}$$

III. SECONDARY BACK IRON SATURATION EFFECTS

The secondary back-iron plays important role in performance of the SLIM. On the one hand, it is used as magnetic flux pass produced by the primary; on the other hand, it is a mechanical support for the secondary of the motor. For proper working of the SLIM, the magnetic field produced by the primary should penetrate in the secondary aluminum sheet as well as the secondary back-iron. Because of the low value of the relative

permeability of the secondary conductor sheet, the field can easily penetrate in whole of it. However, the depth of the field penetration in the secondary back-iron is limited. The field can only penetrate in a limited thickness of the iron. Hence, the whole thickness of the secondary back-iron is not used as magnetic flux pass. Thus, at some operating conditions, due to high value of the flux density, saturation occurs in the back-iron and should be taken in to account in calculations. The saturation factor is given in (17) where the iron relative permeability μ_i should be determined. To do this, an iterative algorithm is employed. First, a proper value for the relative permeability μ_i is assigned. Then, the saturation factor and the depth of the field penetration are calculated using (17) and (18). Then, air-gap leakage factor k_l, Carter's coefficient k_c, magnetizing reactance factor due to edge effect k_{tm} are calculated using (7), (8), and (10). Then, the effective air-gap length and the secondary modified effective conductivity are calculated using (5) and (23). The air-gap flux density is calculated using (27). If the distribution of the flux density through the back-iron takes exponential form, in depth x from the surface of the back-iron, we have:

$$B_i = B_{is} e^{-\frac{x}{\delta_i}} \tag{36}$$

where B_{is} is the flux density on the secondary back-iron surface. By having air-gap flux density, B_{is} is calculated using the following equation:

$$B_{is} = B_g \frac{\tau}{\pi \delta_i} \tag{37}$$

With the obtained flux density, and using the back-iron $B-H$ curve, the relative permeability of the back-iron is calculated. Now, the relative permeability used in the previous calculation step is replaced by the calculated one. With the new obtained relative permeability, the calculations are repeated to obtain a desired convergence.

IV. PERFORMANCE ANALYSIS AND DISCUSION

In this section, the effect of the input frequency on the performance of the SLIM is investigated. The specifications of the SLIM are shown in Table 1. As mentioned in the previous sections, the frequency influences the depth of the field penetration and saturation level of the secondary back-iron. In Fig. 2, the depth of the field penetration in back-iron, its relative permeability, the input impedance and the input current of the SLIM are illustrated. It is seen in this figure that by increasing the frequency, the depth of the field penetration is decreased while the relative permeability of the secondary back-iron is increased. At first, it seemed that by decreasing the depth of penetration, the relative permeability would decrease because of increasing the flux density in limited thickness of the iron. However, the increment in the relative permeability is because of the increasing the input impedance and accordingly decreasing the input current and the air-gap flux density, as the frequency increased. In order to approximately maintain the input current and the air-gap flux density constant, the input voltage is increased by increasing the frequency. So, *V/f* is kept constant. In this case, the results for the same characteristics depicted in Fig. 2 are illustrated in Fig. 3. As expected, it is seen that by increasing the input frequency, the relative permeability of the back-iron decreases. The relative permeability in these figures is obtained by iterative algorithm discussed in the previous section. The magnetizing curve for the sample iron used as back-iron is illustrated in Fig. 4 which has been extracted by experiment. Figure 5 shows outputs of the SLIM versus input frequency. It is seen that increasing the frequency, on the one hand, increases the efficiency; on the other hand, decreases the power factor, the output thrust and the normal force. As the input impedance increases by increasing the frequency, the input current and accordingly the air-gap flux density decreases and causes the output thrust and also the normal force to decrease. As seen in the figure, the normal force becomes negative for the frequencies higher than 262Hz. It means that in mentioned frequency ranges, the repulsive normal force is larger than the attractive one. This phenomenon is because of the reaction of the secondary conductor sheet. For further clarity, the attractive and repulsive normal forces are separately shown in Fig. 6. As it is seen in this figure, although the absolute values of both of the attractive and repulsive normal force decrease by increasing the frequency, the absolute value of the repulsive force is larger than that of attractive one in high frequency ranges. Figure 7 illustrates the depth of

the field penetration and relative permeability of the secondary back-iron versus frequency in different back-iron resistivities. The figure shows that by increasing the back-iron resistivity, the depth of the field penetration is increased as expected from (18). Also, increasing the resisitivity of the back-iron increases the permeability of the iron, and accordingly decreases its reluctance. In Fig. 8, the relative permeability of the back-iron versus the motor speed is illustrated for constant input frequency. As seen in this figure, in low speeds, the frequency in the secondary circuit of the SLIM is high; hence, the value of the relative permeability is low. As the speed increases the relative permeability also increases. It should be noted that in this case, only the frequency of the secondary circuit changes; so, the input impedance of the motor does not change too much to decrease the input current and the air-gap flux density. This is the reason for different behavior of the relative permeability in Figs. 2 and 8.

Table 1: The SLIM specifications

Specification	Values
Phase input voltage, V	220
Primary current density, A/mm^2	6
Primary width, mm	130
Secondary sheet thickness, mm	2.0
Air gap length, mm	5.1
Slip	0.5
Number of pole pairs	2
Number of slots/pole/phase	3
Number of turns/phase	72
Motor length(L_s), m	0.4138
Tooth width, mm	2.9
Slot width, mm	6.8
Slot depth, mm	39.3
Primary weight, Kg	29.34

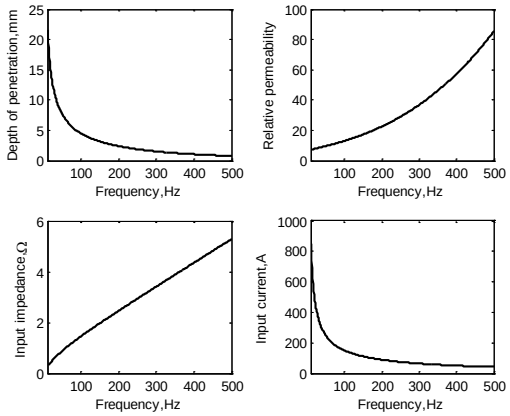

Fig. 2. Frequency effects on different parameters of the SLIM.

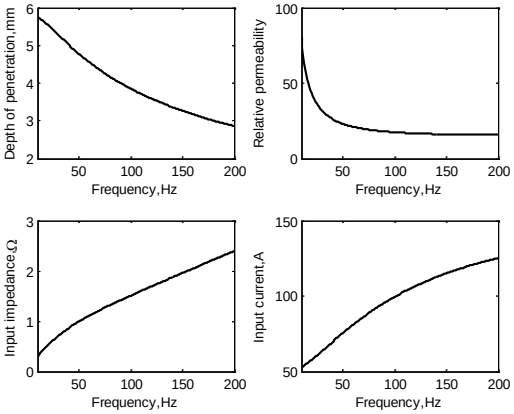

Fig. 3. Frequency effects on different parameters of the SLIM (*V/f* constant).

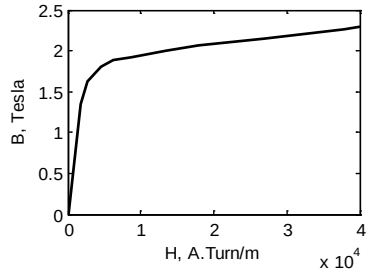

Fig. 4. Back-iron magnetizing curve extracted by experiment.

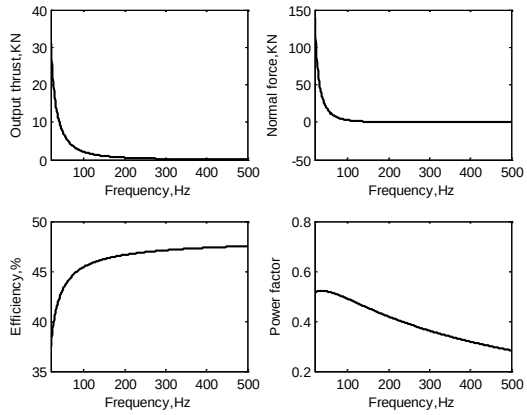

Fig. 5. Frequency effects on different outputs of the SLIM.

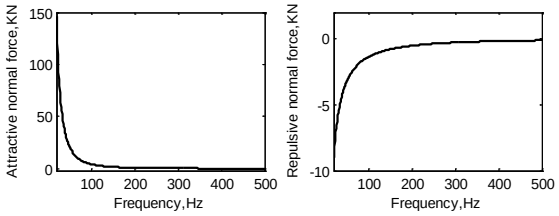

Fig. 6. Frequency effects on attractive and repulsive normal force.

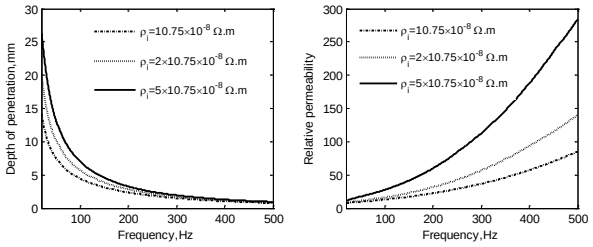

Fig. 7. Frequency effects on different parameters of the SLIM.

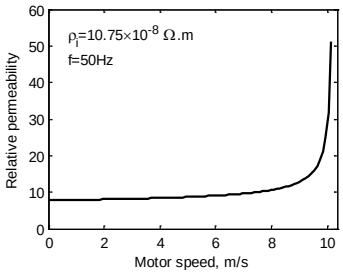

Fig. 8. Relative permeability of the back-iron versus motor speed.

V. FINITE ELEMENT ANALYSIS

In this section, 2-D time-stepping finite element method (FEM) is employed to confirm the analytical results. The SLIM given in Table 1 is used in FEM simulations. In Fig. 9, the flux paths in the different parts of the SLIM is illustrated. The input frequency of the motor is 20Hz. In order to investigate the effect of the frequency on the depth of the field penetration and the secondary back-iron, the simulations are done with input frequency of 20 and 200Hz in constant input current. With input current being constant, only the effects of the input frequency changes are investigated. Figure 10 shows the flux density distribution results for f=20Hz, while in Fig. 11, the flux density distribution results for f=200Hz are illustrated. The magnetizing curve shown in Fig. 4 is used for the back-iron. As seen in Figs. 10 and 11, by increasing the input frequency, the depth of the field penetration is reduced and the flux can only penetrate into a limited thickness of the secondary back-iron. Also, the flux density is increased in those regions. Figure 12 illustrates the distribution of the current density on the secondary back-iron, when the input frequency is 200 Hz. It is also clear in this figure that the depth of the field penetration is limited to a narrow path in the secondary back-iron. The current density in these areas is in the order of $10^7 A/m^2$. This high value of current density produces large local MMFs and causes the flux density to increase and locally saturates the secondary back-iron. To compare the analytical results with the results of the FEM, the simulations have been done in different input frequencies. The efficiency, the power factor, the normal force, and the output thrust are calculated using the FEM. The analytical calculation results are compared with FEM results in Table 2. It is seen in Table 2 that by increasing the input frequency, the efficiency increases while the power factor, the normal force, and the output thrust decrease. These behaviors have been previously deduced from Fig. 5. It can be also seen that the results of the two methods are close enough to each other confirming the analytical calculations.

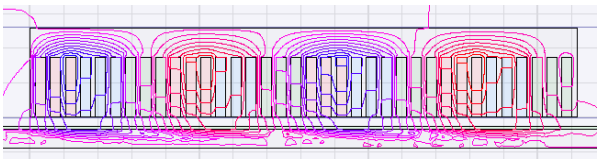

Fig. 9. Flux paths in the moving SLIM ($f = 20Hz$).

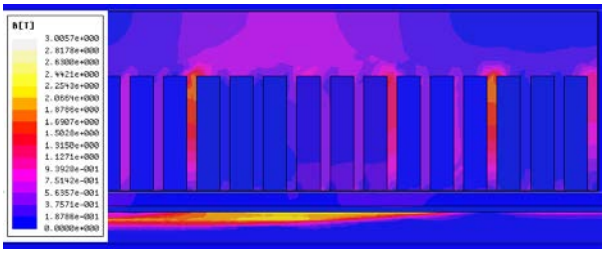

Fig. 10. Flux density distribution in different parts of SLIM ($f = 20Hz$).

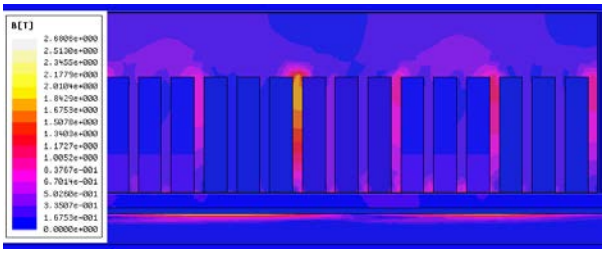

Fig. 11. Flux density distribution in different parts of SLIM ($f = 200Hz$).

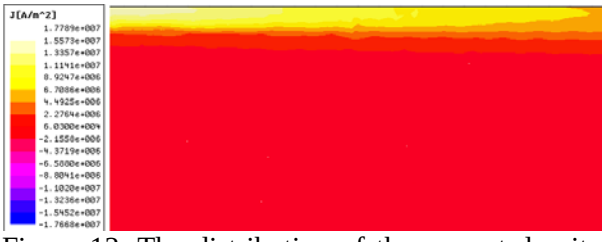

Figure 12. The distribution of the current density on the secondary back-iron ($f = 200Hz$).

VI. CONCLUSION

The magnetic characteristic of the secondary back-iron in the SLIM is affected by the level of the saturation and accordingly the input frequency. So, the performance of the motor mainly depends on the latter. In this paper, the effects of the input frequency on the SLIM outputs are investigated. Analytical equations for the efficiency, the power factor, the normal force and the output thrust of the SLIM are derived considering the longitudinal end effect, iron saturation, transverse edge effect, and skin effect. The results show that increasing the frequency, decreases the active and usable thickness of the secondary back-iron. So, in high frequencies, the thickness of the secondary back-iron can be limited to the depth of the field penetration in the iron. It should be mentioned that besides the magnetic capabilities, the secondary back-iron is used as mechanical support for the secondary sheet which should be taken in to account in design. 2D finite element method is used to confirm the analytical investigations. The FEM results, in which all phenomena are taken into account, are in good agreement with the analytical results. This confirms the validity of the proposed analytical equations and analysis.

Table 2: The calculation and FEM results

		Efficiency, %	Power factor
f=20Hz	Analytical	37.59	0.5252
	FEM	35.71	0.5447
f=50Hz	Analytical	43.20	0.5211
	FEM	41.42	0.5409
f=100Hz	Analytical	45.38	0.4898
	FEM	44.04	0.5093
f=500Hz	Analytical	47.52	0.2824
	FEM	45.97	0.3101
		Normal force, KN	Output thrust, KN
f=20Hz	Analytical	137.18	32.01
	FEM	136.21	32.05
f=50Hz	Analytical	17.91	7.32
	FEM	18.01	7.35
f=100Hz	Analytical	2.89	2.18
	FEM	2.81	2.20
f=500Hz	Analytical	-0.069	0.073
	FEM	-0.060	0.069

REFERENCES

[1] S. Nonaka and T. Higuchi, “Elements of Linear Induction Motor Design for Urban Transit”, *IEEE Trans. Magn.*, vol. 23, no. 5, pp. 3002-3004 , 1989.

[2] S. Yoon, J. Hur, and D. Hyun, “A Method of Optimal Design of Single-Sided Linear Induction Motor for Transit”, *IEEE Trans. Magn.*, vol. 33, no. 5, pp. 4215-4217, 1997.

[3] S. Osawa, M. Wada, M. Karita, D. Ebihara, and T. Yokoi, “Light-Weight Type Linear Induction Motor and Its Characteristics”, *IEEE Trans. Magn.*, vol. 28, no. 4, pp. 3003-3005, 1992.

[4] M. Kitamura, N. Hino, H. Nihei, and M. Ito, “A Direct Search Shape Optimization Based on Complex Expressions of 2-Dimentional Magnetic Fields and Forces”, *IEEE Trans. Magn.*, vol. 34, no. 5, pp. 2845-2848, 1998.

[5] A. H. Isfahani, H. Lesani, and B. M. Ebrahimi, “Design Optimization of Linear Induction Motor

for Improved Efficiency and Power Factor", *IEEE Int. Conf. on Electric Machines Drives, IEMDC*, pp. 988-991, 2007.

[6] A. H. Isfahani, B. M. Ebrahimi, and H. Lesani, "Design Optimization of a Low-Speed Single-Sided Linear Induction Motor for Improved Efficiency and Power Factor", *IEEE Trans. Magn.*, vol. 44, no. 2, pp. 266-272, 2008.

[7] C. Lucas, Z. Nasiri, G. and F. Tootoonchian, "Application of an Imperialist Competitive Algorithm to Design of Linear Induction Motor", *Energy Conversion and Management*, vol. 51, pp. 1407-1411, 2010.

[8] D. H. Im, S. C. Park, and J. W. Im, "Design of Single-Sided Linear Induction Motor using the Finite Element Method and SUMT", *IEEE Trans. Magn.*, vol. 29, no. 2, pp. 1762-1766, 1993.

[9] J. Duncan, "Linear Induction Motor-Equivalent Circuit Model", *IEE Proc. Electric Power Appl.*, vol. 130, no. 1, pp. 51-57, 1983.

[10] W. Xu, J. G. Zhu, Y. Zhang, Y. Li, Y. Wang, and Y. Guo, "An Improved Equivalent Circuit Model of a Single-Sided Linear Induction Motor", *IEEE Trans. Vehicular Tech.*, vol. 59, no. 5, pp. 2277-2289, 2010.

[11] W. Xu, J. G. Zhu, Y. Zhang, Z. Li, Y. Li, Y. Wang, Y. Guo, and W. Li, "Equivalent Circuits For Single-Sided Linear Induction Motors", *IEEE Trans. Ind. Appl.*, vol. 46, no. 6, pp. 2410-2423, 2010.

[12] S. G. Lee, H. Lee, S. Ham, C. Jin, H. Park, and J. Lee, "Influence of the Construction of Secondary Reaction Plate on the Transverse Edge Effect in Linear Induction Motor", *IEEE Trans. Magn.*, vol. 45, no. 6, pp. 2815-2818, 2009.

[13] A. Z. Bazghaleh, M. R. Naghashan, and M. R. Meshkatoddini, "Optimum Design of Single-Sided Linear Induction Motors for Improved Motor Performance", *IEEE Trans. Magn.*, vol. 46, no. 11, pp. 3939–3947, 2010.

[14] A. Z. Bazghaleh, M. R. Naghashan, M. R. Meshkatoddini, and H. Mahmoudimanesh, "Optimum Design of High Speed Single-Sided Linear Induction Motor to Obtain Best Performance", *IEEE Conf. Power Electronics & Electrical Drive, Automation & Motion, SPEEDAM*, pp. 1222-1226, 2010.

[15] A. Z. Bazghaleh, M. R. Naghashan, M. R. Meshkatoddini, and H. Mahmoudimanesh, "Optimum Design of High Speed Single-Sided Linear Induction Motor using Particle Swarm Optimization", *IEEE Conf. Power Electronics & Drive Systems & Technologies, PEDSTC*, pp. 329-334, 2010.

[16] J. F. Gieras, G. E. Dawson, A. R. Easthan, "A New Longitudinal End Effect Factor for Linear Induction Motor", *IEEE Trans. Energy Convers.*, vol. 2, no. 1, pp. 152-159, 1987.

[17] R. C. Creppe, J. A. C. Ulson and J. F. Rodrigues, "Influence of Design Parameters on Linear Induction Motor End Effect", *IEEE Trans. Energy Convers.*, vol. 23, no. 2, pp. 358-362, 2008.

[18] J. Lu and W. Ma., "Research on End Effect of Linear Induction Machine For High-Speed Industrial Transportation", *IEEE Trans. Plasma Sci.*, vol. 39, no. 1, pp. 116-120, 2011.

[19] T. Yang, L. Zhou, and L. Li, "Influence of Design Parameters on end Effect in Long Primary Double-Sided Linear Induction Motor", *IEEE Trans Plasma Sci.*, vol. 39, no. 1, pp. 192-197, 2011.

[20] I. Boldea and S. A. Nasar, *Linear motion electromagnetic devices*, Taylor & Francis, New York, 2001.

[21] S. A. Nasar and I. Boldea, Linear electric motors, Prentice-Hall, New Jersey, 1987.

[22] M. Mirsalim, A. Doroudi, and J. S. Moghani, "Obtaining the Operating Characteristics of Linear Induction Motors: A New Approach", *IEEE Trans. Magn.*, vol. 38, no. 2, pp. 1365-1370, 2002.

[23] E. R. Laithwaite, Induction machines for special purposes, George Newnes Limited, London 1996.

[24] R. M. Pai, I. Boldea, and S. A. Nasar, "A Complete Equivalent Circuit of a Linear Induction Motor with Sheet Secondary", *IEEE Trans. Magn.*, vol. 24, no. 1, 1988.

[25] J. F. Gieras, *Linear Induction Drives*, Oxford University Press, New York, 1994.

Abbas Shiri was born in Hashtrood, Iran in 1980. He received the B.Sc. degree from Tabriz University and M.Sc. degree from Iran University of Science and Technology (IUST) both in electrical engineering in 2004 and 2006, respectively. He is currently working toward Ph.D. degree in electrical engineering at IUST.

His areas of research interests include linear electric machines, electromagnetic systems and actuators, electrical machine design and modeling.

Abbas Shoulaie was born in Isfahan, Iran, in 1949. He received the B.Sc. degree from Iran University of Science and Technology (IUST), Tehran, Iran, in 1973, and the M.Sc. and Ph.D. degrees in electrical engineering from U.S.T.L, Montpellier, France, in 1981 and 1984, respectively.

He is a Professor at the department of Electrical Engineering, IUST. He is the author of more than 100 journal and conference papers in the field of power electronics, electromagnetic systems, electrical machine, linear machine and HVDC.

Simulation and Analysis of HEMP Coupling Effect on a Wire Inside an Apertured Cylindrical Shielding Cavity

Shu-Ting Song, Hong Jiang, Yu-Lan Huang

College of Communication Engineering
Jilin University, Changchun, Jilin Province 130012, China
Email: shadoushi@163.com, jiangh@jlu.edu.cn, ylhuang@jlu.edu.cn

Abstract ─ High altitude nuclear electromagnetic pulse (HEMP) can damage electronic equipments of radar and communication systems. Back door coupling is one of the main ways of HEMP attacks on the electronic devices. In this paper, the three-dimensional (3D) electromagnetic (EM) simulation software MicroStripes7.5, which is based on the transmission line matrix (TLM) method, are employed to investigate the HEMP coupling effect on a wire located inside a cylindrical shielding cavity having one or few apertures. The EM models of the wire and the apertured shielding cavity are constructed, and the induced wire currents through the aperture of cavity are simulated. By comparing the simulation results of the wire with and without shield of the cavity, the shielding effectiveness (SE) is calculated. Further, the effects on induced wire in various cases are compared and analyzed, including single-aperture and multiple-aperture, different incident angles, polarization angles, and wire locations. Also, the cylindrical cavity is compared with the rectangular cavity.

Index Terms ─ Aperture, cylindrical cavity, EM simulation, HEMP, wire current.

I. INTRODUCTION

With the miniaturization of electronic and electrical equipments and systems, the electronic equipments become more sensitive and vulnerable to electromagnetic pulses (EMP). High altitude nuclear electromagnetic pulse (HEMP) is produced by nuclear explosion at high altitude, characterized by intense electric field strength, short duration, wideband frequency coverage and wide range coverage, which can damage electronic equipments of radar and communication systems, wires, crystal diodes, transistors, integrated circuits resistors, capacitors, filters, relays and other components. HEMP protection technologies and methods [1] have become one of the most important research fields in many applications.

Back door coupling through apertures is one of the main ways of HEMP attacks on the electronic devices. Some literatures have studied the methods of wire coupling effects of electromagnetic pulse. For example, the electromagnetic field energy flow on a thin wire is measured using Hallén integral equations [2]. Resonance of the wire is formulated using the theory of the linear antenna [3]. A 'diffuse-field reciprocity principle' has been applied to electromagnetic (EM) systems, enabling the currents induced in a wiring system to be computed in an efficient manner [4].

However, most of these researches focus on the coupling effects of unshielded wire. In practice, wires are often in enclosure by a shielding cavity for the electromagnetic pulse protection. Inevitably, if the shielding cavity has one or some apertures, the wire induced circuits will be produced through aperture coupling.

For aperture coupling, some methods have been proposed. An efficient hybrid method is developed for calculating EMP coupling to a device on a printed circuit board inside a cavity with an aperture [5]. The EM coupling through a thick aperture in multilayer planar circuits has been analyzed using extended spectral domain approach and finite difference time-domain

Submitted On: Oct. 30, 2011
Accepted On: April 25, 2012

(FDTD) method [6]. EMP coupling rules of different apertures is also researched and the rules of coupling energy are discussed in the condition of different polarization [7]. The fast prediction of the electromagnetic shielding performances of aperture loaded by resistive thin film coatings is investigated [8].

As for the shielding effectiveness (SE) of a cavity, the rectangular shielding cavity has been mostly studied so far, for example, the SE is evaluated for a rectangular enclosure with numerous apertures [9]. Based on the method of moments (MoM), the SE of rectangular enclosures with thin and thick Apertures has been analyzed [10]. The SE of rectangular metallic enclosures with apertures, metal plates, and conducting objects is calculated using fast MoM [11]. The SE of rectangular enclosures with apertures using transmission line matrix (TLM) method is analytically formulated [12]. However, a few are for the cylindrical shielding cavity.

In this paper, we will investigate the HEMP coupling effect on a wire which is located inside an apertured cylindrical shielding cavity using MicroStripes7.5, 3D EM simulation software. We will construct the EM models of the wire and the cylindrical shielding cavity with one or few apertures, and simulate to obtain the induced wire current through apertures of cavity. By comparing the simulation results of the wire with and without shield of the cavity, we calculate the shielding effectiveness. Further, we will compare and analyze the affects of induced wire currents under various conditions, including single-aperture and multiple-aperture, different incident angles, polarization angles and wire locations. Also, we compare our cylindrical cavity with traditional rectangular cavity.

II. EM SIMULATION SOFTWARE AND TLM METHOD

3D EM simulation software MicroStripes7.5 is used in this paper to analyze the HEMP coupling effect on a wire located in an apertured cylindrical shielding cavity. MicroStripes7.5 is based on the TLM method.

The TLM method is a time-domain, differential numerical technique for modeling electromagnetic and other field problems, especially for wideband incident wave coupling like HEMP. The details of the TLM theory can be found in [13]. Its computational efficiency, stability, and calculation accuracy have all been well proven. Also, TLM is unconditionally stable, the time step being determined by the mesh resolution. TLM has some advantages over frequency domain FDTD. Firstly, it can exactly calculate electric and magnetic fields on the same mesh, without the half cell offset characteristic of FDTD. In the TLM method, both space and time are in discrete form in order to implement Huygens' model on a digital computer, and the networks containing series and shunt nodes are adopted to simulate different situations of propagation. The currents of series-wound nodes are calculated in the scattering matrix [14]. The comparison between measurements and TLM method shows good agreement in analyzing a wire placed inside a rectangular cavity with an aperture [15].

MicroStripes7.5 software has been extensively used in vehicles, ships, aviation, and also employed in the evaluation of human absorption of electromagnetic fields, to solve the issues of antenna design, installation performance assessment, RF or microwave devices, radar cross section (RCS), electromagnetic compatibility (EMC), electromagnetic interference (EMI), electromagnetic pulse (EMP), and lightning strikes and other issues.

III. HEMP WAVEFORM

HEMP waveform standards promulgated by the standard of MIL-STL-461F [16] is adopted in this paper, the electric field description can be expressed as

$$E(t) = kE_p(e^{-\alpha t} - e^{-\beta t}) \qquad (1)$$

where $k = 1.3$, $E_p = 50kV/m$, $\alpha = 4\times10^7 s^{-1}$, $\beta = 6\times10^8 s^{-1}$.

We take an observation point in infinite space near the ground. HEMP incident wave in time domain and frequency domain can be simulated by MicroStripes7.5, as shown in Fig. 1.

It is shown from Fig. 1 that the HEMP energy mainly focuses on the frequency range of 200 ~ 300*MHz*, and the energy is small when the frequency is over 3GHz. Therefore, the following simulation and analysis of coupling currents focus on the frequency range of 0~3GHz.

In the following, except Section VI and VII, the HEMP incident angles of elevation is 10°, the

azimuth angles is 30°, and the polarization angle is 30°.

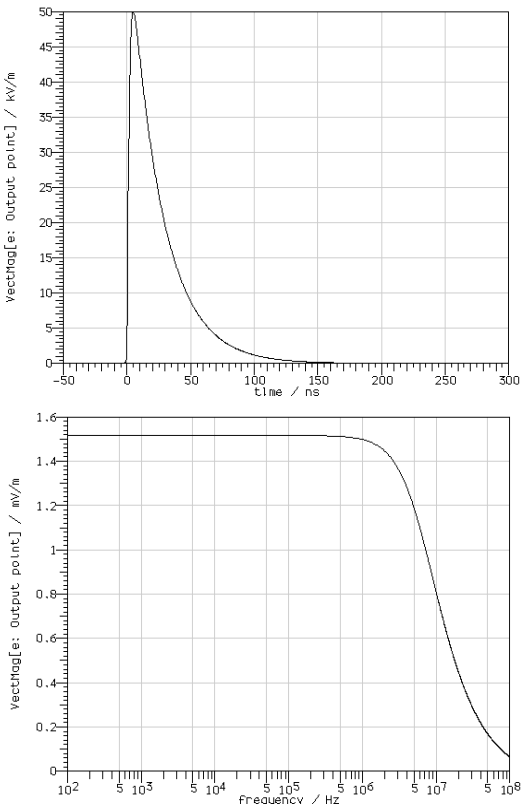

Fig. 1. HEMP incident wave in time domain and frequency domain described by MIL-STL-461F standard.

IV. SIMULATION MODELING AND ANALYSIS OF WIRE CIRCUIT IN A CYLINDRICAL SHIELDING CAVITY

A. Simulation Model

In this section, a wire and a cavity are modeled in the EM simulation. Their parameters are shown in Table 1.

Table 1: Parameters of the wire and cavity

	Radius	**Length**	**Wall thickness**	**Height above ground**
wire	0.25mm	13cm		11cm
cavity	5cm	20cm	0.5cm	6cm

The wire is assumed to be an ideal conductor line whose resistivity $\gamma \to 0$, being placed parallel to the ground, without a shield of a cavity. The model of an unshielded wire is built using the simulation software, shown in Fig. 2.

In Fig. 3, the wire is insulately located inside a cylindrical cavity with a single aperture. On the bottom of the cavity, there exists a rectangular aperture with the size of $0.5\text{cm} \times 3\text{cm}$. The conductivity of the cavity walls is 1×10^{7} s/m and the relative permeability is 200. Thus, we can consider the cavity walls as a nearly perfect conductor. The cavity is placed parallel to the ground, and is 6cm above to the ground.

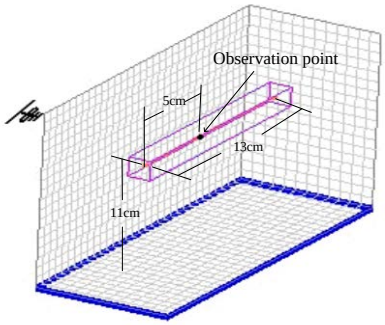

Fig. 2. The model of an unshielded wire.

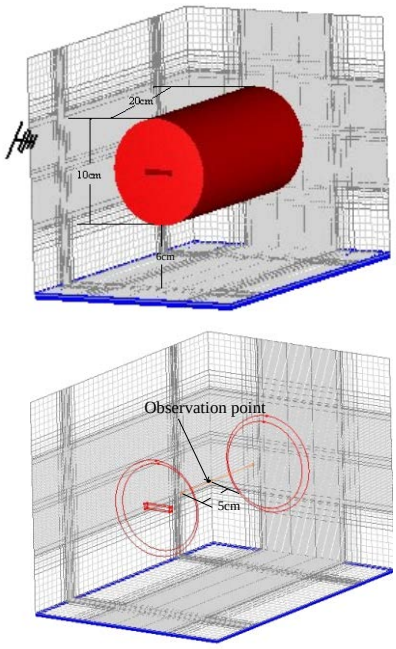

Fig. 3. The model of a wire inside a cylindrical cavity with a single aperture.

In the simulation, we put two observation points on the wire in Fig. 2 and Fig. 3, respectively. The observation point on the unshielded wire (without the cavity) is named as Ioutput1, and the observation point on the wire inside the cavity is named as Ioutput2. The two

observation points are all 5cm distances from the front terminal of the wire.

B. Results Analysis

The time-domain waveforms of Ioutput1 and Ioutput2 are shown in Fig. 4 and Fig. 5.

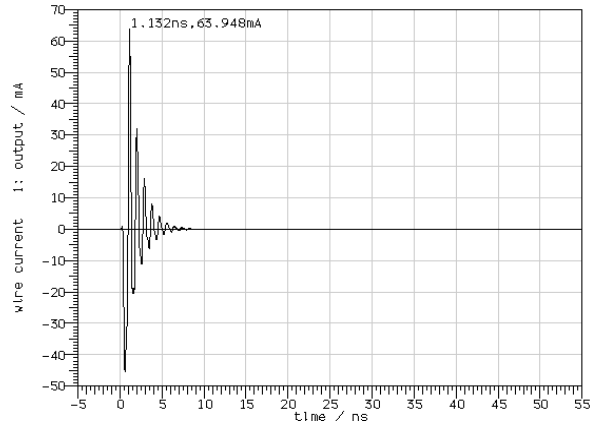

Fig. 4. Ioutput1's waveform of current in time domain.

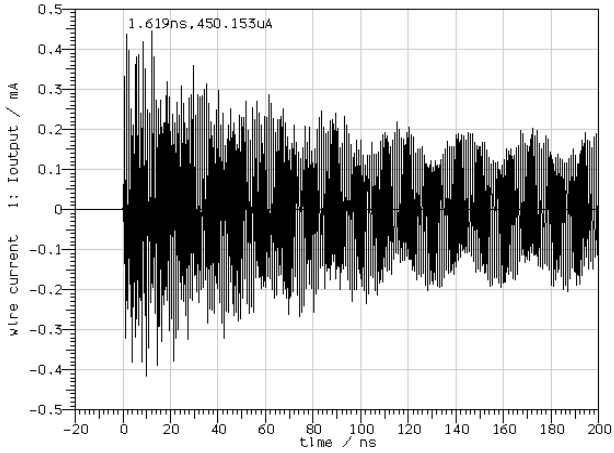

Fig. 5. Ioutput2's waveform of current in time domain.

Since the induced currents on the wire bounces back and forth due to reflection, waveform oscillation is formed, as shown in both Fig. 4 and Fig. 5. With the increase of time, the induced wire currents periodically oscillate and gradually attenuate. The maximum oscillation amplitude at Ioutput1 point is I_{o1} =63.948mA, occurring at the time of 1.132ns, and then it gradually decays to zero after 10ns.

The wire current inside the cavity is mainly high-frequency oscillating current due to the reflection of the cavity walls. Electromagnetic pulse energy is coupled into the shielding cavity and resonance is generated. Then high-frequency oscillatory current is induced in the wire. In the initial time, the amplitude of oscillation current is high, the maximum oscillation amplitude at Ioutput2 point is I_{o2} =450.153μA.

Therefore, compared with the wires with and without a shield of the cavity, the shielding effectiveness is $SE = 20\log\frac{I_{o1}}{I_{o2}} = 43dB$. That is, the induced wires current with a shield of the cavity is decreased by 43dB.

The frequency-domain waveforms of Ioutput1 and Ioutput2 are shown in Fig. 6 and Fig. 7 respectively. By analyzing the frequency spectrum, we can see that, within the frequency-range of 0~3GHz, the optimal coupling frequency is between 1.00GHz ~ 1.10GHz and 2.00GHz ~ 2.10GHz. Comparing the two figures, we can also see that, since the wire inside the cavity is shielded, the current components coupled into the wire are much smaller than the case of the wire without shielding cavity. From this, we know that the cavity with aperture plays a very good role of protection. In practice, specific evaluation of protective levels is based on the damage threshold of the electronic equipment inside the cavity.

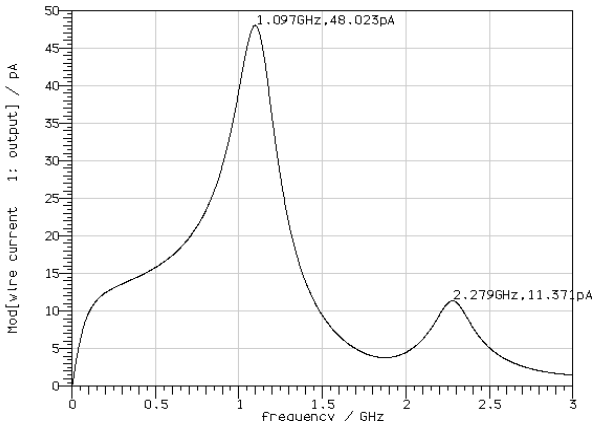

Fig. 6. Ioutput1's waveform of current in frequency-domain.

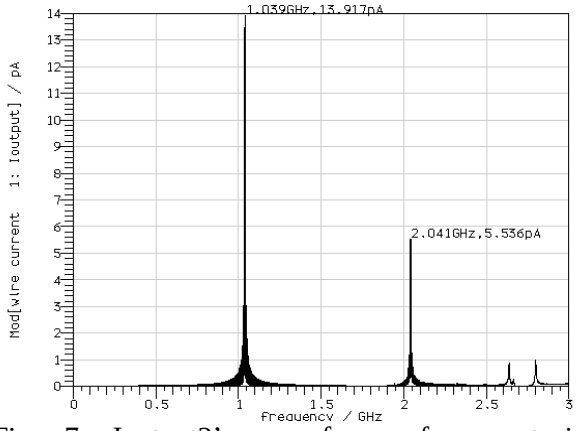

Fig. 7. Ioutput2's waveform of current in frequency-domain.

V. SIMULATION AND ANALYSIS OF THE IMPACT OF THE NUMBERS OF APERTURES

A. Simulation Model

In this section, we compare the impact of different numbers of apertures on the induced current based on two models. The two models are shown in Fig. 8 and Fig. 9, respectively.

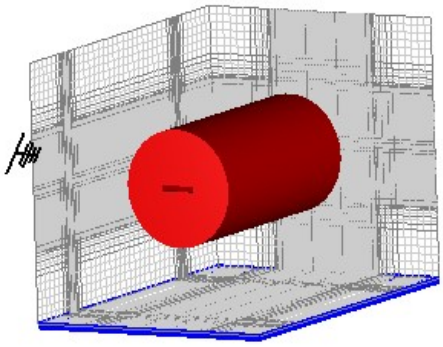

Fig. 8. Single aperture.

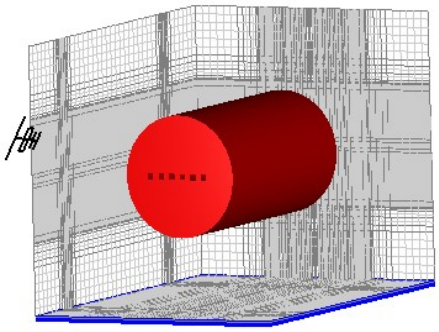

Fig. 9. Multiple apertures.

The material in both Fig. 8 and Fig. 9 is iron. The cavity parameters are the same as in Section IV. The single aperture model in Fig. 8 is a rectangular aperture with size of 0.5cm×3cm. The multiple aperture model in Fig. 9 are composed of six same squares with side length of 0.5cm, the total area of which is the same as in Fig. 8.

Inside the cavity, we insulately place a wire having the same parameters as in section IV. The observation points are 6cm distances from the front terminal of the wire.

B. Results Analysis

Figure 10 and Fig. 11 show the time-domain current waveforms of the wire located inside the cavities with single aperture and multiple apertures, respectively.

It is shown that the maximum coupling current peak of the wire inside the cavity with single-aperture is 449.889μA. However, the maximum value inside the cavity with multiple-aperture is 8.303μA, which is lower than that of the single-aperture cavity. Compared with single-aperture, the shielding effectiveness of multiple-aperture is increased by 34.7dB.

Therefore, by increasing the number of apertures the shielding effectiveness is much increased while keeping the total area the same. The reason can be analyzed similarly to the rectangular apertured cavity case in [12] using analytical formulation of shielding effectiveness modeling aperture as impedance.

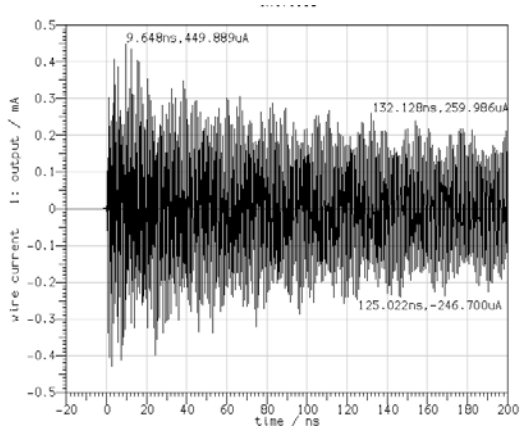

Fig. 10. Wire current waveform of single-aperture cavity.

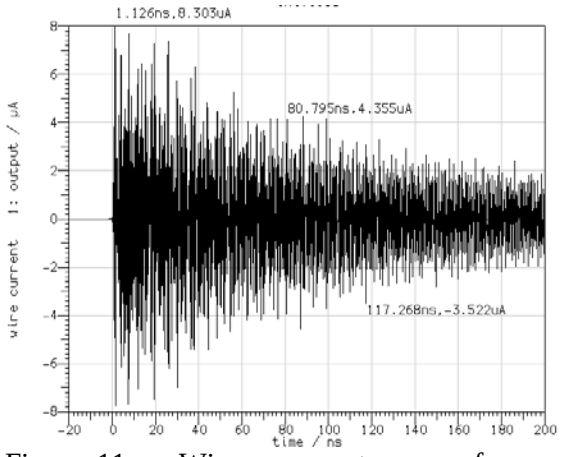

Fig. 11. Wire current waveform of multiple-aperture cavity.

VI. AFFECT OF THE INCIDENT ANGLE

In this section, we compare the affect of different HEMP incident angles. Figures 12 - Fig. 15 show the current waveform for different incident elevation angles, they are 0°, 10°, 60° and 90°.

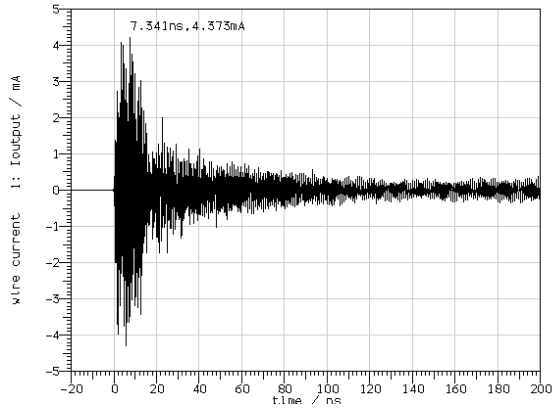

Fig. 12. Current waveform of 0° incident angle.

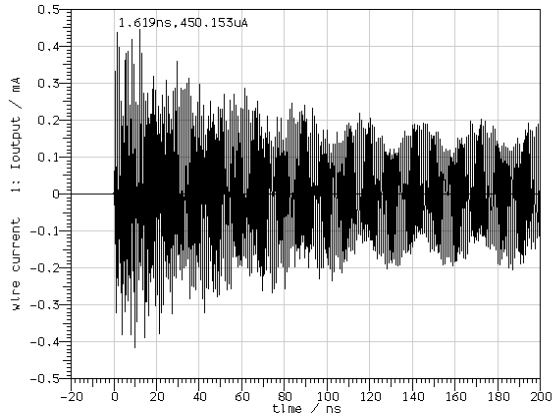

Fig. 13. Current waveform of 10° incident angle.

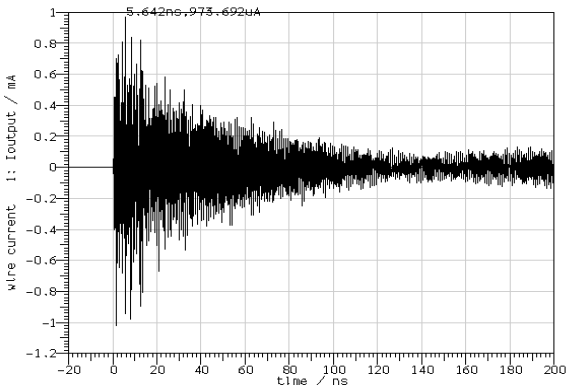

Fig. 14. Current waveform of 60° incident angle.

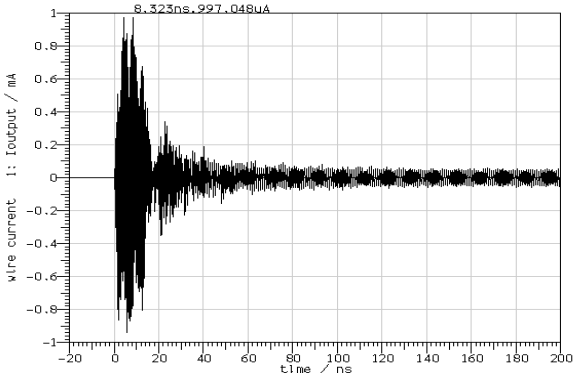

Fig. 15. Current waveform of 90° incident angle.

From Fig. 12 to Fig. 15, we know that on the condition of 0° incident angle, the current on the wire is the largest. The maximum amplitude is over 4mA. After the coupling of HEMP, the amplitude of the current oscillates in the range from 300μA to 450μA. For other incident angles, the maximum amplitude of the wire current during the coupling period is below 1mA, and changes very little with the change of the incident angle. The comparison of maximum current amplitude for different incident angles are listed in Table 2.

Table 2: The maximum current amplitude for different incident angles

Incident angle	0°	10°	60°	90°
Maximum current amplitude	4.373 mA	450.153 μA	973.692 μA	997.048 μA

VII. AFFECT OF THE POLARIZATION ANGLE

We further study the affect of different HEMP polarization angles while the incident angles are the same. Figure 16 - Fig. 19 show the current waveform in frequency-domain for different polarization angles, they are 0^o, 30^o, 60^o and 90^o.

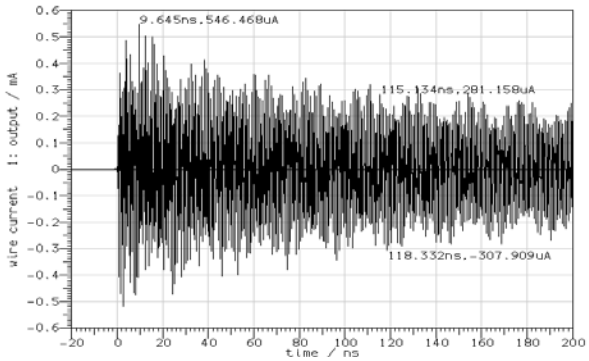

Fig.16. Current waveform of 0^o polarization angle.

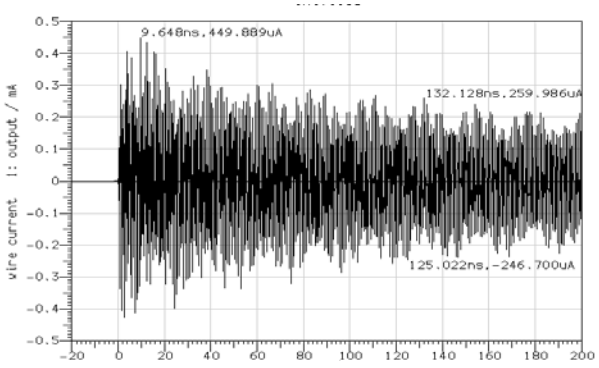

Fig.17.Current waveform of 30^o polarization angle.

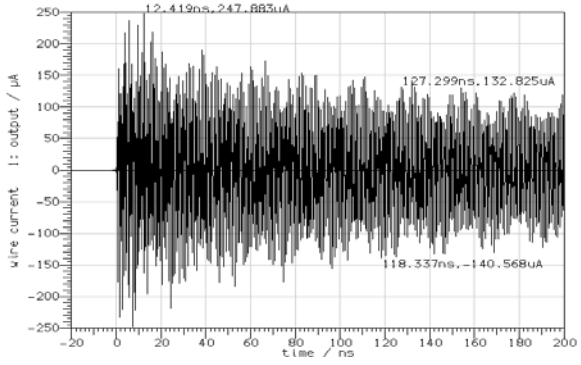

Fig.18.Current waveform of 60^o polarization angle.

From Fig. 16 to Fig. 19, we know that on the condition of 0° polarization angle, the current on the wire is the largest. Besides with the increase of the polarization angle, the amplitude of the current decreases. When the polarization angle is 90°, the current on wire decays the most fast. The comparing table of the currents' biggest amplitude in different cases is listed in Table 3.

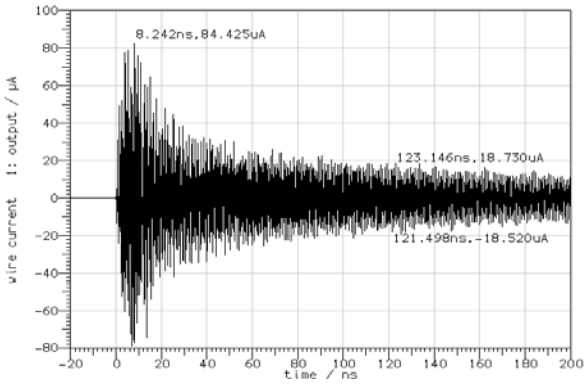

Fig.19. Current waveform of 90^o polarization angle.

Table 3: The maximum current amplitude for different polarization angles

Polarization angle	0°	30°	60°	90°
Maximum current amplitude	546.47 µA	449.9 µA	247.88 µA	84.425 µA

VIII. AFFECT OF THE LOCATION OF WIRE INSIDE THE CAVITY

In this section, two different locations of the wire inside the cavity are compared. The model and results analysis are shown as follows:

A. Simulation Model

The parameters of the cavity and the wire are the same as in Section IV. However, the wire is placed at two different locations in the cavity.

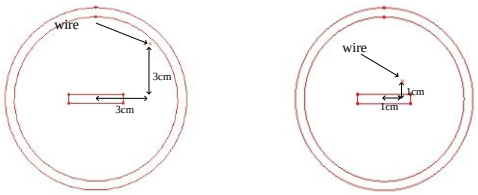

(a) The wire near to wall. (b) The wire near to aperture.

Fig. 20. Vertical vision of the wire location.

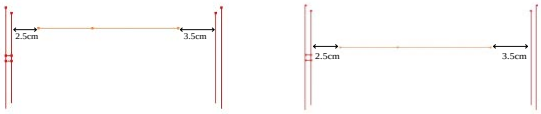

(a) The wire near to wall. (b) The wire near to aperture.

Fig. 21. Horizontal vision of the wire location.

Figure 20 and Fig. 21 show the vertical and horizontal visions of the wire location, respectively. The vertical and horizontal distances from the wire to the aperture and the cavity walls are shown in the figures.

B. Results Analysis

We put an observation point in the wire to observe the wire current, shown in Figure 21. The observation point in Figure 21(a) is named as I(1), and in Figure 21(b) is named as I(2).

Figure 22 shows the time-domain waveform on the wire, and Fig. 23 shows the frequency-domain waveform.

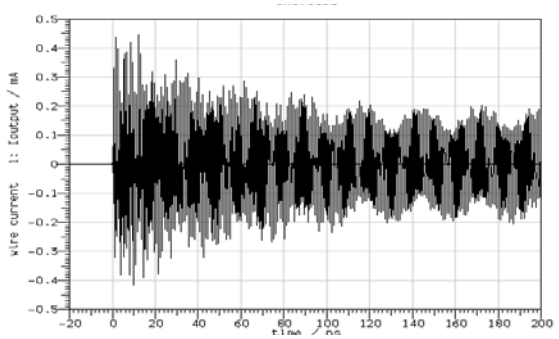

(a) The time-domain waveform of I(1)

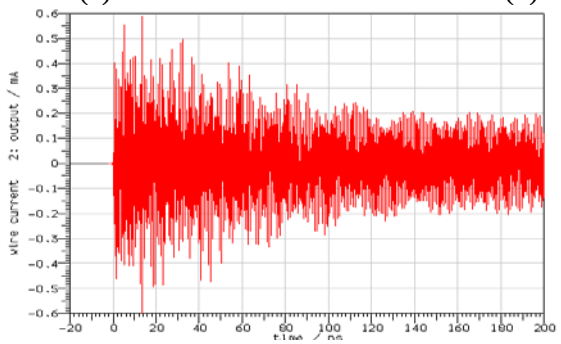

(b) The time-domain waveform of I(2)

Fig. 22. The current waveform in time domain.

By comparing the two conditions, we know that the optimal coupling frequency is between the 1.0 GHz - 1.10GHz and 2.0GHz - 2.2GHz, and the value of the amplitude changes with the changing of the wire's location. In the time-domain, the current maximum amplitude of I(1) is about 0.44mA, and current maximum amplitude of I(2) is about 0.59mA. The coupling affect of the aperture is stronger than that of the cavity wall.

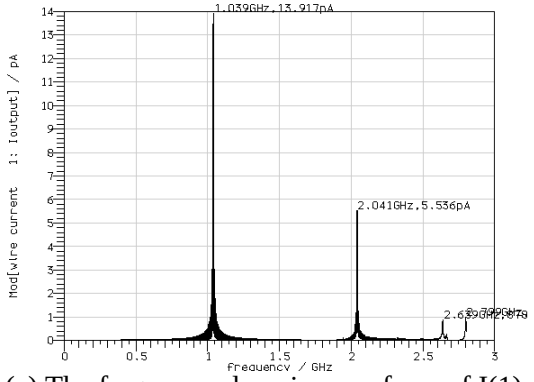

(a) The frequency-domain waveform of I(1)

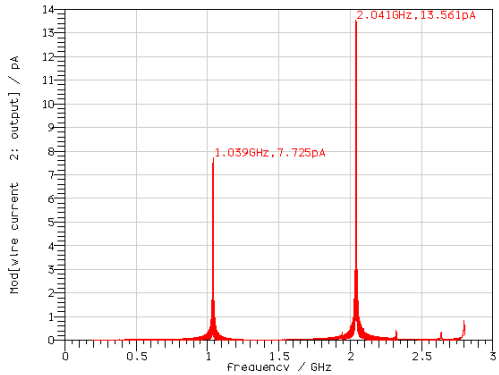

(b) The frequency-domain waveform of I(2).

Fig. 23. Current waveform in frequency-domain.

IX. COMPARISION BETWEEN CYLINDRICAL CAVITY AND RECTANGULAR CAVITY

A. Simulation Model

The size of the cylindrical cavity is the same as in section IV. The rectangular cavity has the parameters as follows: Its side length of the square bottom is 10cm, its length is 20cm, and its wall thickness is 0.5cm. The size of the aperture is also 0.5cm×3cm. Figure 24 shows the model of a wire inside a rectangular cavity with a single aperture. The wire is placed at the same location relative to the aperture as in the cylindrical cavity.

B. Results Analysis

For different shapes of cavity, the time-domain waveform is shown in Fig. 25 and Fig. 26. The amplitude value of the optimal coupling frequency is shown in Fig. 27 and Fig. 28.

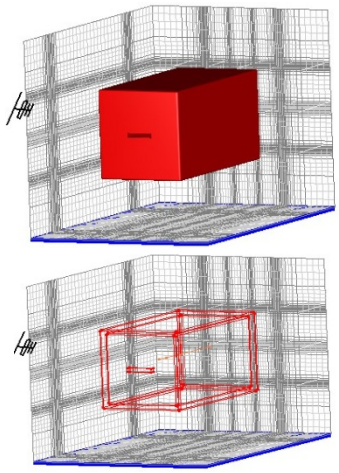

Fig. 24. The model of a wire inside a rectangular cavity with a single aperture.

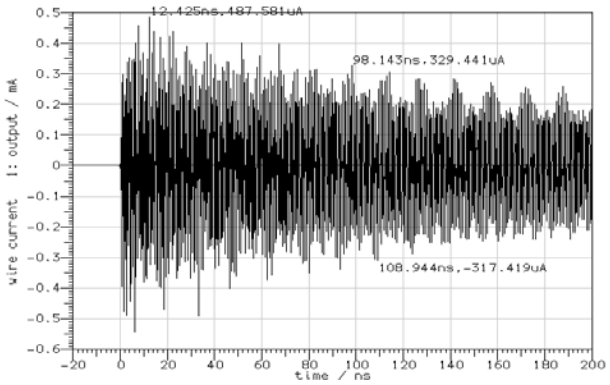

Fig. 25. The waveform of wire current for rectangular cavity.

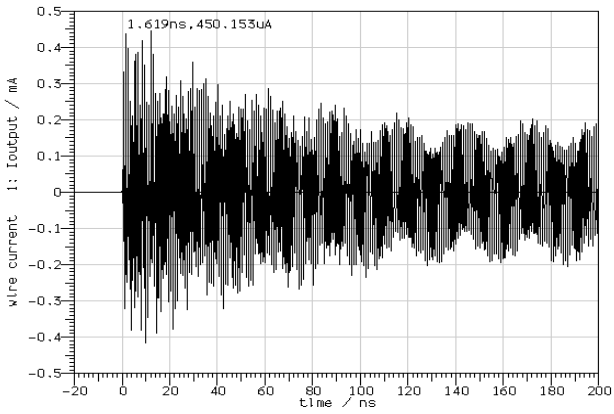

Fig. 26. The waveform of wire current for cylindrical cavity.

For the rectangular cavity, the maximum current amplitude is about 487.581μA, the amplitude of high-frequency oscillating current is about 300μA after the coupling of HEMP, the two optimal coupling frequencies are 1.072GHz and 2.075GHz, and the their corresponding amplitudes are respectively 12.446pA and 2.695pA. While for the cylindrical cavity, the maximum current amplitude is about 449.889μA, the amplitude of high-frequency oscillating current is about 250μA after the coupling of HEMP, the two optimal coupling frequencies of the cylindrical cavity is 1.054GHz and 2.064GHz, and their corresponding amplitudes are respectively 10.7pA and 3.919pA.

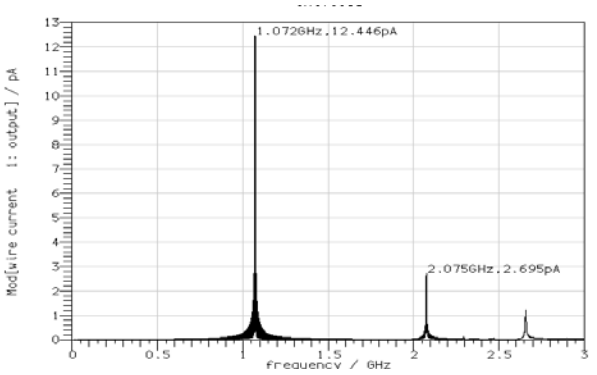

Fig. 27. The current amplitue of the optimal coupling frequency in rectangular cavity.

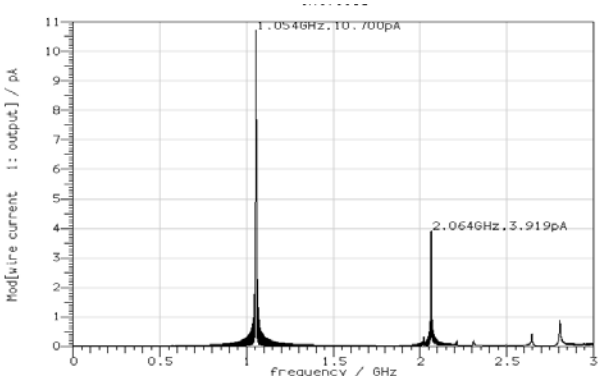

Fig. 28. The current amplitue of the optimal coupling frequency in cylindrical cavity.

X. CONCLUSION

In this paper, we exploit the EM simulation software MicroStripes 7.5 to simulate the environment of HEMP, modeling and analyzing the effect of HEMP coupling on the wire which is inside a shielding cylindrical cavity with apertures. Under the model of this experiment, the induced currents on the wire shielded by an apertured cavity are decreased about 43dB compared with on the wire without cavity. Aperture characteristic is the main factor which determines the strength of HEMP coupling to the cavity. When the total area

of the aperture is the same, the coupling coefficient of multiple-apertured cavity is much smaller than that of single-apertured cavity. Compared with single-aperture, the shielding effectiveness of multiple-aperture is increased by 34.7dB. When the HEMP incident elevation angle is 0° and the polarization angle is 0°, the induced current on the wire is larger than other angle cases. While the wire is near to the aperture, its induced current is larger than the case when the wire is near to the wall. Also, since the rectangular cavity and the cylindrical cavity of cavities have similar volume and size, the optimal coupling frequency and the amplitude of the high frequency components for the two shapes is close, the latter is a little bit smaller than the former in our simulation.

ACKNOWLEDGMENT

The authors would like to thank the reviewers for their useful comments and suggestions.

REFERENCES

[1] X. J. Zhang, J. Yang, Q. Y. Yuan, Z. X. Wang, X. J. Li, "Research on the Suppressing Behaviour of EMP Protection Device," *Cross Strait Quad-Regional Radio Science and Wireless Technology Conf.*, vol. 1, pp. 318-321, 2011.

[2] D. Poljak, V. Doriæ, V. Roje, "Transient Analysis of Buried Cables," *Proc. IEEE International Symposium on Antennas and Propagation*, Washington, USA: IEEE Press, vol. 1B, pp. 46-49, 2005.

[3] J. M. Myers, S. S. Sandler, T. T. Wu, "Electromagnetic Resonances of a Straight Wire," *IEEE Trans. Antennas Propagat*., vol. 59, no. 1, pp. 129-134, 2011.

[4] R. S. Langley, "A Reciprocity Approach for Computing the Response of Wiring Systems to Diffuse Electromagnetic Fields," *IEEE Trans. Electromagnetic Compatbility*, vol. 52, no. 4, pp. 1041-1055, 2010.

[5] C. Lertsirimit, D. R. Jackson, and R. Wilton, "An Efficient Hybrid Method for Calculating the EMC Coupling to a Device on a Printed Circuit Board inside a Cavity by a Wire Penetrating an Aperture," *Electromagnetics*, vol. 25, pp. 637-654, 2005.

[6] A. M. Tran, B. Houshmand, T. Itoh, "Analysis of Electromagnetic Coupling Through a Thick Aperture in Multilayer Planar Circuits Using the Extended Spectral Domain Approach and Finite Difference Time-Domain Method," *Antennas and Propagation*,vol.43, pp.921-926, 1995.

[7] A. Gademann, I. V. Shvets, C. Durkan, "Study of Polarization-dependent Energy Coupling between Near-field Optical Probe and Mesoscopic Metal Structure," *Journal of Applied Physics*, vol. 95, pp. 3988-3993, 2004.

[8] M. D'Amore, V. De. Santis, M. Feliziani, "Fast Prediction of the Electromagnetic Shielding of Small Apertures Coated by Conductive Thin Film," *2010 Asia-Pacific International Symposium on Electromagnetic Compatibility (APEMC)*, pp. 524-527, 2010.

[9] P. Dehkhoda, A. Tavakoli, R. Moini, "An Efficient and Reliable Shielding Effectiveness Evaluation of a Rectangular Enclosure with Numerous Apertures," *IEEE Trans. Electromagnetic Compatibility*, vol. 50, no. 1, pp. 208-212, 2008.

[10] R. Araneo and G. Lovat, "An Efficient MoM Formulation for the Evaluation of the Shielding Effectiveness of Rectangular Enclosures with Thin and Thick Apertures," *IEEE Trans. Electromagnetic Compatibility*, vol. 50, pp. 294-304, 2008.

[11]R. Araneo and G. Lovat, "Fast MoM Analysis of the Shielding Effectiveness of Rectangular Enclosures with Apertures, Metal Plates, and Conducting Objects," *IEEE Trans. Electromagnetic Compatibility*, vol. 51, pp. 274-283, 2009.

[12]M. P. Robinson,T. M. Benson, C. Christopoulos, etc., "Analytical Formulation for the Shielding Effectiveness of Enclosures with Apertures," *IEEE Trans. Electromagnetic Compatibility*, vol. 40, pp. 240-248, Aug. 1998.

[13] WJR Hoefer, "The Transmission Line Matrix Method—Theory and Applications," *IEEE Trans, Microwave Theory and Tech*. vol. MTT-43, no. 9, pp. 882-893, Oct. 1985.

[14]A. F. Yagli, J. K. Lee, and E. Arvas, "Monochromatic Scattering from Three-dimensional Gyrotropic Bodies Using the TLM Method," *Applied Computational Electromagnetic Society (ACES) Journal*, vol. 22, no. 1, pp. 155-163, 2007.

[15]A. P. Duffy, T. M. Benson, and C. Christopoulos, "Propagation Along a Wire Placed Inside a Cavity with an Aperture: A Comparison of Measurements and Transmission-Line Modeling (TLM)," *IEEE Trans. Electromagnetic Compatibility*, vol. 36, pp. 144-146, 1994.

[16]Requirements for the Control of Electromagnetic Interference Characteristics of Subsystems and Equipment [S], MIL-STD-461F, Re 10, December 2007.

Shu-Ting Song received the B.S. degree in Communication Engineering from Jilin University, China, in 2010. She is currently a graduate student at College of Communication Engineering, Jilin University, China. Her current research interest is EM simulation in computational electromagnetics.

Hong Jiang received the B.S. degree from Tianjin University, China, in 1989, the M.S. degree in Communication and Electronic System from Jilin University of Technology, China, in 1996, and the Ph.D. degree in Communication and Information System from Jilin University, China, in 2005. From May 2010 to May 2011, she had worked as a visiting research fellow at McMaster University, Canada. Currently, she is an associate professor at the College of Communication Engineering, Jilin University, China. She is a senior member of the Chinese Institute of Electronics (CIE). Her research fields focus on electromagnetic protection, signal processing for wireless communication. She has published over 40 papers.

Yu-Lan Huang is an associate professor at the College of Communication Engineering, Jilin University, China. Her current research fields involve simulation of wireless communication networks and microwave technology.

Planar Circular Monopole Antenna with Perforated Dielectric Resonator for Notched Ultra-Wide Band Applications

Saber H. Zainud-Deen[1], Ahmed Shaker [2], and K. R. Mahmoud[2]

[1] Faculty of Electronic Engineering, Menoufiya University, Menouf, Egypt
anssaber@yahoo.com

[2]Department of Electronics and Communications Engineering, Faculty of Engineering, Helwan University, Cairo, Egypt
shakerelhagar@yahoo.com,kurany_hameda@h-eng.helwan.edu.eg

Abstract **-**In this paper, a planar circular patch antenna is presented for UWB operating characteristics. The bandwidth of the proposed antenna is increased by inserting a perforated dielectric resonator (DR) material with the planar monopole. The design combines the advantages of a small size dielectric resonator (DR) and thin planar monopole antennas. Two antenna designs A and B are proposed. In design A, two layers of the same dielectric material are presented with the same radius and different thicknesses. While in antenna design B, only one dielectric material layer perforated by 11 holes drilled with the same radius is considered. The effects with respect to the geometric parameters of the proposed antennas on impedance bandwidth and radiation pattern are discussed. In addition, the two proposed antennas are designed to have a rejection frequency band from 5 to 6 GHz by inserting two U-shaped slots in the ground plane, where the WLAN service is allocated. The proposed antennas are completely designed and analyzed using the finite element method (FEM), and then the finite integral transform (FIT) technique is used to check the validity of the numerical results.

Index Terms**-**Band notched, dielectric resonator antenna (DRA), FEM, FIT, ultra-wideband (UWB).

I. INTRODUCTION

Recently, ultra-wide band (UWB) technology has been attracting much attention for communication systems especially since the U.S. Federal Communications Commission (FCC) began allowing use of the band from 3.1 to 10.6 GHz for commercial applications [1]. UWB systems have widely been exploited in the wireless short-range high throughput communication operating over the same frequency range. To satisfy such requirement, various ultra-wide band antennas have been studied [2-3]. The UWB antennas have been designed with a specification of constant gain and linear phase response. Moreover, the antenna should have good impedance matching characteristics over the whole UWB frequency range. Planar monopole antennas are very suitable for UWB applications [4]. However, due to the overlap of currently allocated UWB frequency band with the existing wireless local area network (WLAN) (5.15 - 5.825GHz), special characteristics such as band notch are much desired for UWB antennas to reduce the interference between those two communication systems [5-6]. Accordingly, an ultra-wide band antenna with a band-notch characteristic can be an alternative choice to the use of a distinct stop-band filter in the system. One simple way is to etch thin slots in the antenna surface [7] to achieve the band-notched characteristic.

Submitted On: Dec. 29, 2011
Accepted On: Feb. 23, 2012

A dielectric resonator antenna (DRA) has a minimum of metal parts and mainly consists of dielectric materials mounted over a metal ground plane. DRAs have been of interest for the last three decades due to its attractive features like high radiation efficiency, lightweight, small size, low loss, and ease of excitation [8]. DRAs found many applications in wireless communications such as cellular communications operating over a wide frequency band [9].An ultra-wide band DRAs are presented in [10]. A novel compact UWB dielectric resonator antenna for UWB short-range wireless communication systems has been presented in [11]. In [12], the UWB dielectric resonator antenna having consistent omnidirectional pattern and low cross-polarization is presented. Ultra wideband dielectric resonator antenna with band rejection is studied in [13].

In this paper, a simple compact monopole type dielectric resonator antenna is presented. The design combines the advantages of small size dielectric resonator antenna (DRA) and thin planar circular monopole antenna. The dielectric resonator is inserted with monopole antenna where it is shaped to house the excitation feed. Two proposed designs A and B are presented to operate in the UWB range. The coplanar waveguide (CPW) is used to feed the antennas. Then, U-shape slots etched on the ground plane is considered to achieve the notched band from 5 to 6 GHz, to prevent interference between the UWB communications and the WLAN systems. Simulations have been carried out with the finite element method (FEM) to determine the antenna return loss bandwidth, gain, and radiation pattern [14-15]. Numerical results are checked with those obtained by the finite integration technique (FIT) to validate the results [16].

The paper is organized as follows: In Section 2, the simulation and optimization for the two proposed UWB antennas A and B are demonstrated. In Section 3, the notched UWB antennas are presented. Finally, the conclusions are drawn in Section 4.

II. ANTENNAS DESIGN AND NUMERICAL RESULTS

Figure 1 shows the geometry of the planar circular monopole antenna. The antenna is printed on an RT6002 substrate with thickness of 0.762 mm and relative permittivity of 2.94. The antenna is composed of the radiation circular patch of radius R_p, and partial ground L_g x W. The coplanar waveguide is used to feed the antenna. The feed gap G_3 can be used to adjust the impedance matching. The antenna parameters are listed in Table 1.

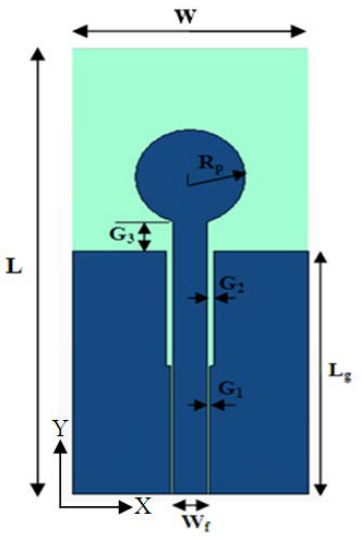

Fig. 1.The geometry of the planar circular monopole antenna.

Table 1: Parameters of the planar circular monopole antenna (all dimensions are in mm)

L	W	L_g	G_1	G_2	G_3	R_p	W_f
33	15	2.54	0.15	0.45	2	3.5	2.16

Figure 2 shows the variation of the power reflection coefficient and the gain of the antenna versus the frequency. It is clearly shown that the return loss < -10 dB occurs over the frequency range from 4.1 to 5.9 GHz with gain variation from 2 to 3 dB and from 7.7 to 9.3 GHz with gain variation from 1 to 1.2 dB. The simulated radiation patterns of the antenna at frequencies 5 and 8.2 GHz in different planes are shown in Fig.3. Simulations have been carried out with FEM and compared with those calculated by the FIT method. It can be observed that, good agreement is obtained. The results show that the radiation pattern is nearly omnidirectional in the H-plane and monopole-like radiation pattern in the E-plane.

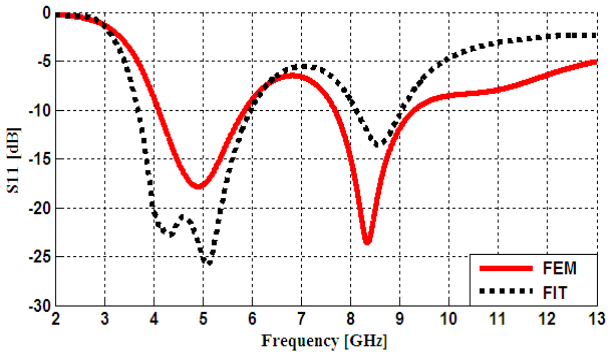

(a) Reflection coefficient frequency response.

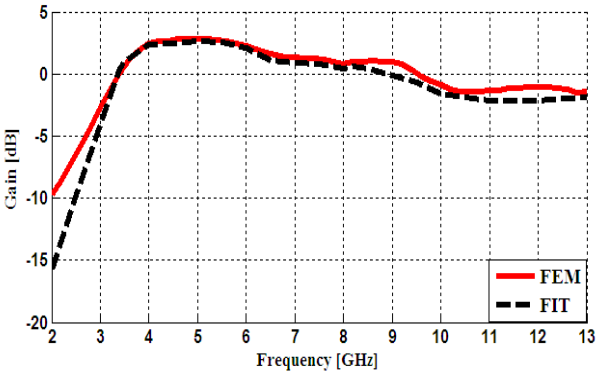

(b) Antenna gain frequency response.

Fig. 2. The simulated frequency response results of the planar circular monopole antenna using FEM and FIT methods.

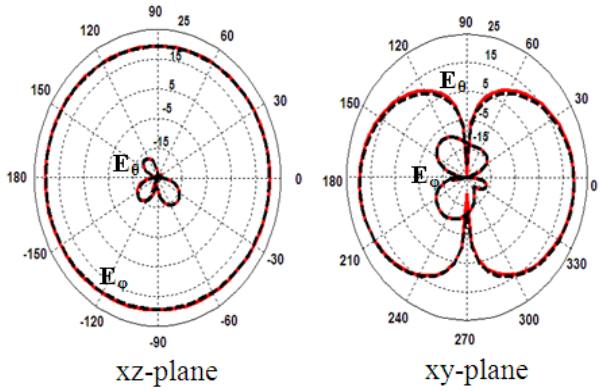

(a) f = 5 GHz

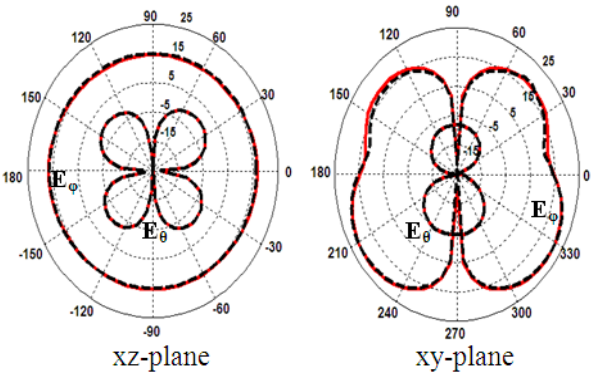

(b) f= 8.2 GHz

Fig. 3. The simulated radiation patterns of the planar circular monopole antenna in xz and xy-planes at different frequencies.
____ FEM --- FIT

A. Antenna design A

In this antenna design, the circular monopole antenna is inserted within cylindrical DRA with two layers of the same dielectric material with a relative dielectric constant ε_r = 10.2. Both layers have the same radius of W/2 with different thicknesses of T_1 = 3.54 mm and $T_2 = T_1/2$ for lower and upper layers, respectively. The upper one is perforated by five holes drilled into the dielectric material to change its effective dielectric constant [17]. The radius of each hole and the separation between holes are optimized for wider antenna impedance bandwidth. Figure4 shows the construction of the proposed antenna where the diameter of wider holes is d_1 = 1.8 mm , the diameter of other holes is d_2 = 1.25 mm, and the separation between the holes is S= 5.41 mm. Figure5 depicts the simulated power reflection coefficient and antenna gain for the antenna design A. It obviously indicates that an UWB bandwidth covering from 3.2 GHz to 11.2 GHz with a ratio of about115% is achieved for the proposed antenna. The gain varies from 3 dB to 6 dB over the operating frequency range. It can be concluded that the gain variation is 3dB over the entire operating frequency range (3.2 to 11.2 GHz). The simulated radiation patterns of the proposed antenna at 3.4, 6.2, and 7.8 GHz in different planes are illustrated in Fig.6, respectively. The results show that the radiation pattern is quite stable as the frequency changes with a nearly

omnidirectional radiation pattern in the H-plane and the monopole-like radiation patterns in the E-plane.

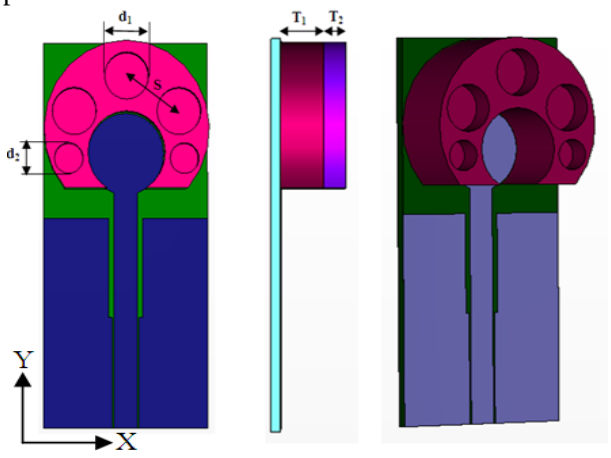

(a) Top view (b) Side view (c) Three dimension

Fig. 4.The geometry of the proposed antenna design A.

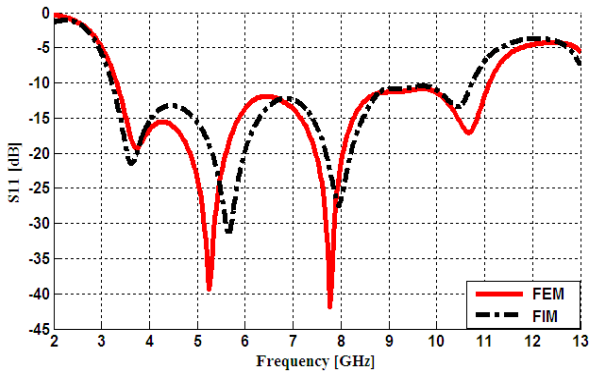

(a) Reflection coefficient frequency response.

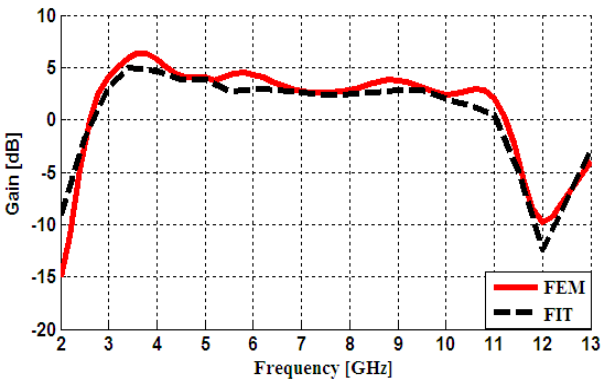

(b) Antenna gain frequency response

Fig. 5. The simulated frequency response results of proposed antenna design A using FEM and FIT.

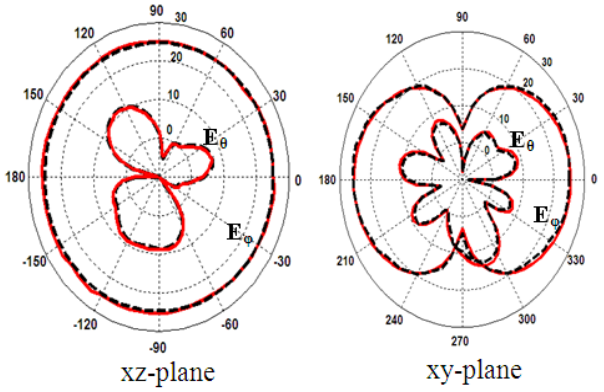

(a) f= 3.4 GHz

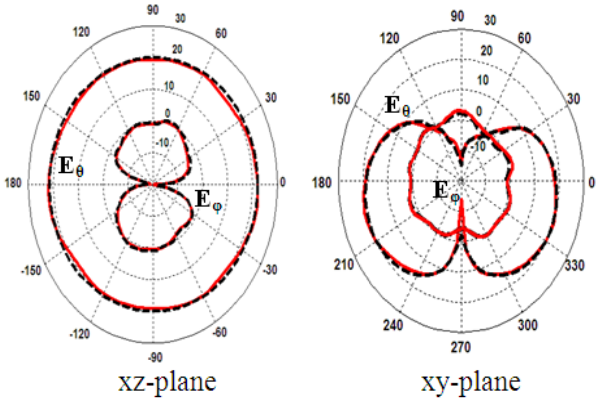

(b) f= 6.2 GHz

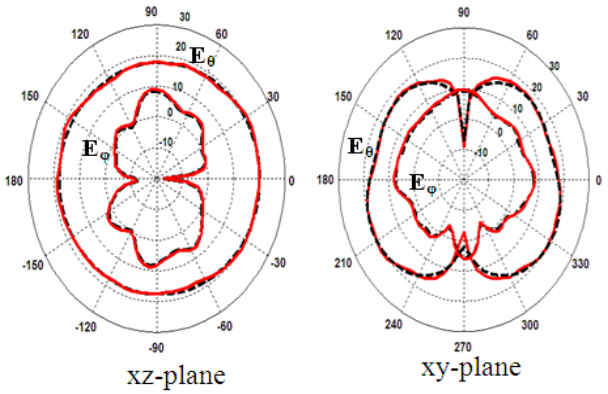

(c) f= 7.8 GHz

Fig. 6. The simulated radiation patterns of the proposed antenna A in xz and xy-planes at different frequencies.

____ FEM _ _ _ FIT

B. Antenna design B

In this proposed antenna design, the planar circular monopole antenna is inserted within only one layer of cylindrical DR with radius R_1 = 7.5 mm and thickness T = T_1+T_2 = 5.318 mm. The layer is perforated by 11 semi-holes drilled into

the dielectric material with a hole diameter of d_3 = 1.4 mm and separation between each two holes S_2 = 2.52 mm. The center of the holes located at $\left(\frac{R_1+R_2}{2}\right)$,where R_2 = 5.5 mm. Based on several parametric studies, the optimized antenna is designed as depicted in Fig. 7. Using the FEM method, the power reflection coefficientand gain of the proposed antenna are calculated as shown in Fig.8. The gain of the proposed antenna in the boresight direction varies from 3dB to 6dB over the operating UWB frequency range. Simulation results show that the impedance bandwidth is about 8.4 GHz starting from 3.2 GHz to 11.6 GHz. The simulated radiation patterns of the proposed antenna at 3.4, 6.2, and 7.8 GHz along the different planes are illustrated in Fig. 9, respectively. The simulated H-plane retains omnidirectional over the entire bandwidth. The results are compared with that calculated with FIT with a good agreement between the two techniques as shown in the figures.

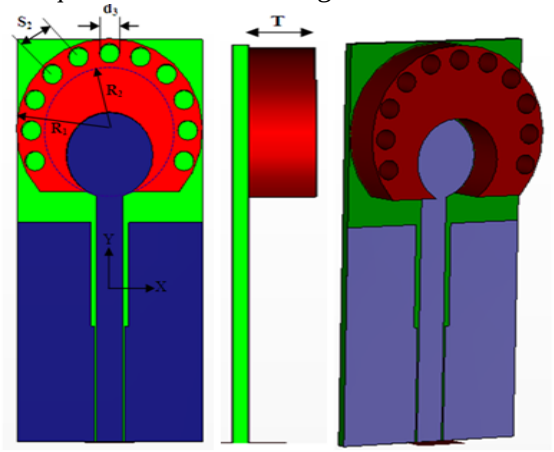

(a) Top view (b) Side view (c) Three dimensic

Fig. 7. The geometry of the proposed antenna design B.

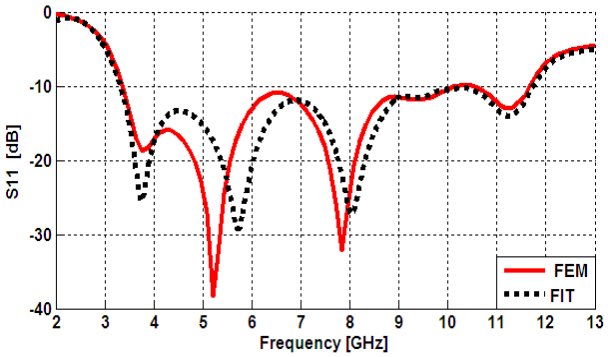

(a) Reflection coefficient frequency response.

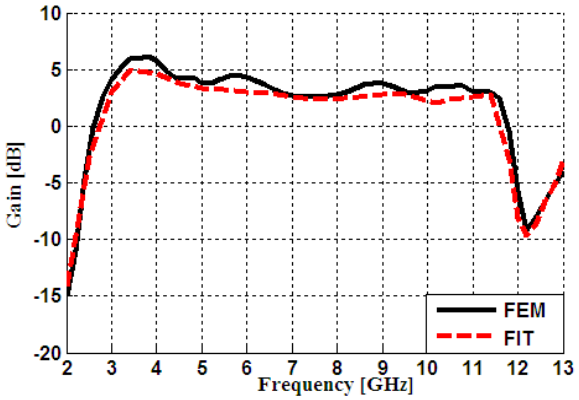

(b) Antenna gain frequency response

Fig. 8. The simulated frequency response results of proposed antenna design A using FEM and FIT.

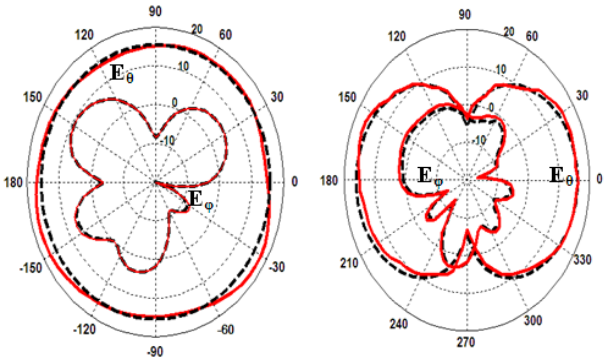

(a) f= 3.4 GHz

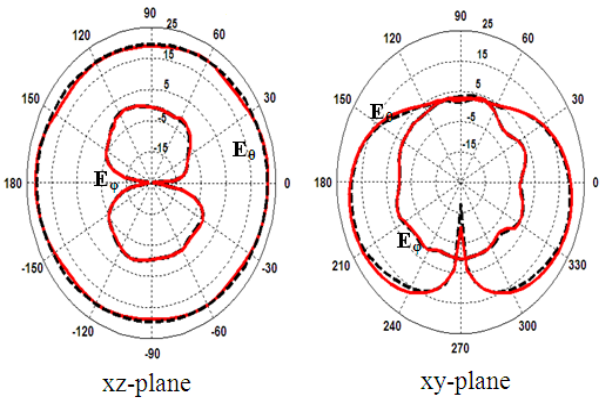

(b) f= 6.2 GHz

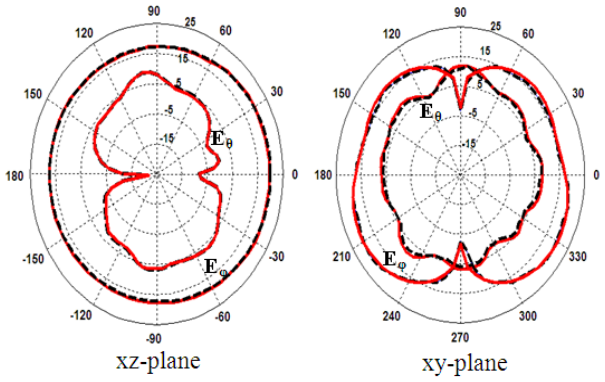

(c) f= 7.8 GHz

Fig. 9. The simulated radiation patterns of the proposed antenna B in xz and xy-planes at different frequencies.

___ FEM _ _ _ FIT

Figure 10 shows the effect of the parameters of the perforated DRA on the impedance bandwidth since the diameter of the holes is varying the bandwidth of the antenna affecting where the result effective permittivity is changing with respect to the holes diameter.

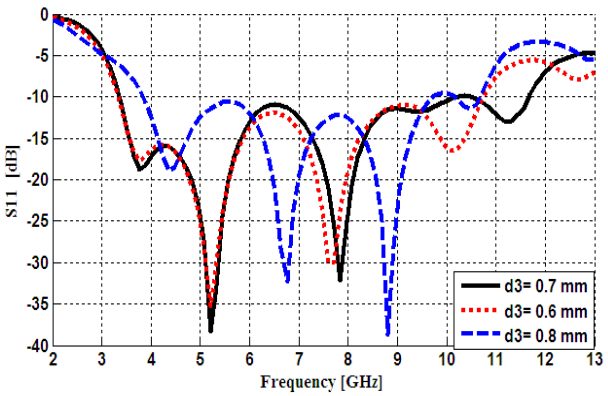

Fig. 10. The effect of the holes diameter on the antenna B bandwidth.

III. UWB ANTENNAS WITH A BAND-NOTCH STRUCTURES

In this section, the proposed antennas A and B are reconstructed to provide a stop-band notch from 5 to 6 GHz for WLAN communication system. Two U-shaped slots etched in the ground plane are used as shown in Fig. 11. The notch frequency can be adjusted by tuning the length and depth of the U-slot. The slots behave as resonant structures and are capable of preventing the energy from radiating to the free space. The dimensions of the slots are optimized to give the required stop band where the length of each slot is L_s= 8.2 mm and the width is W_s= 4 mm with thickness t = 0.5 mm with offsets d_x= 0.97 mm and d_y= 3 mm as depicted in Fig.11. It is seen that from Fig.12, the antennas in design A and design B provide sharp stop-band notch in the frequency range 5 - 6 GHz with a VSWR value of about 15 at 5.4 GHz for antenna design A and 12 at 5.5 GHz for design B by inserting the two slots. Figure 13 shows a minimum gain of -18dB at 5.4 GHz for design A while for design B the gain decreased to -15 dB at the frequency of 5.5 GHz. For other frequencies outside the notch frequency band, the antenna gain is about the same for both antennas with and without the U-slots. It is observed that the radiation patterns at other frequencies out of the notched frequency band are about the same as those of the antennas without adding the U-slots. The proposed antennas present omnidirectional patterns across the whole operating band in the H-plane an immediate sharp increase in VSWR is observed at the notch frequency band.

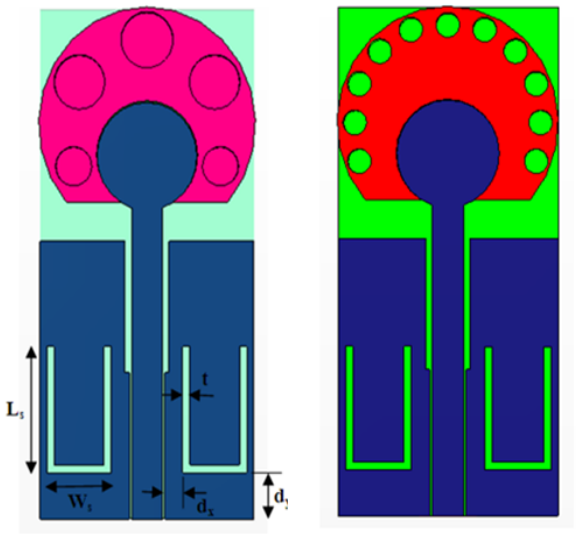

Fig. 11.The geometry of the proposed antennas A and B after adding two U-slots in the ground plane.

IV. CONCLUSIONS

In this paper, two antennas for notched-UWB applications are proposed. The antennas combine the planar circular monopole and dielectric resonator antennas. The antennas have

demonstrated good performance in terms of return loss and gain. The antenna -10dB |s11|bandwidth covers the range of 3.2 to 11.6 GHz. The two U-slots embedded in the ground plane around the CPW feeding achieved an immediate sharp increase in VSWR at the notch band from 5 to 6 GHz for WLAN. The simulated radiation patterns are quite stable within UWB frequencies; it shows good monopole-like patterns and nearly omnidirectional patterns in the horizontal plane.

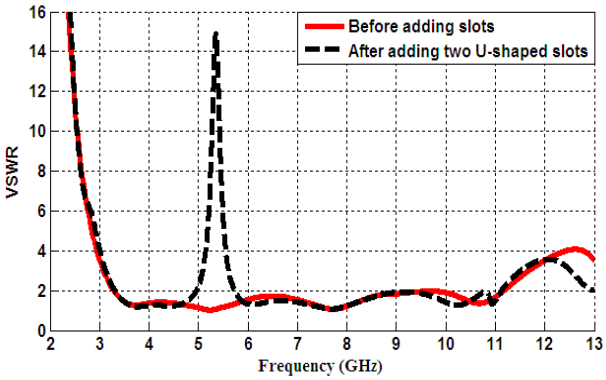

(a) Antenna design A.

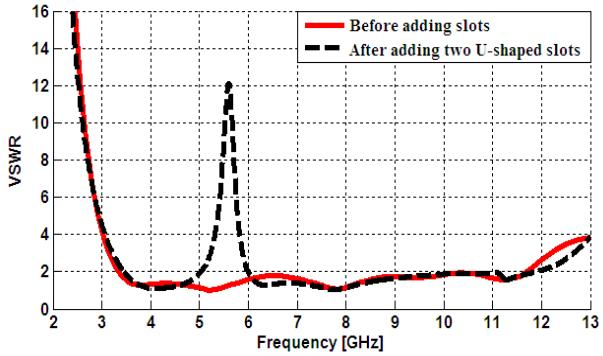

(b) Antenna design B.

Fig. 12. The simulated VSWR of proposed antennas A and B versus operating frequency before and after adding U-slots.

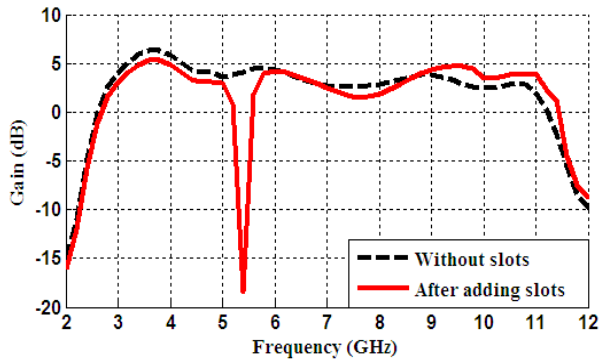

(a) Antenna design A.

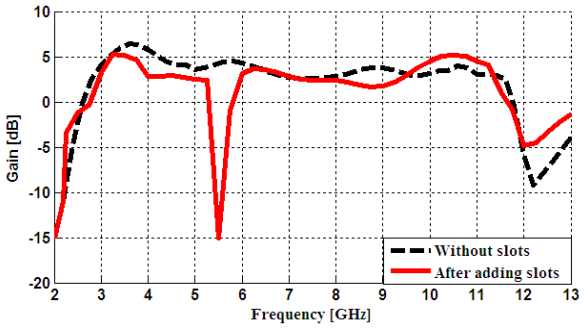

(b) Antenna design B.

Fig. 13. The simulated gain of proposed antennas A and B versus operating frequency before and after adding U-slots.

REFERENCES

[1] Federal Communications Commission, First Report and Order on Ultra-Wideband Technology, FCC 02–48, Washington, DC, April 22, 2002.

[2] B. Allen, M. Dohler, E. E. Okon, W. Q. Malik, A. K. Brown, and D. J. Edwards, "Ultra-Wideband Antennas and Propagation for Wireless Communications, Radar, and Imaging," *John Wiley &Sons*, USA, 2007.

[3] S. R. Saunders and A. A. Zavala, "Antennas and Propagation for Wireless Communications," *John Wiley & Sons*, UAS, 2007.

[4] A. M. Abbosh and M. E. Bialkowshi "Design of Ultra-Wideband Planar Monopole Antenna of Circular and Elliptical Shape," *IEEE Trans. Antennas Propag.*, vol. 56, no.1, pp. 17-23, January 2008.

[5] J. William and R. Nakkeeran,"A New UWB Slot Antenna with Rejection of Wi-Max and WLAN Bands," *Applied Computational Electromagnetics Society(ACES) Journal*, vol. 25, no. 9, September 2010.

[6] D. S. Jaran and Ghouchani, "Cross Slot Antenna with U-Shaped Tuning Stub for Ultra Wideband Applications," *Applied Computational Electromagnetics Society(ACES) Journal*, vol. 24, no.4, August 2009.

[7] G.-M. Zhang, J.-S. Hong, and B.-Z. Wang, "Two Novel Band-Notched UWB Slot Antennas FED by Micro-Strip Line," *Progress in Electromagnetics Research*, vol. 78, 209-218, 2008.

[8] A. Petosa, Dielectric Resonator Antenna Hand-Book, Artech House, Inc., Norwood, USA, 2007

[9] A. Kishk, Y. Yin, and A. W. Glisson, "Conical Dielectric Resonator Antennas forWide-Band Applications," *IEEE Trans. Antennas Propag.*, vol. 50, no. 4, pp. 469-474, August 2002.

[10]K. S. Ryu and A. Kishk, "Ultra-Wideband Dielectric Resonator Antennas," *IEEE Antennas and Propagation Society International Symposium (APS/URSI)*, Toronto, ON. Canada, July 2010.

[11]O. Ahmed, A. R. Sebak, and T. A. Denidni, "Size Reduction and Band-Width Enhance-ement of a UWB Hybrid Dielectric Resonator Antenna for Short-Range Wireless Communicateons," *Progress In Electromagnetics Research Letters*, vol. 19, pp. 19-30, 2010.

[12]K. S. Ryu and A. Kishk, "UWB Dielectric Resonator Antenna Having Consistent Omni-directional Pattern and Low Cross-Polarization," *IEEE Trans. Antennas Propag*., vol. 59, no.4, pp. 1403-1408, April 2011.

[13]M. N. Jazi and T. A. Denidni,"Ultra-Wideband Dielectric Resonator Antenna with Band Rejection," *IEEE Antennas and Propagation Society International Symposium (APS/URSI)*, Toronto, ON, Canada, July 2010.

[14]X. Dong and T. An, "A New FEM Approach for Open Boundary Laplace's Problem," *IEEE Transactions on Microwave Theory and Techniques*, vol. 44, no. 1, pp. 157-160, January 1996.

[15]A. Mitchell, D. M. Kokotoff, and M. W. Austin, "Improvement to the PML Boundary Condition in the FEM using Mesh Compression," *IEEE Transactions on Microwave Theory and Techniques*, vol. 50, no. 5, pp. 1297-1302, May 2002.

[16]R. Marklein, The Finite Integration Techniques as a General Tool to ComputeAcoustic, Electromagnetic, Elastodynamic, and Coupled Wave Fields, IEEE press, New York, USA, 2002.

[17]A. Petosa, S. Thirakoune, and A. Ittipiboon, "Array of Perforated Dielectric Resonator Antennas," *IEEE Antennas and Propagation Society International Symposium (APS/-URSI)*, Monterey, CA, USA, pp. 1106-1109, June 2004.

S. H. Zauind-Deen (S'81-M'88) was born in Menouf, Egypt, on November 15, 1955. He received the B.Sc. and M.Sc. degrees from Menoufia University in 1973 and 1982 respectively, and the Ph.D. degree in Antenna Engineering from Menoufia University, Egypt in 1988.He is currently a professor in the Department of Electrical And Electronic Engineering in the Faculty of Electronic Engineering, Menoufia University, Egypt. His research interests at present include microtrip and leaky wave antennas, DRA, RFID, UWB, and optimization techniques.

Ahmed Shaker was born in Cairo, Egypt, on February 10, 1976. He received the B.Sc. and M.Sc. degrees from Helwan University in 1999 and 2006 respectively. He is currently working for his Ph.D. in Antenna Engineering from Helwan University, Egypt. He is currently an assistance lecture in the Department of Electronics and Communications Engineering in the Faculty of Engineering, Helwan University, Egypt. His research interests at present include UWB antennas, and DRA.

Korany R. Mahmoud was born in Cairo, Egypt, on August 1975. He received his B.S. and M.S. degrees in Communications and Electronics Engineering from Helwan University in 1998 and 2003. His Ph.D. degree from Helwan University in collaboration with the University of Connecticut, USA in 2008. He is currently an assistant professor at the department of communications and electronics engineering in the same faculty. Dr. Mahmoud has served as an Editor/Reviewer of Int. J. RF & Microwave CAE. His current research interests include the areas of antenna design, array beamforming using optimization techniques.

Reducing the Numerical Calculation in the Wave Iterative Method by Image Processing Techniques

H. Hrizi and N. Sboui
Electronics Laboratory, Department of Physics, Faculty of Sciences in Tunis, 2092 Manar Tunisia
noureddine.sboui@fst.rnu.tn

Abstract ─ The wave iterative method is a numerical method used to model electromagnetic circuits. It is based on the concept of waves in the place of electromagnetic fields. To study the electronic circuits having complex structures, this method requires much time. We propose in this article to improve this method by using techniques of image processing. That's why the structure of the studied circuit is considered as an image. The objective is to reduce computing time by reducing dimensions of the calculation matrices. The reduced matrices are built containing only the important part of the information. Our goal is to prove that the most important zones in the structure are located in the contour with small steps in the vicinity of the contour.

Keywords ─ Image processing techniques, reducing calculation matrices, reducing computing time, WCIP method, R-WCIP method.

I. INTRODUCTION

The wave concept iterative process (WCIP) method is a numerical method [1-8] used to ensure electromagnetic modeling of high frequency (HF) electronic circuits. This method is characterized by its stability and its convergence towards good results. In the case of complex structures, this method is also stable but it takes much time to converge to the optimal result. A big number of iterations are necessary to model complex structures requiring a fine mesh. We have a problem of numerical complexity because the number of cells describing the circuit is important. That's why the WCIP method takes much time to give reach the convergence to the optimal values. In order to improve performances of this method, techniques of image processing are used. Thus, a rapid convergence to the optimal result is ensured. Our study is based on the principle of image segmentation [9-14], especially the contour detection technique [15-18]. We choose this technique in order to focus on the important information part of the studied structure. The contour represents the place of the important points in the electronic structure because the values of the electromagnetic fields are important on contours and they are weak elsewhere. The contour of a digital image corresponds to a brutal change of the luminous intensity and the image properties. The important values of the electromagnetic fields are in the zones of the structure discontinuity between metal and dielectric in the structure. To locate these zones of interest, we have resort to a method based on contour detection. We focus on the important information while the rest will be neglected. Thus, we build new calculation matrices containing only the useful information. So the new matrices have reduced sizes compared to the original matrices in the classical WCIP method. The calculation time is reduced because we calculate on these reduced matrices that's why a large gain in computing time is realized and the improved method is noted Reduced-WCIP (R-WCIP).

II. THEORETICAL STUDY

A. Outline on the wave iterative method

The WCIP method is an integral method used in the electromagnetic modeling of HF electronic circuits. The wave iterative method is developed in detail in [1-8]. It is called WCIPbecause it is based on waves instead of electromagnetic fields and it establishes a recurrent relation between incident and reflected waves. The iterative method is used to study a frequency selective surface (FSS) having a complex structure represented in Fig. 1.

Submitted On: Aug. 3, 2011
Accepted On: April 25, 2012

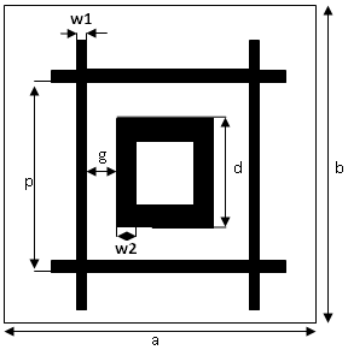

Fig. 1. Unit cell of a FSS structure.

The height of the substrate is h= 3mm and its permittivity εr=3.8, a=b=30mm, p = 28 mm, G = 2.8 mm, D = 22.2 mm, w1 = 0, 2 mm, and w2 = 3.4 mm, the total structure is synthesized using a grid of 150x150 pixels.

The amplitudes of the incidental and reflected waves are expressed in function of electromagnetic fields by the following relations:

$$\begin{vmatrix} A_i \\ B_i \end{vmatrix} = \begin{bmatrix} \dfrac{1}{2\sqrt{Z_{0i}}} & \dfrac{\sqrt{Z_{0i}}}{2} \\ \dfrac{1}{2\sqrt{Z_{0i}}} & -\dfrac{\sqrt{Z_{0i}}}{2} \end{bmatrix} \begin{vmatrix} E_i \\ J_i \end{vmatrix}. \qquad (1)$$

A_i and B_i are respectively the incidental and reflected waves in the plan P_i, "i" is an indication of medium (i=1, 2), Z_{0i} indicates the wave impedance of the medium. The iterative process consists in establishing a recurrent relation between incident and reflected waves in two different domains as indicated in the following equations:

$$\begin{cases} \vec{B} = \hat{\Gamma}_{\Omega} \vec{A} + \vec{B}_0 \\ \vec{A} = \hat{\Gamma} \vec{B} \end{cases}. \qquad (2)$$

Two operators are defined: one is in the space domain and the other one is in the spectral domain. The fast Fourier mode transformation (FMT) and the reverse transformation (FMT^{-1}) ensure the transition from one domain to another. In general, the algorithm of the iterative process is summarized in Fig. 2 with $\alpha = TE \text{ or } TM$.

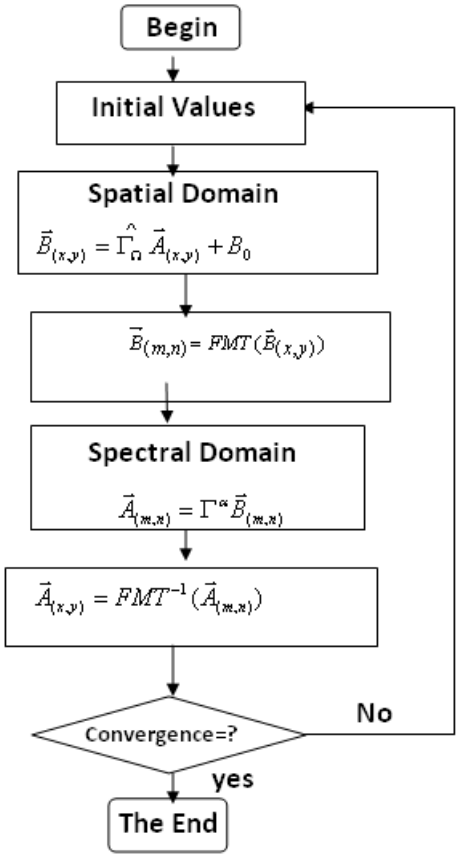

Fig. 2. Algorithm of the WCIP method.

B. Image processing technique

The image processing technique used in this work is the technique of segmentation [9-14]. It consists in cutting out an image in related areas presenting homogeneity according to a certain criterion, such as the color. The union of these areas must give again the initial image. The segmentation technique allows the extraction of qualitative information in the image. The image segmentation is based on the technique of contour detection which defines the borders between distinct homogeneous zones. It is characterized by the fact that they take into account only information on the contour of the objects. This technique detects all the image contours. The algorithms of contour detection are characterized by the use of derivations operators, the gradient or the Laplacian, from which we respectively seek for the maxima or the passage by zero. In general, the variation of intensity in an image corresponds to relevant zones that contain important information. It ensures the extraction of the useful part in the image. This information corresponds to

borders of homogeneous areas. The contour detection [15-18] is a preliminary stage to many applications of image analysis. Contours constitute rich indices, as well as the points of interests, for any later interpretation of the image. They correspond to discontinuities of the intensity function. For that, the first derivative of the image intensity function is studied in order to define local maxima of the intensity gradient function and passages by zero of the Laplacian. That's why the contour is the place of maximum first derivative and the crossing points by zeros of the second derivative for the intensity function. The difficulty consists in the presence of noise in the image that's why the derivative calculation requires an image pre-filtering. In a continuous image $f(x, y)$, a contour appears as a line where the very strong variations of $f(x, y)$ are localized. We consider $\vec{G}$ the gradient of $f(x, y)$, the module of $\vec{G}$ is defined in the following relation:

$$G = \left[\left(\frac{\partial f}{\partial x}\right)^2 + \left(\frac{\partial f}{\partial y}\right)^2 \right]^{\frac{1}{2}}. \quad (3)$$

The direction of the gradient is defined by:

$$\vec{g} = \frac{\vec{G}}{G}. \quad (4)$$

The contour is the place of the maximum of the gradient G in the direction $\vec{g}$, a point of contour is defined by:

$$\frac{\partial G}{\partial g} = 0. \quad (5)$$

The second derivative of $f(x, y)$ in the direction $\vec{g}$ gives that:

$$\frac{\partial G}{\partial g} = \frac{\partial^2 f}{\partial g^2} = 0. \quad (6)$$

Finally, the passage by 0 of the Laplacian is obtained and it is given by:

$$\Delta f = 0 \approx \frac{\partial^2 f}{\partial g^2} = 0. \quad (7)$$

This property is used in the approaches known as contour detectors by passage by zero of the Laplacian. Thus, we conclude that it exists a great number of methods of contour detection in an image. The majority of them can be gathered in two categories. The first category seeks the extremum of the first derivative of the intensity function especially the local maxima of the gradient intensity. The second method seeks the cancellations of the second derivative which means the passage by zero of the Laplacian or the resolution of a non-linear differential expression. In order to guarantee the double derivation, the image is at least pretreated by convolution with a function twice derivable. For this reason, we use the Gaussian function. The approach used in our study is based on the method of "Canny" which has a very good quality of contour detection [15].

C. Reducing matrices by the new algorithm

The important zones of the studied structure are located in the vicinity of contours and they are defined by the technique of contour detection. The useful information is extracted from the original matrix "MxN", then reduced matrix "Mr x Nr"is built having smaller sizes as in Fig. 3 so that a big part of calculation matrices is neglected.

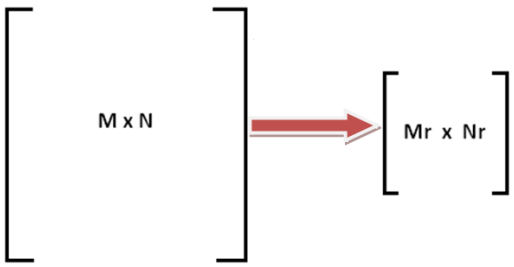

Fig. 3. Reducing the dimensions of the original matrices towards reduced matrices.

In the new proposed algorithm, the calculation is carried out on the reduced matrices " *Ar* " and " *Br* " which represent the incidental and reflected waves as shown in Fig. 4.

The new process starts with the classical WCIP algorithm which calculates a certain number of iterations (Nmin) applied on original matrices having basic sizes "MxN". After that, the dimensions of the original matrices are reduced using the algorithm of contour detection. The WCIP algorithm is applied to continue the remaining iterations but in this case we operate on the matrices having reduced sizes "Mr x Nr" until reaching the convergence after "Nmax" iterations. Finally, original matrices are rebuilt. Thus, this new approach is called Reduced WCIP (R-WCIP)

since we apply a mechanism of reduction of matrices dimensions by the technique of contour detection. The R-WCIP algorithm operates first on original matrices then on reduced matrices in order to reduce the computing time and to obtain a good result in a minimum of time as in Fig. 5.

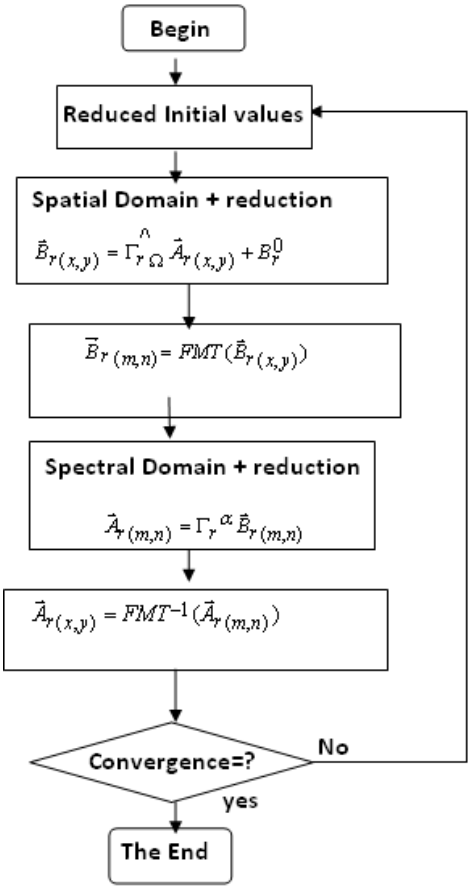

Fig. 4. The reduced WCIP algorithm.

III. SIMULATION RESULTS

A. Reduction ratio in the calculation matrices

The contour of the basic studied structure is represented in Fig. 6. The technique of contour detection specifies the zones where the electromagnetic field values are important. In an image in gray levels, a contour is characterized by a brutal change of the intensity values. The goal is to transform this image into another in which contours appear by convention in white on black bottom. Thus, we consider only the contour because it contains the useful information and the remaining zones are neglected.

The zones that are close to contour are called the vicinity of contour. For more precision, the vicinity is detected with different steps (a step of 1 pixel in Fig. 7 and a step of 3 pixels in Fig. 8).

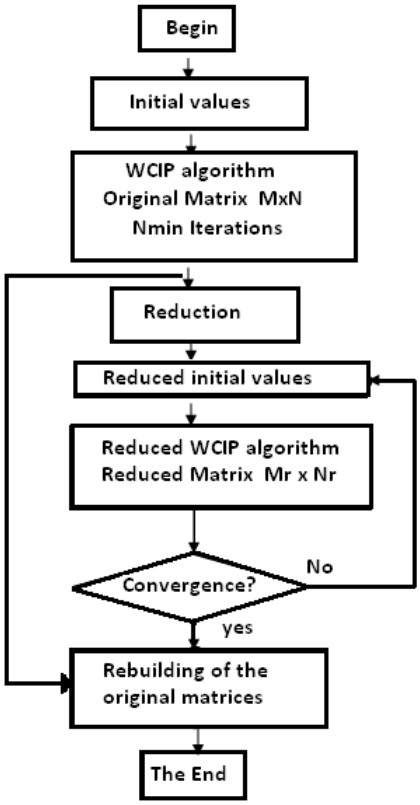

Fig. 5. The new proposed algorithm R-WCIP.

Our goal is to prove that the most important part in the structure is in the contour with small step in the vicinity of the contour. From the original matrix that its dimensions are equal to 150x150 pixels, a reduced matrix is formed containing only useful information represented in white in the image of the contour vicinity detection. What is represented in black is neglected because it contains information that is not important. In the case of one step in the contour vicinity, a reduction ratio around 76% is realized as described in the following:

- Discretization 150x150 pixels
- Original matrix 150x150 pixel
- Reduced matrix 72x72 pixels
- Reduction ratio = 76%

In the case of three steps in the contour vicinity of the structure, the reduction ratio is around 59% as described in the following:

- Discretization 150x150 pixels
- Original matrix 150x150 pixel

- Reduced matrix 96x96 pixels
- Reduction ratio = 59%

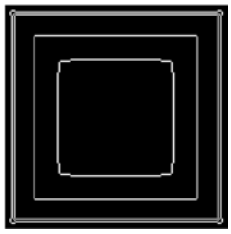

Fig. 6. Contour detection in the basic structure.

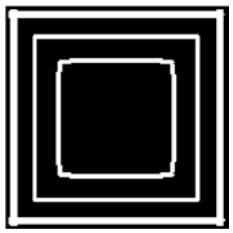

Fig. 7. Detection of contour vicinity (Step =1).

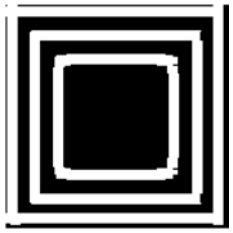

Fig. 8. Detection of contour vicinity (Step =3).

B. Variation of S_{11} and S_{21} calculated by the new method in function of frequency

In Figs. 9-12, the variation of the coefficients S_{11} and S_{21} is represented in function of frequency. These coefficients are calculated by our new R-WCIP method. These results are compared with those calculated by the classical WCIP method in order to prove that our results are closed to the best and optimal results. The maximum number of iterations calculated by the two methods is equal to 200 iterations (Nmax=200). In the new R-WCIP method, two values of "Nmin" are tested (25 and 50 iterations). Good results are obtained in comparison with the WCIP method. Thus, in our new R-WCIP method, the WCIP algorithm is used to calculate only 25 or 50 iterations on the basic matrices that have big dimensions and the following iterations are calculated on reduced matrices that have small dimensions until achieving 200 iterations. That's why the new approach takes less time of calculation. However, in the classical WCIP method, the WCIP algorithm calculates all the 200 iterations on big matrices. Thus, our principal goal which is the reduction of calculation matrices is achieved so that the computing time is reduced. Finally, we have a fast convergence to the optimal result with minimum average error. Thus, good results are obtained by the new R-WCIP method with a best reduction in computing time.

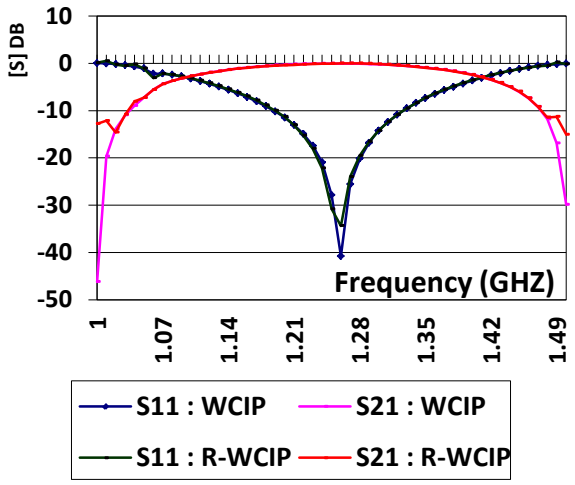

Fig. 9. Parameter "S" in function of frequency, 50 basic iterations before reducing the dimensions of the matrices, Nmax=200 iterations, contour vicinity with step=1.

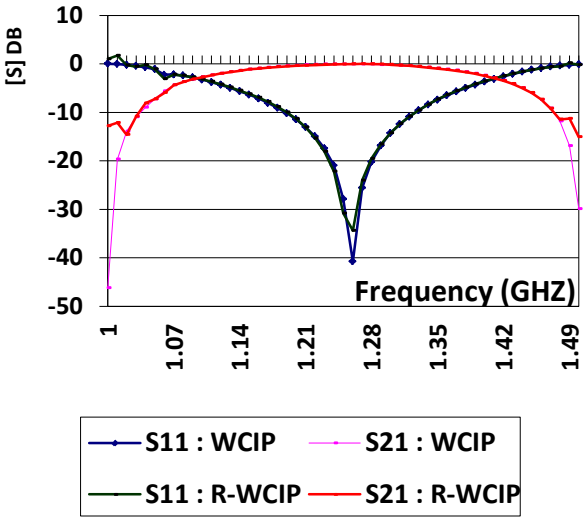

Fig. 10. Parameter "S" in function of frequency, 50 basic iterations before reducing the matrices dimensions, Nmax=200 iterations, contour vicinity with step=3.

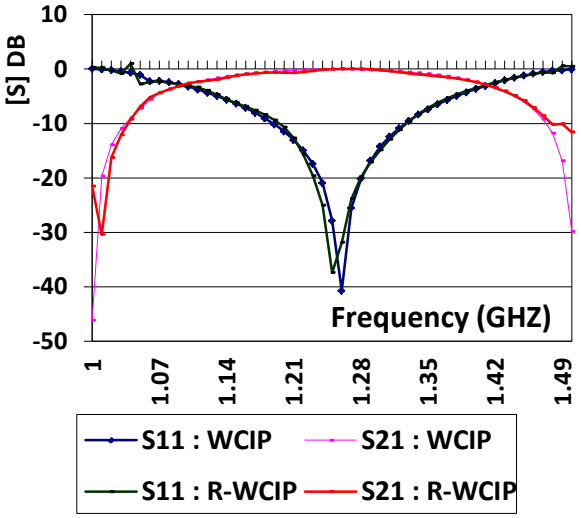

Fig. 11. Parameter "S" in function of frequency, 25 basic iterations before reducing the dimensions of the matrices, Nmax=200 iterations, contour vicinity with step=1.

From the last results, we conclude that the new R-WCIP method provides good results either in the case of one step or three steps in the contour vicinity. This proves that one step near the contour is sufficient to give good results which means that the important information part is located on the contour and not far from the contour. Also, we notice that the number of iterations applied on basic matrices before reducing the dimensions of matrices is 25 or 50 and the remaining iterations are calculated on reduced matrices. Thus, a big gain in computing time is realized and good results are found with the new R-WCIP method.

C. Gain in computing time

In the next paragraph, the classical WCIP method is used to calculate a maximum number of iterations (Nmax). To make a comparison between the two methods, the new R-WCIP method calculates the same number of iterations (Nmax) with two values of Nmin (25 and 50). In Table 1 and Table 2, we observe an important gain in convergence time when calculating S_{11} and S_{21} values after Nmax iterations by the two methods. This gain of time is provided by the new R-WCIP method because we add an algorithm of matrices reduction based on contour detection. The mesh used in this structure is 256x256 cells. The used machine has a microprocessor Intel(R) Pentium(R) Dual Core CPU 2x2.16GHz and 3GB of RAM. So we notice that the R-WCIP method is more rapid than the classical WCIP method.

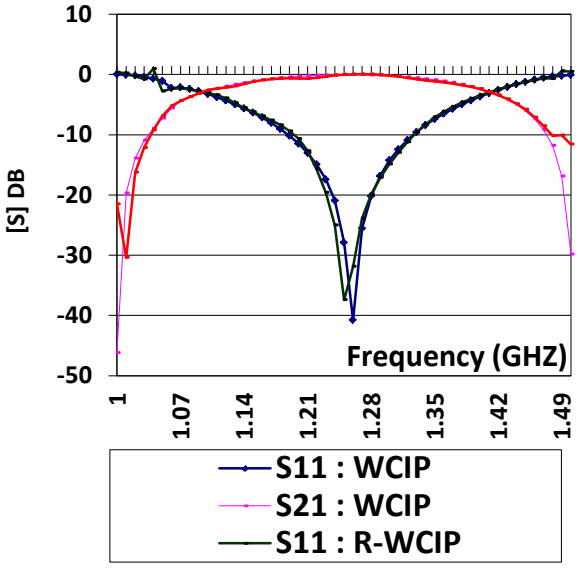

Fig. 12. Parameter "S" in function of frequency, 25 basic iterations before reducing the matrices dimensions, Nmax=200 iterations, contour vicinity with step=3.

Table 1: Gain in computing time given by "R-WCIP", Fr=11GHZ, Grid 150 x 150 pixels, (Nmax=1000 iterations)

Nmin	WCIP (Nmax=1000) Time (s)	"R-WCIP" (Nmax=1000) Time (s)	Gain (%)
25	86	19	77%
50	86	24	72%

Table 2: Gain in computing time given by "R-WCIP", Fr=11GHZ, Grid 150 x 150 pixels, (Nmax=200 iterations)

Nmin	WCIP (Nmax=200) Time (s)	"R-WCIP" (Nmax=200) Time (s)	Gain (%)
25	17	5.9060	65%
50	17	7.5320	55%

D. Comparison in terms of the average error

In Table 3, we represent the values of the average error calculated on the transmission coefficients S_{21}. The band of frequency is from 10GHz to 15GHz. The error is calculated when using the new R-WCIP method in comparison with the classical WCIP method. Two different values of "Nmin" are chosen (25 and 50). The number "Nmin" represents the minimum number of iterations calculated by the classical WCIP algorithm before the reduction of the matrices dimensions in the new R-WCIP method. Then, the remaining iterations are carried out after the mechanism of reduction until the convergence with “Nmax” iterations. The maximum number of iterations “Nmax” is equal to 200 iterations. The average error in comparison with the classical WCIP method is limited. This proves the effectiveness and robustness of our new approach. Finally, we notice that the convergence to the good result very close to the desired value with a minimum average error in each frequency. Thus, the new R-WCIP method gives good results with minimum error.

Table 3: Comparison between WCIP and «R-WCIP» in terms of the average error (S_{21}), band of frequency from10GHZ to 15GHZ, (Nmax=200 iterations)

Nmin	Error(DB)
25	0.6077
50	0.6064

IV. CONCLUSION

In our research work, the wave iterative method has been improved especially when modeling complex structures. Image processing techniques have been used to reduce the dimensions of calculation matrices and to focus on zones in the contour vicinity where the electromagnetic fields are important. The new R-WCIP method operates on reduced matrices so that the computing time is reduced. Finally, a fast convergence to the optimal result is realized in spite of the complex structures of the studied electronic circuits.

REFERENCES

[1] N. Sboui, A. Gharsallah, H. Baudrand, A. Gharbi, ‘‘Global Modeling of Microwave Active Circuits by an efficient iterative procedure”, *IEE Proc-Microw. Antenna Propag.*, vol. 148, no. 3, June 2001.

[2] N. Sboui, A. Gharsallah, H. Baudrand, A. Gharbi, ‘‘Design and Modeling of RF MEMS Switch by Reducing the Number of Interfaces’’, *Microw. and Opt. Technol. Lett*, vol. 49, no. 5, pp, 1166-1170, May 2007.

[3] N. Sboui, L. Latrach, A. Gharsallah, H. Baudrand, A. Gharbi, “A 2D Design and Modeling of Micro strip Structures on Inhomogeneous Substrate”, *Int. Journal of RF and Microwave Computer Aided Engineering*, vol. 19, no. 3, pp. 346-353, May 2009.

[4] N. Sboui, A. Gharsallah, H. Baudrand, A. Gharbi, “Global Modeling of Periodic Coplanar Waveguide Structure for Filter Applications Using an Efficient Iterative Procedure”, *Microwave and Opt. Technol. Lett*, vol. 43, no. 2, pp. 157-160, 2004.

[5] N. Sboui, A. Gharsallah, A. Gharbi, and H. Baudrand, “Analysis of Double Loop Meander Line by using Iterative Process”, *Microw. Optical Technical Letters*, vol. 26, pp. 396-399, June 2000.

[6] J. Selmi, R. Bedira, A. Gharsallah, A. Gharbi, H. Baudrand, “Iterative Solution of Electromagnetic Scattering by Arbitrary Shaped Cylinders,” *Applied Computational Electromagnetic Society (ACES) Journal*, vol. 25, no. 7, pp. 639 - 646, July 2010.

[7] L. Latrach, N. Sboui, A. Gharsallah, H. Baudrand, A. Gharbi, “Analysis and Design of Planar Multilayered FSS with Arbitrary Incidence”, *Applied Computational Electromagnetic Society (ACES) Journal*, vol. 23, no. 2, pp. 149-154, June 2008.

[8] H. Baudrand, N. Raveu, N. Sboui, G. Fontgalland, “Applications of Multiscale Waves Concept Iterative Procedure”, *Inter. Microw. And Opto. Conference*, Salvador, BA, Brazil, October 29-November 2007.

[9] A. Herbulot, S. Jehan-Besson, S. Du_ner, M. Barlaud, G. Aubert, “Segmentation of Vectorial Image Features using Shape Gradients and Information Measures”, *Journal of Mathematical Imaging and Vision*, vol. 25, iss. 3, pp. 365-386, October 2006.

[10] C. Vazquez, A. Mitiche, R. Laganiere, “Joint Multiregion Segmentation and Parametric Estimation of Image Motion by Basis Function Representation and Level Set Evolution”, *IEEE Transactions on*

Pattern Analysis and Machine Intelligence, vol. 28, iss. 5, pp. 782-793, 2006.

[11] A. Herbulot, S. Jehan-Besson, S. Duffner, M. Barlaud, et G. Au- bert, "Segmentation of Vectorial Image Features using Shape Gradients and Information Measures", *Journal of Mathematical Imaging and Vision*, vol. 25, iss. 3, pp. 365-386, October 2006.

[12] F. Precioso, M. Barlaud, T. Blu, et M. Unser, "Robust Real-Time Segmentation of Images and Videos Using a Smooth-Spline Snake-Based Algorithm", *IEEE Transactions on Image Processing*, vol. 14, iss. 7, pp. 910-924, July 2005.

[13] A. Herbulot, S. Boltz, E. Debreuve, M. Barlaud. "Robust Motion-Based Segmentation in Video Sequences using Entropy Estimator", *International Conference on Image Processing*, pp. 1853-1856, Atlanta, USA, October 2006.

[14] R. Araneo, S. Barmada, "Advanced Image Processing Techniques for the Discrimination of Buried Objects," *Applied Computational Electromagnetic Society (ACES Journal)*, vol. 26, no. 5, pp. 437-446, May 2011.

[15] J. Canny, "A Computational Approach to Edge Detection", *IEEE Transactions on Pattern Analysis and Machine Intelligence*, vol. 8, no. 6, pp. 679-714, 1986.

[16] M. Gastaud, et M. Barlaud, "Video Segmentation Using Active Contours on a Group of Pictures", *IEEE International Conference on Image Processing*, vol. 2, pp. 81-84, Rochester, N.Y, September 2002.

[17] M. Rochery, I. H. Jermyn, J. Zerubia, "Higher Order Active Contours", *International Journal of Computer Vision*, vol. 69, pp. 27-42, 2006.

[18] E. Debreuve, M. Barlaud, G. Aubert, J. Darcourt, "Space Time Segmentation using Level Set Active Contours Applied to Myocardial Gated SPECT", *IEEE Transactions on Medical Imaging*, vol. 20, iss. 7, pp. 643-659, July 2001.

Characterization of Packet-Level Measurements for Vehicular Wireless Networks

Yuhao Wang, Xing Xing, and Yan Zhang

School of Information Engineering
Nanchang University, 330031, China
wangyuhao@ncu.edu.cn

Abstract ─ A comprehensive understanding of the fading effect on vehicular communications is essential for reliable intelligent transportation system (ITS). Dozens of experiments were performed in the real urban area to collect various types of vehicular wireless data measurements. Then a simulation model of radio link between double mobile nodes was proposed. Based on the real measured data, the proposed model, and the existing model are all applied to the simulator for comparison. It is shown that by evaluating the packet level performance for double mobile vehicles in an urban area, the proposed model performed better. Significant realism can be added to existing systems with clear implications on the design of upper layer protocols by modeling the fading characters for vehicular communications.

Index Terms ─ Communication performance, measurements, radio channel, radio propagation, vehicular wireless networks.

I. INTRODUCTION

Vehicular wireless networks, as the key part of the intelligent transportation system (ITS), which can achieve traffic warning [1-3] and provide the driver with specific route dependent information, will be widely used in the future. Furthermore, from [4-7], the increasing demand for mobile computing and quality of service (QoS) will have future vehicles equipped with a high data rate access to the internet. Various multimedia applications, such as video on demand, games, email, etc., will also be available. Due to the dynamics of high-speed mobile vehicles and the variety of the road conditions, it is difficult to build a complete analytical model to study the network performance, and from [8-9], experimental measurement becomes important in characterizing the channel fading effect in such a dynamic vehicular communication environment. An important factor of vehicular channel model is the mobility [10-12] by including the mobility of nodes and the channel variability. Channel variability, is not well modeled in today's wireless vehicle networks. In [13], simplistic models may not be practical and it is also different to draw conclusions on the real performance of the upper layers. Designers require statistical models that can accurately capture the characteristic of propagation behavior observed at both mobile vehicles [14].

Currently, free space and two ray ground channel models are the most popular propagation models for simulation in vehicular wireless networks [15]. For the free space channel model, it describes an ideal propagation characteristic, and the received power depends on the transmitted power, the gain of antenna, and the distance of the transmitter-receiver. While for the two way ground model, it assumes that the received signal is the sum of the direct line of sight path and the reflected path from the ground. However, the model does not take obstacles into consideration. It is also too ideal for short transmitter-receiver separation distances, as it assumes that signals have a perfect 250m radius range. On the other hand, QualNet supports open-space propagation as well as stochastic propagation models such as Rayleigh, Rician, and log-normal fading, in which all models describe the time-correlation of the received signal power. The Rayleigh model considers indirect paths between the transmitter and the receiver, while the Rician model considers when there is one dominant path and multiple

Submitted On: Sept. 9, 2011
Accepted On: March 4, 2012

indirect signals. OPNet supports open-space propagation models as well as an enhanced open-space model that accounts for hills, foliage, and atmospheric affects [16]. Furthermore, obstacle effects are combined in [17, 18, 19], but the propagation characteristic is limited to line-of-sight. In [20], a radio planning tool is applied and the evaluation for the impact of a more realistic propagation by a set of measurements is validated.

In a dense urban area, path loss, shadow fading, and short-term variants are the main factors affecting the communication quality. Path loss and shadow fading determines the effective communication distance between two adjacent vehicles, while multi-path and Doppler spectrum caused by the sum of absolute speeds of individual nodes affect the quality of service (QoS) in inter-vehicle networks. However, it is noted that some of these effects can be avoided, such as by increasing the height of the antenna and the inerratic variations is just relative to the distance between transmitter and receiver. Here, the model is focused on the short-term variants, especially for the Doppler spectrum model caused by both high mobile vehicles. The Doppler spectrum models in [21, 22] for wireless cellular network cannot really be used for link between double mobile nodes. Akki and Haber [23] consider a Doppler spectrum model for radio link between double mobile nodes in a two-dimensional (2-D) uniform scattering environment. It is a deterministic channel model without considering the specific characteristics, such as the effect of antenna and dynamic distribution of received multi-path wave.

This paper addresses a fast fading channel model for radio link between double mobile nodes in a three-dimensional (3-D) scenario (3-D scatter fading channel model). It is a stochastic model relative to the antenna, the probability distribution of the multi-path wave and the relative speed of the two mobile nodes [24]. The random phase of received wave is assumed to be uncorrelated. The necessity of the proposed method is demonstrated by using real-life experiments conducted in an urban area of Wuhan city, China. The experiment involves two cars, one for transmitter and one for receiver, driving on different time and road conditions in the Wuhan city to create a broaden wireless measurement database. We obtain the analytical expressions of the Doppler spectrum for double mobile nodes, and then integrate the Doppler spectrum model with a path loss model as the physical module in OMNet++ platform to evaluate packet level performance for the link of vehicular wireless networks. The real-life vehicular wireless measurement is used to validate the proposed channel model and the results are compared with that of the conventional two ray ground model.

The rest of the paper is organized as follows. Section 2 describes the experiment and the measured wireless data. The packet-level statistical performance of the measurement is also given. Section 3 describes the proposed channel model by analytic expression of Doppler spectrum for radio link between double mobile nodes in 3-D scenario. Section 4 analyzes the packet level statistical performance of the proposed model, and compares the performance with the Gans Doppler model. Results and conclusions are given in Sections 5 and 6, respectively.

II. EXPERIMENTS AND MEASUREMENTS

The experiments were performed on LuoYu and ZhongNan roads, Wuhan city, China. There were two mobile vehicles used in the experiments as a transmitter (TX Vehicle) and a receiver (RX Vehicle), respectively. Both vehicles contain embedded-PCs (EPC) built with a Mini-ITX board, an automotive power supply, a Celeron processor, storage devices and GPS devices. The used parameters of vehicular wireless experiment network are given in Table 1.

Table 1: The parameters of Vehicular Wireless Network in measurements

Parameters	**Detailed information**
The high of antenna	3.2 m
Antenna type	Omni-direction
The gain of antenna	8 dBi
Wireless LAN chip	Intel@2200BG
Network adaper power	100 mW
Network model	Ad Hoc
Modulation	BPSK
MAC protocol	802.11b
Transmission Platform	StarEast

The transmitter broadcasted 100 User Datagram Protocol (UDP) packets per second with 100 bits per packet at 1 Mbps (the lowest rate). The UDP payload consists of a 32-bit sequence number that is incremented by the transmitter for every successive packet and local GPS record. The receiver sniffs the packets from the wireless interface and keeps a trace of the lost ones by checking the UDP packet sequence numbers, as shown in Fig. 1(a) and Fig. 1(b). We adopted packet loss rate (PLR) which is the ratio of the missing number packets in radio link to the total number packet sent by the TX vehicle as the indicator.

(a) Vehicle in the experiments

(b) PC in the vehicle

Fig. 1. Experimental vehicular system.

Dozens of measurements were obtained from real road tests. In Fig. 2 is plotted the cumulative density functions (CDF) of PLR when the distance between two vehicles varies from 10-20 meters, 20-30 meters, and 30-40 meters, respectively. From these figures, it is observed that: a) The inter-vehicle distance has an direct impact on link quality of vehicular wireless network. The distribution of PLRs become flatter as the inter-vehicle distance becomes larger. b) The PLRs with the same inter-vehicle distance almost follow the same distribution, no matter if the traffic is heavy (8 am), or light (2 pm and 9 pm). From the measurements, it is observed that we can use the same distribution function to express the different packet loss samples for the same inter-vehicle distance.

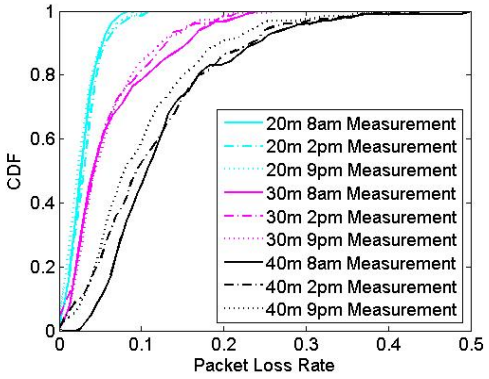

Fig. 2. The CDF of PLR for different inter-vehicle distances and different measured time

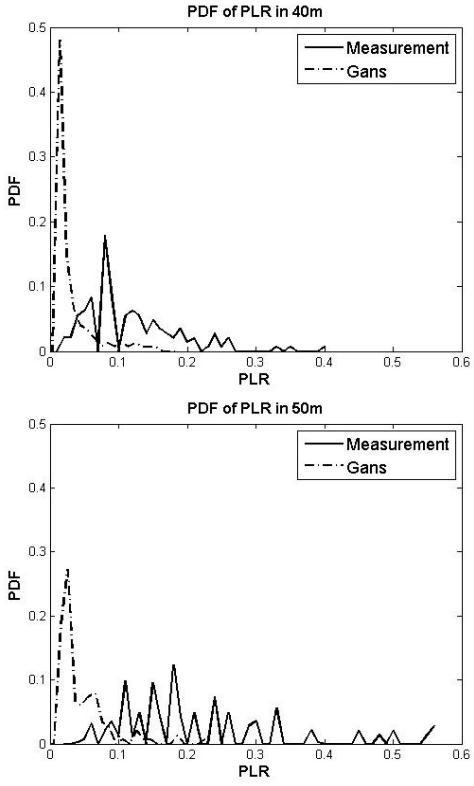

Fig. 3. The PDF of PLR for both measurement and Gans Doppler model.

Figures 3 and 4 depict the probability distribution function (PDF) and cumulative distribution function (CDF) of PLR for the Gans Doppler model and the measurements. Apparently, the Gans Doppler model does not fit the measure-

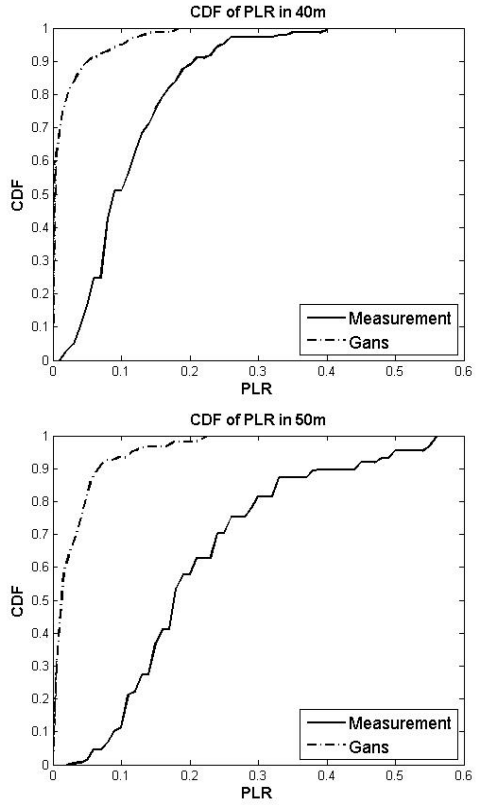

Fig. 4. The CDF of PLR for both measurement and Gans Doppler model.

ments. The reason is that the Gans Doppler model only considers the Doppler Effect caused by one mobile node, which is used in wireless cellular networks. However, for vehicular wireless networks, all vehicles are in motion, and the mobility of all vehicles should be incorporated into the propagation model. Therefore, it is necessary to propose a propagation model for double mobile nodes in vehicular networks.

III. PROPAGATION MODEL FOR DOUBLE MOBLE NODES

Considering a two ray ground model may not be practical for the vehicular application, as it assumes that signals have a perfect 250m radius range, here we proposed to integrate the channel model with a short-term fading channel model as the propagation model for vehicular wireless networks for short-term fading [24], a new fading model for a radio link between double mobile nodes in 3-D scenario. In the following sections, more significant results will be presented.

The radio link considered here is between two vehicles moving with speed $V_i, i = 1,2$ in 3-D scenario. The left one in Fig. 5 shows the coordi-

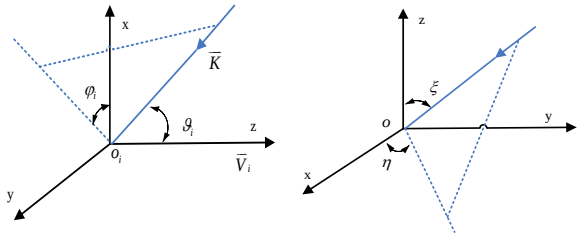

Fig. 5. The coordinate system of mobile vehicles.

nate system of the mobile vehicles and the right one in Fig. 5 displays the referenced coordinate system. According to the radio propagation model for the 2-D wide area with one mobile node [25], the channel time-variant transfer function for radio link between double mobile vehicles in a 3-D scenario can be defined as

$$h(f_0;\vec{r}) = \sum_{k=1}^{N} a_k F_1(\overrightarrow{K_{1k}}) F_2(\overrightarrow{K_{2k}}) e^{j\phi_k - \vec{k_1}\cdot\vec{r_1} - \vec{k_2}\cdot\vec{r_2} - 2\pi f_0 \tau_k}, \quad (1)$$

where $\sum_{k=1}^{N} a_k F_1(\overrightarrow{K_{1k}}) F_2(\overrightarrow{K_{2k}})$ is the relative amplitude, and $\vec{k_1}\bullet\vec{r_1} + \vec{k_2}\bullet\vec{r_2}$ is the phase caused by the double mobile nodes. Setting

$$2\pi f_{dk} = \vec{k_1}\cdot\vec{r_1} + \vec{k_2}\cdot\vec{r_2} = \left|\vec{k_1}\right|\left|\vec{r_1}\right|\cos\vartheta_{1k} + \left|\vec{k_2}\right|\left|\vec{r_2}\right|\cos\vartheta_{2k}, \quad (2)$$

where $\vartheta_{ik}(i = 1,2; k = 1,2,...,N)$ is the angle between $\overrightarrow{V_I}$ and $\overrightarrow{K_{ik}}$. The Doppler frequency shift is thus

$$\begin{aligned} f_{dk} &= \frac{f_0 V_1 t}{c}\cos\vartheta_{1k} + \frac{f_0 V_2 t}{c}\cos\vartheta_{2k} \\ &= f_{d1}\cos\vartheta_{1k} + f_{d2}\cos\vartheta_{2k}, \end{aligned} \quad (3)$$

where $f_{d\max} = f_{d1} + f_{d2}$ is the max Doppler shift caused by the two mobile vehicles. Substituting (3) into (1), we have

$$h(f_0;\vec{r}) = h(f_0;t) = \sum_{k=1}^{N} F_1(\overrightarrow{K_{1k}}) F_2(\overrightarrow{K_{2k}}) e^{j\phi_k - 2\pi f_{dk} - 2\pi f_0 \tau_k}. \quad (4)$$

Assume that the phases are uncorrelated; the time-autocorrelation function of the channel transfer function can be written as

$$\begin{aligned} R_H(\tau) &= E\{h(f_0;t)h^*(f_0;t+\tau)\} \\ &= \sum_{k=1}^{N} E\{F_1^2(\overrightarrow{K_{1k}})\}E\{F_2^2(\overrightarrow{K_{2k}})\}E\{e^{j2\pi f_{dk}\tau}\}, \end{aligned} \quad (5)$$

$\{\overrightarrow{K_{ik}}\}$ and f_{dk} are independent identically distributed. Therefore, (5) can be further written as

$$R_H(\tau) = E\{F_1^2(\overrightarrow{K_{1k}})\}E\{F_2^2(\overrightarrow{K_{2k}})\}E\{e^{j2\pi f_{dk}\tau}\}$$
$$= \int_0^{2\pi}\int_0^{\pi}\int_0^{2\pi}\int_0^{\pi} F_1^2(\vartheta_1,\varphi_1)F_1^2(\vartheta_2,\varphi_2)e^{j2\pi f_d(\vartheta_1,\vartheta_2)\tau} \cdot p_{\vartheta_1,\varphi_1}(\vartheta_1,\varphi_1)\, p_{\vartheta_2,\varphi_2}(\vartheta_2,\varphi_2)\,\mathrm{d}\vartheta_1\mathrm{d}\vartheta_2\mathrm{d}\varphi_1\mathrm{d}\varphi_2, \quad (6)$$

substituting (3) into (6), we have

$$R_H(\tau) = \delta^2 g_1(\tau)g_2(\tau), \quad (7)$$

where $\delta^2 = R_H(0)$ is the average power of the multi-path scattering component, which is the channel variance, and

$$g_i(\tau) = \int_0^{\pi} p_i(\vartheta_i)e^{j2\pi f_{di}\tau\cos\vartheta_i}\mathrm{d}\vartheta_i \quad (i=1,2), \quad (8)$$

$$p_i(\vartheta_i) = \frac{\int_0^{2\pi} F_i^2(\vartheta_i,\varphi_i)p_{\vartheta_i,\varphi_i}(\vartheta_i,\varphi_i)\,d\varphi_i}{\int_0^{\pi}\int_0^{2\pi} F_i^2(\vartheta_i,\varphi_i)p_{\vartheta_i,\varphi_i}(\vartheta_i,\varphi_i)\,d\varphi_i d\vartheta_i}, \quad (9)$$

where $p_i(\vartheta_i)$ is the PDF of the antenna gain when the K-th multi-path arrived or transmitted with an-. gle ϑ_i. Taking the Fourier transform of $R_H(\tau)$, we have the Doppler spectrum

$$S_H(\upsilon) = \delta_H^{\ 2} G_1(\upsilon) * G_2(\upsilon), \quad (10)$$

where $G_i(\upsilon), i=1,2$ is the Fourier transform of $g_i(\tau)$ Since we have $f_{di}\cos\vartheta_i = y$,

$$G_i(\upsilon) = F[\int_0^{\pi} p_i(\vartheta_i)e^{j2\pi f_{di}\tau\cos\vartheta_i}d\vartheta_i]$$
$$= \frac{1}{f_{di}}\int_{-f_{di}}^{f_{di}} \frac{p_i(\arccos\frac{\upsilon}{f_{di}})}{\sqrt{1-(\frac{\upsilon}{f_{di}})^2}}\sigma(v-y)dy, \vartheta_i\in[0,\pi], \quad (11)$$

If the range of ϑ_i is extended from $[0,\pi]$ to $[2n\pi, 2(n+1)\pi]$, where n is the natural number, (11) can be further written as

$$G_i(\upsilon) = \frac{1}{f_{di}}\int_{-\infty}^{\infty} \frac{p_i(\arccos\frac{\upsilon}{f_{di}})}{\sqrt{1-(\frac{\upsilon}{f_{di}})^2}} rect(\frac{y}{2f_{di}})\sigma(v-y)dy$$
$$= \frac{p_i(\arccos\frac{\upsilon}{f_{di}})}{\sqrt{1-(\frac{\upsilon}{f_{di}})^2}} rect(\frac{y}{2f_{di}}), \quad (12)$$

where $rect(\frac{y}{2f_{di}}) = 1$ when $\frac{y}{2f_{di}} < \frac{1}{2}$, and 0 otherwise. And the Doppler spectrum becomes

$$S_H(\upsilon) = \frac{a}{f_{d2}^2}\cdot\frac{p_2(\arccos\frac{\upsilon}{f_{d2}})}{\sqrt{1-(\frac{a\upsilon}{f_{d2}})^2}} * \frac{p_2(\arccos\frac{\upsilon}{f_{d2}})}{\sqrt{1-(\frac{\upsilon}{f_{d2}})^2}}, \quad (13)$$

where $a = f_{d1}/f_{d2,}\ 0<a<1$, and f_{d2} is the Doppler shift caused by one vehicle. The analytical expressions of the Doppler spectrum for double mobile channel proposed here is a random variable of the antenna, relative speed of the two mobile vehicles, and the probability distribution of the received and transmitted multipath wave.

In Fig. 6 is plotted the Doppler spectrums of the proposed double mobile channel model and the conventional Gans model with single mobile node. It illustrates that the Doppler spectrums for two links are different. As the values of vehicle speed ratio (values of frequency shift ratio caused by vehicles) a decreases from 1 to 0, the vertical asymptotes move nonlinearly from the center of the graph to the outside. The curve becomes similar to the Doppler spectrum for link of a single mobile node, and the Doppler spectrum gap shrinks as $a\to 0$ .When $a=0$, that is

$$f_{d2}=0,\ S_H(\upsilon) = p_1(\arccos\frac{\upsilon}{f_{d1}})/(f_{d1}\sqrt{1-(\frac{\upsilon}{f_{d1}})^2}). \quad (14)$$

It is similar to the analytical expression Doppler spectrum for single mobile node, which reveals that our models are more comprehensive.

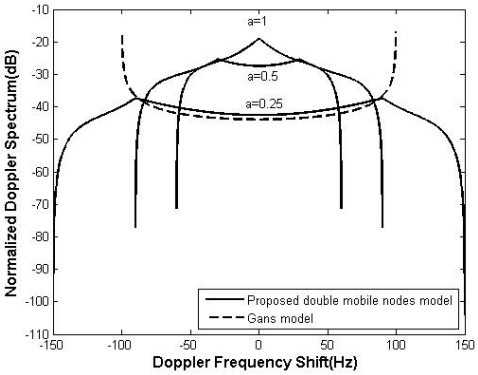

Fig. 6. Doppler spectrum.

IV. PACKET-LEVEL PERFORMANCE EVALUATION

The architecture of mobile nodes used here is depicted in Fig. 7. We use OMNET++ [26] as the simulation tool.

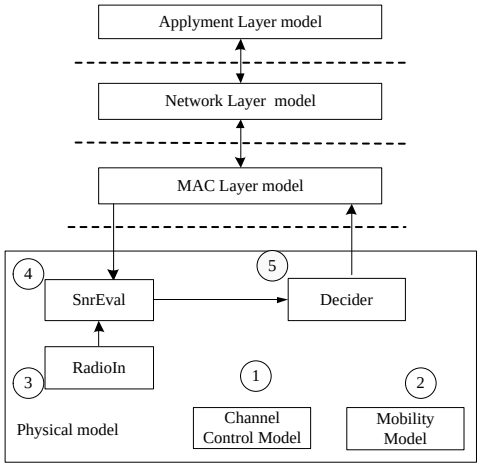

Fig. 7. The architecture of the mobile nodes.

In the simulation, the applyment layer module broadcasts 100 packets per second. The network-layer module is necessary for nodes accessing Internet network. The MAC-Layer module uses the 802.11b communication protocol. The physical module integrates the information of node mobility, received power, background noise and modulation to decide whether a transmitter ground is received correctly. Here, we focus on the SnrEval and Decider modules which are used to control the propagation characteristic. We integrate the proposed Doppler spectrum model with the two ray ground channel model to calculate the received power.

Figures 8 and 9 show the PDF and the CDF of the PLR, which is an important measure for statistical performance of packet level. Apparently, the proposed model fits the measurements quite well compared to the Gans Doppler model. The proposed 3-D scatter fading channel model for double mobile nodes is useful to express the actual radio propagation performance in a dense urban environment. The fading caused by two mobile vehicles is more severe than that caused by single mobile vehicle, and this effect has to be taken into consideration. For different inter-vehicle distances, the proposed model can provide a reasonable match to the measurements.

To further compare these models, we consider the mean error (ε), relative mean error (ε), and mean square standard deviation of error (σ_{MSE}).The mean error reflects the approximation degree between simulation and measurement results; while the mean-square standard deviation of error reflects the extent of the error and the stability of method.

$$\varepsilon = \frac{1}{N}\sum_{t=1}^{N} | x(t) - x_r(t) |, \bar{\varepsilon} = \frac{\varepsilon}{\frac{1}{N}\sum_{t=1}^{N} x_r(t)},$$

$$\sigma_{MSE} = \sqrt{\frac{1}{N}\sum_{t=1}^{N} [x(t) - x_r(t) - \varepsilon]^2}. \quad (15)$$

Table 2 summarizes the results of the proposed model and the Gans model. The mean error ε is between -0.05 - +0.05 when the transmitter-receiver distance is 20m, 30m, 40m, 50m, while that of Gans model is much larger. The relative mean error $\bar{\varepsilon}$ of the proposed channel is under 50%, compared to that of Gans model, which is almost 80%. The proposed model is found to be more accurate based on measured data and can be used to estimate the packet-level performance of vehicular wireless networks in a dense urban environment. However, we also found that as the distance increases, the mean-square standard deviation of error σ_{MSE} increases. The larger distance between transmitter-receiver may result in a larger mean-square standard deviation of error.

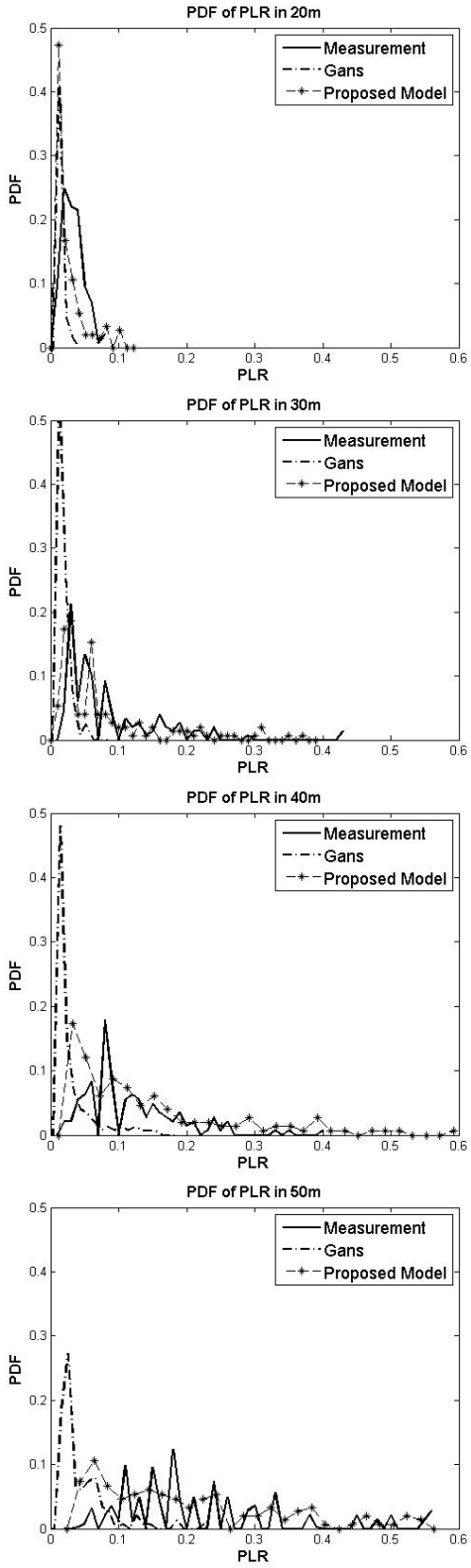

Fig. 8. Comparison in PDF of PLR with inter-vehicle distance 20m, 30m, 40m, and 50m.

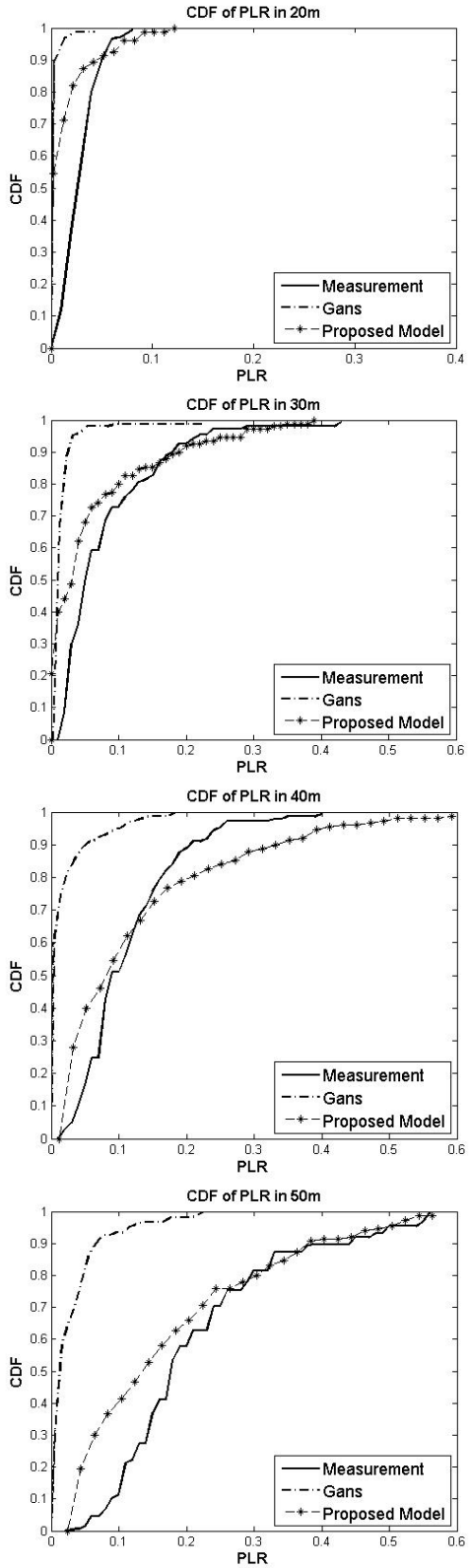

Fig. 9. Comparison in CDF of PLR with inter-vehicle distance 20m, 30m, 40m, and 50m.

Table 2: Comparison of the prediction errors between proposed model and the Gans model

	20m		30m	
	P-model	G-model	P-model	G-model
ε	0.015768	0.028252	0.028747	0.068238
$\overline{\varepsilon}$	0.4693	0.84083	0.35229	0.83625
σ_{MSE}	0.032105	0.058905	0.051324	0.15156
	40m		**50m**	
	P-model	G-model	P-model	G-model
ε	0.043869	0.09113	0.07446	0.1758
$\overline{\varepsilon}$	0.38799	0.80604	0.35035	0.82717
σ_{MSE}	0.077522	0.19414	0.14123	0.37399

V. CONCLUSION

As a key component of the ITS, vehicular wireless networks, has attracted research attention from both the academia and industry of US, EU, and Japan. Although many works have been done on communication and routing protocol, only few models have been developed to characterize the fading effect on vehicular wireless data. This paper presents a real-life experiment conducted in a real environment that collects wireless vehicular measurements to analyze the channel model for vehicular communications and the fading effects. It is shown that the previous Gans Doppler model, which is just based on one mobile node, cannot accurately model the channel variability. To address the problem, a novel channel model based on 3-D scattering fading for radio link between double mobile nodes is developed. The statistical performance of PLR based on the measured data supports the results of the proposed model.

ACKNOWLEDGMENT

This work was an extension beyond I^{2}MTC 2011 Proceeding. The authors would like to thank Dr. Hao Jiang and Jing Wu of Wuhan University for their kind help in vehicle wireless network's measurements in Wuhan City, China. This work was supported by the National Natural Science Foundation of China (No.60762005 and No. 6106 2009), the Natural Science Foundation of Jiangxi Province for Youth (No.2010GQS0153 and No. 2009GQS0070), the Science and Technology Foundation of the Department of Education in Jiangxi Province under Grant GJJ12006) and the Graduate Student Innovation Foundation of Jiang xi Province(YC2011S008).

REFERENCES

[1] T. L. Willke, P. Tientrakool, etc., "A Survey of Inter-Vehicle Communication Protocols and Their Applications," *IEEE Communica-tions Surveys and Tutorials*, vol. 11, no. 2, pp. 3-20, 2009.

[2] V. Tarokh, "New Directions in Wireless Communications Research," *Springer Press*, 2009.

[3] J. M. Francisco, K. T. Chai, C. C. Juan, T. C. Carlos etc., "Emergency Services in Future Intelligent Transportation Systems Based on Vehicular Communication Networks," *IEEE Intelligent Transportation Systems Magazine*, vol. 2, no. 2, pp. 6-20, 2010.

[4] P. Panos, F. Arnaud, E. Knut and etc., "Vehicular Communication Systems: Enabling Technologies, Applications, and Future Outlook on Intelligent Transportation," *IEEE Communication Magazine*, vol. 47, no. 11, pp. 84-95, 2009.

[5] L. J. Li, X. Li, C. J. Cheng, C. Chen, etc., "Research Collaboration and ITS Topic Evolution: 10 Years at T-ITS," *IEEE Transactions on Intelligent Transportation Systems*, vol. 11, no. 3, pp. 517-523, 2010.

[6] G. Mario and K. Leonard, "Vehicular Networks and the Future of the Mobile Internet," *Computer Networks*, vol. 52, no. 2, pp. 457-469, 2011.

[7] C. Sandra, X. M. Shen and etc., "IP Mobility Management for Vehicular Communication Networks: Challenges and Solutions," *IEEE Communications Magazine*, vol. 49, no. 5, pp. 187-194, 2011.

[8] R. D. Tingley and K. Pahlavan, "Space-Time Measurement of Indoor Radio Propagation," *IEEE Transactions on Instrumentation and Measurement*, vol. 50, no.1, 2001.

[9] N. Alsindi, X. Li, K. Pahlavan, "Analysis of Time of Arrival Estimation Using Wideband Measurements of Indoor Radio Propagations," *IEEE Transactions on Instrumentation and Measurement*, vol. 56, no. 5, 2007.

[10] S. Gowrishankar, T. G. Basavaraju, etc., "Effect of Random Mobility Models Pattern in Mobile Ad hoc Networks," *International Journal of Computer Science and Network 160 Security*, vol. 7, no. 6, pp. 160-164, 2007.

[11] J. Yoon, B. Noble, "A General Framework to Construct Stationary Mobility Models for the Simulation of Mobile Networks," *IEEE Transactions on Mobile Computing*, vol. 5, no. 7, pp. 1-12, July 2006.

[12] M. Ho, F. Wu, K. Jian, "Induced Currents on a Moving and Vibrating Perfect Plane Under the Illumination of Electromagnetic Pulse: One-Dimensional Simulation using Characteristic Based Algorithm," *Applied Computational*

Electromagnetics Society Journal, vol. 20, no. 2, 2005.
[13] K. Pawlikowski, H. D. J. Jeong, and J. S. R. Lee, "On Credibility of Simulation Studies of Telecommunication Networks," *IEEE Communication Magazine*, vol. 40, no. 1, pp. 132-139, 2002.
[14] G. Michelson, J. Chuang, "Requirements for Standard Radio Wave Propagation Models for Vehicular Environments," *IEEE 63rd Vehicular Technology Conference*, vol. 6, pp. 2777-2781, 2006.
[15] http://www.isi.edu/nsnam/ns/.
[16] OPNET, http://www.opnet.com.
[17] A. Jardosh, E. M. Belding-Royer, K. C. Almeroth, etc., "Towards Realistic Mobility Models for Mobile Ad Hoc Networks," *in Proceedings of ACM MobiCom*, San Diego, CA, pp. 217C229, 2006.
[18] A. P. Jardosh, E. M. Belding-Royer, etc., "Real-World Environment Models for Mobile Network Evaluation," *IEEE Journal on Selected Areas in Communications*, vol. 23, no. 3, pp. 622-632, 2005.
[19] A. Mahajan, N. Potnis, K. Gopalan and A. Wang, "Modeling Vanet Deployment in Urban Settings," *International Workshop on Modeling Analysis and Simulation of Wireless and Mobile Systems*, Crete Island, Greece, pp. 151-158, 2007.
[20] I. Stepanoy, K. Rothermel, "On the Impact of a More Realistic Physical Layer on MANET Simulations Results," *Ad Hoc Networks*, vol. 6, no. 1, pp. 61-78, 2008.
[21] R. H. Clarke, "A Statistical Theory of Mobile-Radio Reception," *Bell System Technology*, vol. 47, pp. 957-1000, 1968.
[22] M. J. Gans, "A Power Spectral Theory of Propagation in the Mobile Radio Environment," *IEEE Transactions on Vehicular Technology*, vol. 21, no. 3, pp. 27-38, 1972.
[23] A. S. Akki, F. Haber, "A Statistical Model of Mobile-to-Mobile Land Communication Channel," *IEEE Transactions on Vehicular Technology*, vol. 35, no. 1, pp. 2-7, 1986.
[24] Yuhao Wang, Xing Xing, Henry Leung, Siyue Chen and Ming Yao, "Experimental Characterization of Packet-Level for Vehicular Wireless Network in Urban," *IEEE Instrumentation and Measurement Technology Conference*, pp. 1-4, 2011.
[25] G. D. Durgin, "Space-Time Wireless Channels," *Prentice Hall PTR*, vol. 13, pp. 152-171, 2002.
[26] C. P. Mayer and T. Gamer, "Integrating Real World Applications into OMNeT++," *Telematics Technical Reports*, vol. 27, 2008.

Yuhao Wang was born in Hubei, China, in 1977. He received the Ph.D. degree in space physics from Wuhan University, China in 2006. He is a Professor with the School of Information Engineering, Nanchang University, China from 2006. His current interests are in the areas of radio measurements, channel modeling, radio link and network simulation, wireless cellular network, VANET and Software Defined Radio (SDR).

Xing Xing was born in An Hui, China, in 1989. He received the B.S. degree from Nanchang University, China, in 2010. His research interests include radio measurements and wave propagation, computational simulation, and wireless networks.

Yan Zhang was born in Jiang Xi, China in 1987. She received the M.S. degree from Nanchang University, China, in 2011. Her research interests include radio measurements and wave propagation, computational simulation, and wireless networks.

2012 INSTITUTIONAL MEMBERS

DTIC-OCP LIBRARY
8725 John J. Kingman Rd, Ste 0944
Fort Belvoir, VA 22060-6218

AUSTRALIAN DEFENCE LIBRARY
Northcott Drive
Canberra, A.C.T. 2600 Australia

BEIJING BOOK CO, INC
701 E Linden Avenue
Linden, NJ 07036-2495

DARTMOUTH COLLEGE
6025 Baker/Berry Library
Hanover, NH 03755-3560

DSTO EDINBURGH
AU/33851-AP, PO Box 830470
Birmingham, AL 35283

SIMEON J. EARL – BAE SYSTEMS
W432A, Warton Aerodome
Preston, Lancs., UK PR4 1AX

ENGINEERING INFORMATION, INC
PO Box 543
Amsterdam, Netherlands 1000 Am

ETSE TELECOMUNICACION
Biblioteca, Campus Lagoas
Vigo, 36200 Spain

GA INSTITUTE OF TECHNOLOGY
EBS-Lib Mail code 0900
74 Cherry Street
Atlanta, GA 30332

TIMOTHY HOLZHEIMER
Raytheon
PO Box 1044
Rockwall, TX 75087

HRL LABS, RESEARCH LIBRARY
3011 Malibu Canyon
Malibu, CA 90265

IEE INSPEC
Michael Faraday House
6 Hills Way
Stevenage, Herts UK SG1 2AY

INSTITUTE FOR SCIENTIFIC INFO.
Publication Processing Dept.
3501 Market St.
Philadelphia, PA 19104-3302

LIBRARY – DRDC OTTAWA
3701 Carling Avenue
Ottawa, Ontario, Canada K1A OZ4

LIBRARY of CONGRESS
Reg. Of Copyrights
Attn: 407 Deposits
Washington DC, 20559

LINDA HALL LIBRARY
5109 Cherry Street
Kansas City, MO 64110-2498

MISSOURI S&T
400 W 14th Street
Rolla, MO 56409

MIT LINCOLN LABORATORY
Periodicals Library
244 Wood Street
Lexington, MA 02420

NATIONAL CHI NAN UNIVERSITY
Lily Journal & Book Co, Ltd
20920 Glenbrook Drive
Walnut, CA 91789-3809

JOHN NORGARD
UCCS
20340 Pine Shadow Drive
Colorado Springs, CO 80908

OSAMA MOHAMMED
Florida International University
10555 W Flagler Street
Miami, FL 33174

NAVAL POSTGRADUATE SCHOOL
Attn:J. Rozdal/411 Dyer Rd./ Rm 111
Monterey, CA 93943-5101

NDL KAGAKU
C/0 KWE-ACCESS
PO Box 300613 (JFK A/P)
Jamaica, NY 11430-0613

OVIEDO LIBRARY
PO BOX 830679
Birmingham, AL 35283

DAVID PAULSEN
E3Compliance
1523 North Joe Wilson Road
Cedr Hill, TX 75104-1437

PENN STATE UNIVERSITY
126 Paterno Library
University Park, PA 16802-1808

DAVID J. PINION
1122 E Pike Street #1217
SEATTLE, WA 98122

KATHERINE SIAKAVARA
Gymnasiou 8
Thessaloniki, Greece 55236

SWETS INFORMATION SERVICES
160 Ninth Avenue, Suite A
Runnemede, NJ 08078

YUTAKA TANGE
Maizuru Natl College of Technology
234 Shiroya
Maizuru, Kyoto, Japan 625-8511

TIB & UNIV. BIB. HANNOVER
DE/5100/G1/0001
Welfengarten 1B
Hannover, Germany 30167

UEKAE
PO Box 830470
Birmingham, AL 35283

UNIV OF CENTRAL FLORIDA
4000 Central Florida Boulevard
Orlando, FL 32816-8005

UNIVERSITY OF COLORADO
1720 Pleasant Street, 184 UCB
Boulder, CO 80309-0184

UNIVERSITY OF KANSAS – WATSON
1425 Jayhawk Blvd 210S
Lawrence, KS 66045-7594

UNIVERSITY OF MISSISSIPPI
JD Williams Library
University, MS 38677-1848

UNIVERSITY LIBRARY/HKUST
Clear Water Bay Road
Kowloon, Honk Kong

CHUAN CHENG WANG
8F, No. 31, Lane 546
MingCheng 2nd Road, Zuoying Dist
Kaoshiung City, Taiwan 813

THOMAS WEILAND
TU Darmstadt
Schlossgartenstrasse 8
Darmstadt, Hessen, Germany 64289

STEVEN WEISS
US Army Research Lab
2800 Powder Mill Road
Adelphi, MD 20783

YOSHIHIDE YAMADA
NATIONAL DEFENSE ACADEMY
1-10-20 Hashirimizu
Yokosuka, Kanagawa,
Japan 239-8686

APPLIED COMPUTATIONAL ELECTROMAGNETICS SOCIETY JOURNAL
http://aces.ee.olemiss.edu

INFORMATION FOR AUTHORS

PUBLICATION CRITERIA

Each paper is required to manifest some relation to applied computational electromagnetics. **Papers may address general issues in applied computational electromagnetics, or they may focus on specific applications, techniques, codes, or computational issues.** While the following list is not exhaustive, each paper will generally relate to at least one of these areas:

1. **Code validation.** This is done using internal checks or experimental, analytical or other computational data. Measured data of potential utility to code validation efforts will also be considered for publication.

2. **Code performance analysis.** This usually involves identification of numerical accuracy or other limitations, solution convergence, numerical and physical modeling error, and parameter tradeoffs. However, it is also permissible to address issues such as ease-of-use, set-up time, run time, special outputs, or other special features.

3. **Computational studies of basic physics.** This involves using a code, algorithm, or computational technique to simulate reality in such a way that better, or new physical insight or understanding, is achieved.

4. **New computational techniques** or new applications for existing computational techniques or codes.

5. **"Tricks of the trade"** in selecting and applying codes and techniques.

6. **New codes, algorithms, code enhancement, and code fixes.** This category is self-explanatory, but includes significant changes to existing codes, such as applicability extensions, algorithm optimization, problem correction, limitation removal, or other performance improvement. **Note: Code (or algorithm) capability descriptions are not acceptable, unless they contain sufficient technical material to justify consideration.**

7. **Code input/output issues.** This normally involves innovations in input (such as input geometry standardization, automatic mesh generation, or computer-aided design) or in output (whether it be tabular, graphical, statistical, Fourier-transformed, or otherwise signal-processed). Material dealing with input/output database management, output interpretation, or other input/output issues will also be considered for publication.

8. **Computer hardware issues.** This is the category for analysis of hardware capabilities and limitations of various types of electromagnetics computational requirements. Vector and parallel computational techniques and implementation are of particular interest.

Applications of interest include, but are not limited to, antennas (and their electromagnetic environments), networks, static fields, radar cross section, inverse scattering, shielding, radiation hazards, biological effects, biomedical applications, electromagnetic pulse (EMP), electromagnetic interference (EMI), electromagnetic compatibility (EMC), power transmission, charge transport, dielectric, magnetic and nonlinear materials, microwave components, MEMS, RFID, and MMIC technologies, remote sensing and geometrical and physical optics, radar and communications systems, sensors, fiber optics, plasmas, particle accelerators, generators and motors, electromagnetic wave propagation, non-destructive evaluation, eddy currents, and inverse scattering.

Techniques of interest include but not limited to frequency-domain and time-domain techniques, integral equation and differential equation techniques, diffraction theories, physical and geometrical optics, method of moments, finite differences and finite element techniques, transmission line method, modal expansions, perturbation methods, and hybrid methods.

Where possible and appropriate, authors are required to provide statements of quantitative accuracy for measured and/or computed data. This issue is discussed in "Accuracy & Publication: Requiring, quantitative accuracy statements to accompany data," by E. K. Miller, *ACES Newsletter*, Vol. 9, No. 3, pp. 23-29, 1994, ISBN 1056-9170.

SUBMITTAL PROCEDURE

All submissions should be uploaded to ACES server through ACES web site (http://aces.ee.olemiss.edu) by using the upload button, journal section. Only pdf files are accepted for submission. The file size should not be larger than 5MB, otherwise permission from the Editor-in-Chief should be obtained first. Automated acknowledgment of the electronic submission, after the upload process is successfully completed, will be sent to the corresponding author only. It is the responsibility of the corresponding author to keep the remaining authors, if applicable, informed. Email submission is not accepted and will not be processed.

EDITORIAL REVIEW

In order to ensure an appropriate level of quality control, papers are peer reviewed. They are reviewed both for technical correctness and for adherence to the listed guidelines regarding information content and format.

PAPER FORMAT

Only camera-ready electronic files are accepted for publication. The term **"camera-ready" means that the material is neat, legible, reproducible, and in accordance with the final version format listed below.**

The following requirements are in effect for the final version of an ACES Journal paper:

1. The paper title should not be placed on a separate page.

The title, author(s), abstract, and (space permitting) beginning of the paper itself should all be on the first page. The title, author(s), and author affiliations should be centered (center-justified) on the first page. The title should be of font size 16 and bolded, the author names should be of font size 12 and bolded, and the author affiliation should be of font size 12 (regular font, neither italic nor bolded).

2. An abstract is required. The abstract should be a brief summary of the work described in the paper. It should state the computer codes, computational techniques, and applications discussed in the paper (as applicable) and should otherwise be usable by technical abstracting and indexing services. The word "Abstract" has to be placed at the left margin of the paper, and should be bolded and italic. It also should be followed by a hyphen (—) with the main text of the abstract starting on the same line.

3. All section titles have to be centered and all the title letters should be written in caps. The section titles need to be numbered using roman numbering (I. II. ….)

4. Either British English or American English spellings may be used, provided that each word is spelled consistently throughout the paper.

5. Internal consistency of references format should be maintained. As a guideline for authors, we recommend that references be given using numerical numbering in the body of the paper (with numerical listing of all references at the end of the paper). The first letter of the authors' first name should be listed followed by a period, which in turn, followed by the authors' complete last name. Use a coma (,) to separate between the authors' names. Titles of papers or articles should be in quotation marks (" "), followed by the title of journal, which should be in italic font. The journal volume (vol.), issue number (no.), page numbering (pp.), month and year of publication should come after the journal title in the sequence listed here.

6. Internal consistency shall also be maintained for other elements of style, such as equation numbering. Equation numbers should be placed in parentheses at the right column margin. All symbols in any equation have to be defined before the equation appears or right immediately following the equation.

7. The use of SI units is strongly encouraged. English units may be used as secondary units (in parentheses).

8. Figures and tables should be formatted appropriately (centered within the column, side-by-side, etc.) on the page such that the presented data appears close to and after it is being referenced in the text. When including figures and tables, all care should be taken so that they will appear appropriately when printed in black and white. For better visibility of paper on computer screen, it is good to make color figures with different line styles for figures with multiple curves. Colors should also be tested to insure their ability to be distinguished after black and white printing. Avoid the use of large symbols with curves in a figure. It is always better to use different line styles such as solid, dotted, dashed, etc.

9. A figure caption should be located directly beneath the corresponding figure, and should be fully justified.

10. The intent and meaning of all text must be clear. For authors who are not masters of the English language, the ACES Editorial Staff will provide assistance with grammar (subject to clarity of intent and meaning). However, this may delay the scheduled publication date.

11. Unused space should be minimized. Sections and subsections should not normally begin on a new page.

ACES reserves the right to edit any uploaded material, however, this is not generally done. It is the author(s) responsibility to provide acceptable camera-ready files in pdf and MSWord formats. Incompatible or incomplete files will not be processed for publication, and authors will be requested to re-upload a revised acceptable version.

COPYRIGHTS AND RELEASES

Each primary author must execute the online copyright form and obtain a release from his/her organization vesting the copyright with ACES. Both the author(s) and affiliated organization(s) are allowed to use the copyrighted material freely for their own private purposes.

Permission is granted to quote short passages and reproduce figures and tables from and ACES Journal issue provided the source is cited. Copies of ACES Journal articles may be made in accordance with usage permitted by Sections 107 or 108 of the U.S. Copyright Law. This consent does not extend to other kinds of copying, such as for general distribution, for advertising or promotional purposes, for creating new collective works, or for resale. The reproduction of multiple copies and the use of articles or extracts for commercial purposes require the consent of the author and specific permission from ACES. Institutional members are allowed to copy any ACES Journal issue for their internal distribution only.

PUBLICATION CHARGES

All authors are allowed for 8 printed pages per paper without charge. Mandatory page charges of $75 a page apply to all pages in excess of 8 printed pages. Authors are entitled to one, free of charge, copy of the printed journal issue in which their paper was published. Additional reprints are available for $ 50. Requests for additional re-prints should be submitted to the managing editor or ACES Secretary.

Corresponding author is required to complete the online form for the over page charge payment right after the initial acceptance of the paper is conveyed to the corresponding author by email.

ACES Journal is abstracted in INSPEC, in Engineering Index, DTIC, Science Citation Index Expanded, the Research Alert, and to Current Contents/Engineering, Computing & Technology.